

Two Paths Diverged: Exploring Trajectories, Protocols, and Dynamic Phases

by

Todd Robert Gingrich

A dissertation submitted in partial satisfaction of the

requirements for the degree of

Doctor of Philosophy

in

Chemistry

in the

Graduate Division

of the

University of California, Berkeley

Committee in charge:

Professor Phillip L. Geissler, Chair

Professor David Chandler

Associate Professor Lauren K. Williams

Spring 2015

Two Paths Diverged: Exploring Trajectories, Protocols, and Dynamic Phases

Copyright 2015
by
Todd Robert Gingrich

Abstract

Two Paths Diverged: Exploring Trajectories, Protocols, and Dynamic Phases

by

Todd Robert Gingrich

Doctor of Philosophy in Chemistry

University of California, Berkeley

Professor Phillip L. Geissler, Chair

Using tools of statistical mechanics, it is routine to average over the distribution of microscopic configurations to obtain equilibrium free energies. These free energies teach us about the most likely molecular arrangements and the probability of observing deviations from the norm. Frequently, it is necessary to interrogate the probability not just of static arrangements, but of dynamical events, in which case analogous statistical mechanical tools may be applied to study the distribution of molecular trajectories. Numerical study of these trajectory spaces requires algorithms which efficiently sample the possible trajectories. We study in detail one such Monte Carlo algorithm, transition path sampling, and use a non-equilibrium statistical mechanical perspective to illuminate why the algorithm cannot easily be adapted to study some problems involving long-timescale dynamics. Algorithmically generating highly-correlated trajectories, a necessity for transition path sampling, grows exponentially more challenging for longer trajectories unless the dynamics is strongly-guided by the “noise history,” the sequence of random numbers representing the noise terms in the stochastic dynamics. Langevin dynamics of Weeks-Chandler-Andersen (WCA) particles in two dimensions lacks this strong noise guidance, so it is challenging to use transition path sampling to study rare dynamical events in long trajectories of WCA particles. The spin flip dynamics of a two-dimensional Ising model, on the other hand, can be guided by the noise history to achieve efficient path sampling. For systems that can be efficiently sampled with path sampling, we show that it is possible to simultaneously sample both the paths and the (potentially vast) space of non-equilibrium protocols to efficiently learn how rate constants vary with protocols and to identify low-dissipation protocols.

When high-dimensional molecular dynamics can be coarse-grained and represented by a simplified dynamics on a low-dimensional state space, the trajectory space may also be analytically studied using methods of large deviation theory. We review these methods and introduce a simple class of dynamical models whose dynamical fluctuations we compute exactly. The simplest such model is an asymmetric random walker on a one-dimensional ring with a single heterogeneous link connecting two sites of the ring. We derive conditions for the existence of a dynamic phase transition, which separates two dynamical phases—one

localized and the other delocalized. The presence of distinct classes trajectories results in profoundly non-Gaussian fluctuations in dynamical quantities. We discuss the implications of such large dynamical fluctuations in the context of simple stochastic models for biological growth.

To my parents

Contents

Contents	ii
List of Figures	iv
List of Tables	vi
1 Introduction	1
1.1 Trajectory Spaces	1
1.2 Rare Events, Reaction Rates, and a Search for Optimal Protocols	3
1.3 Dynamic Fluctuations	5
1.4 Outline	5
2 Sampling Paths	7
2.1 Introduction	7
2.2 Markov Chain Monte Carlo Entropy Production	8
2.3 Transition Path Sampling with Stochastic Dynamics	10
2.4 Guided Dynamics of a 1d Random Walker	12
2.5 Efficacy of Noise Guidance	17
2.6 Conclusion	24
3 Sampling Protocols	25
3.1 Introduction	25
3.2 Direct Sampling of Protocols: One-Dimensional Barrier Crossing	27
3.3 Protocol Sampling in a TPS Framework	29
3.4 Sampling with a Meta-dynamics on Trajectory Space	33
3.5 Finding Low-dissipation Protocols	37
3.6 Low-dissipation Ising Inversions	41
4 Large Deviation Methods for Markov Processes	47
4.1 Introduction	47
4.2 What is a Rate Function?	48
4.3 Scaled Cumulant Generating Functions and Legendre Transforms	49
4.4 Continuous-time Markov Processes	51

4.5 Distributions of Dynamic Order Parameters	52
4.6 Lebowitz-Spohn Symmetry and the Entropy Production Fluctuation Theorem	56
4.7 Conditioned Dynamics	58
5 Dynamic Phases	61
5.1 Framework	63
5.2 Analytic Solution to 1d Random Walker on a Ring with a Heterogeneity	64
5.3 Properties of the Phase Transition	67
5.4 Flows on Decorated Networks	72
5.5 Physical Implications of Dynamic Phases	75
5.6 Conclusions	80
A Entropy Production Statistics for a One-Dimensional Random Walker with Guiding Forces	81
A.1 Mean Entropy Production	81
B Ising Model Steady State Correlations	84
C Extended Ensemble Double Well Transition Path Sampling	86
D Path and Protocol Sampling for the Ising Model	89
D.1 Ising Dynamics and Dissipation	89
D.2 Path Sampling	91
D.3 Protocol Sampling	93
E Ring Network with Heterogeneity Scaled Cumulant Generating Function	95
F Analytical Treatment of the Triangle Network	97
Bibliography	100

List of Figures

2.1	Three Strategies for Guiding Trajectories	14
2.2	Entropy Production Large Deviation Functions for Guided Trajectories	15
2.3	Overlap Between Different Ising Trajectories	18
2.4	Time-dependent Correlations in Guided Ising Trajectories	19
2.5	Strategy for Guiding Lattice Dynamics with Important Intermediate States . . .	21
2.6	Steady State Correlations in Guided Ising Trajectories	22
2.7	Decorrelation of Noise-Guided WCA Trajectories	23
3.1	Schematic Illustrating Guided Assembly Dynamics	26
3.2	Scanning Versus Random Walks	27
3.3	Double Well Schematic	28
3.4	Brute Force Barrier Crossing Trajectories	30
3.5	Double Well Paths and Protocols	32
3.6	Frequency Dependence of Double Well Transitions	34
3.7	Frequency Dependence from Transition Path Dynamics	36
3.8	Ising Spin Flip Dissipation Sampling with a Single Trajectory	44
3.9	Ising Spin Flip Dissipation Sampling with a Ten Trajectories	45
3.10	Ising Spin Flip Dissipation Distribution for a Fixed Protocol	46
4.1	Smooth Legendre Transform	50
4.2	Legendre Transform with a Cusp	51
4.3	Cycle with Three States	53
4.4	Connections Between Tilted Operator, SCGF, and LDF	57
5.1	Two-Dimensional Rate Function Schematic	65
5.2	Ring Network with Heterogeneity	66
5.3	Ring Network SCGF	70
5.4	Critical Driving in Ring Network	71
5.5	Ring Network Joint Rate Functions	72
5.6	Triangle Network with Heterogeneity	73
5.7	Triangle Network SCGF	74
5.8	Triangle Network SCGF —Analytical and Numerical Comparison	75

5.9	Triangle Network Large Deviation Function	76
5.10	Effective Markov Process for Entropy Production Biases	77
5.11	Survival Probability for Ring Network Trajectories	79

List of Tables

B.1 Enumeration of Correlated Transitions for Ising Dynamics	85
--	----

Acknowledgments

First and foremost, I want to acknowledge my advisor, Phill Geissler. More than anyone, Phill has prepared me to become an independent scientist. He has taught me to find problems, tinker with them, then finally write a thorough paper, with emphasis on clarity. I have absorbed Phill's emphasis on long-term, rigorous contributions, and will continue to aspire to his model of clear communication. I was fortunate to also receive significant guidance from David Chandler. The problems addressed in this thesis are clearly influenced by David's prior work and advice. David's classroom instruction was tuned perfectly to my needs, but his tennis instruction is also noteworthy. After I had hardly touched a racket in ten years, David dragged me back to the tennis courts several times a week. I am thankful for the opportunities we had to run each other around the court, and I sincerely hope David finds more chances to hit in the future.

I am deeply indebted to two excellent postdocs, with whom I worked closely, Michael Grünwald and Suriyanarayanan Vaikuntanathan. Michael helped introduce me to path sampling. Most of my work in Chapters 2 and 3 directly benefited from his guidance. I was fortunate that Suri arrived on the scene as I was growing tired of path sampling methods. We had great fun working together on the project that became Chapter 5. Both Suri and Michael exuded enthusiasm and competence in a way I could only hope to mimic.

Toward the end of my time in graduate school, I have thoroughly enjoyed collaborating with Gavin Crooks and Grant Rotskoff on a project discussed in Sections 3.5 and 3.6. Grant, in particular, has been the consummate sounding board. Through frequent mathematical sparring, he would politely correct my mistakes and sharpen my reasoning. I wish that I could have been as useful to him as he has been to me.

The Pitzer center community has been vibrant throughout my stay. I've appreciated the scientific and social company of Patrick Shaffer, Ayelet Benjamini, Anna Schneider, Katie Klymko, Dayton Thorpe, Chris Ryan, John Haberstroh, Lisa Littlejohn, David Limmer, Aaron Keys, Patrick Varilly, Alex Hudson, Kelsey Schuster, Shachi Katira, Milo Lin, Kranthi Mandadapu, John Chodera, and David Sivak, as well as all of those furious people I have forgotten to list. Really, you were great too.

None of this would have been possible without the generous support of the National Science Foundation and the Fannie and John Hertz Foundation. Five years is a long time to trust someone to pursue their interests freely. I am immensely grateful to have been afforded that privilege. The academic and social support from the Hertz Foundation was especially significant. The retreats, workshops, and lunches were scientifically invigorating, introducing me to problems and people from a broad array of disciplines.

In addition to being my scientific home, Berkeley, well Oakland rather, has been my actual home, thanks to the loving environment at 548 63rd Street. Hotel 63rd, starring Ryan, Kayte, Linda, David, Jeanne, Glenn, Pat, Hoppy, Sydney, and Grant with guest appearances by Kathleen, Bob, and others, has been a wonderful place to live. The mixture of good food, irreverent music, and a frisbee-catching dog has contributed greatly to my sanity, and I will be sad to leave (there Ryan, I said it).

A special thank you goes to all the friends who got me away from work to do fun things. Alex Brown, Carlos Daganzo, John Fry, and Henry Wong reached out and invited me to join their weekly doubles match at the Rose Garden. Thanks to Pat, Hoppy, Suri, and Grant for tolerating my slow cycling pace. Ben Mathews, Anthony, Melis, Suri, Grant, Anna, Ben Zax, Pat, Hoppy, Linda, David, Ryan, Kayte, Sydney, Jane, and others gave me excuses to abscond to Yosemite, Salt Point, Big Sur, Mt. Whitney, Yosemite again, the John Muir Wilderness, Yosemite a few more times, and Lake Tahoe. Ray Sidney taught me about gracious living and showed me the best ways to play when I needed a break. A very special thank you goes to Amy, who helped me check several items off my bucket list: snow camping in Sequoia, regular camping in Point Reyes, backpacking in Kings Canyon (with great trout fishing!), and canyoneering on a trip to Zion.

And now, the most important acknowledgment: my family. My parents have offered unyielding support. They set me off on this path long ago, perhaps unintentionally, by giving me books, the freedom to ask questions, and a healthy dose of stubborn. Thanks to my siblings for never making fun of my decision to spend seven years of my life pursuing graduate degrees. I have enjoyed watching from afar as Rebecca has graduated from college and moved into her profession, and it will be a real treat for us to live in the same city again after eleven years. Whether they know it or not, Mark and Kari regularly remind me of the important things in life by giving me a glimpse of their love for Adam, Alex, and Emily. Thanks to Grandma and Grandpa for always being excited and encouraging when I called, even if they thought I was only doing it to pass the time while walking home (I wasn't). Finally, thanks to Adam, Alex, and Emily, who have shown me how much people should be able to learn in the amount of time I've been in graduate school.

Chapter 1

Introduction

1.1 Trajectory Spaces

Every introductory chemistry student studies the interplay between thermodynamics and kinetics. It is customary to first impress upon students that nature minimizes free energy. By balancing energetic and entropic considerations, we can predict which reactions will occur, how much heat they will generate, whether a protein will fold, and countless other properties. Eventually, we are all confronted by experiments which disagree with such thermodynamic analysis, at which point we are taught to blame “kinetic effects.” Equivalently, we might say the system is *out of equilibrium*. This thesis is devoted to these non-equilibrium effects. It concerns methods, analytical and numerical, which calculate the probability of trajectories in and out of equilibrium.

Equilibrium thermodynamics rests upon an assumption that chaotic chemical dynamics has reached a particularly simple stationary distribution. This assumption is exceptionally powerful, when applicable. For example, we can derive relationships between different macroscopic properties of a large collection of molecules (temperature, pressure, etc.) without requiring any knowledge of the microscopic structure. If we include some knowledge of these microscopic details, then it is furthermore possible to relate large-scale material properties to molecular motions using tools of statistical mechanics [26]. It may be hard to construct the appropriate microscopic models—it is not always clear how to appropriately parameterize the model—but the conceptual framework is straightforward. As Feynman famously noted, once the Boltzmann distribution is built up, the rest is a slide down from the summit [45].

But what can we understand when a physical system has not converged to a Boltzmann steady state? We can ignore dynamics for equilibrium statistical mechanics, but the dynamical details are crucial to non-equilibrium processes. This conundrum is ubiquitous and important. Natural and synthetic microscopic systems routinely carry out processes which are not in equilibrium due to time-varying external fields or spatially-dependent gradients. We could, for example, want to understand molecular motors in a cell, which operate far from

equilibrium due to the continual influx of chemical fuel [99]. Alternatively, imagine a material scientist trying to grow crystals in exotic patterns by introducing chemical components and electromagnetic fields in well-timed intervals [106]. Under these conditions, the probability of a molecular arrangement cannot be expressed solely in terms of a time-independent energy function. Instead, the likelihood of observing any configuration must depend on the entire dynamical history. In the absence of an equilibrium steady state, we must model the dynamics with a differential equation that captures the time evolution. By analyzing the space of trajectories, we can ultimately address the kinetics of non-equilibrium systems.

Unfortunately, simulating molecular trajectories in a physically meaningful way is not simple since chemical systems contain a large number of interacting quantum mechanical particles. In this thesis, we focus on situations for which the principal challenge stems, not from the quantum mechanical nature of matter, but rather from the high-dimensionality of the classical phase space. Thus we will make the significant assumption that the processes of interest are classical in nature, in which case the positions and momenta of particles are propagated by Hamiltonian mechanics. By neglecting quantum effects, we limit ourselves to processes which do not make or break chemical bonds. Despite this limitation, a surprising number of chemistry problems can be addressed, i.e., there is a long, successful history of classical models describing the non-covalent interactions between collections of many molecules [5, 6, 109, 98].

Imagine, for example, that we want to understand how a salt crystal dissolves in a glass of stirred water. This simple situation is impossibly hard to handle explicitly. No computer can propagate classical dynamics of 10^{23} water molecules. Even if we explicitly simulate a manageable subsystem, what are we to do with a trajectory of many thousands of particles? The trajectory is so high-dimensional that it is not clear how to extract meaningful information. Typically we are not so interested in the wiggling and jiggling of every molecule. We would rather know about some statistical properties of the trajectory, say the typical time it takes for the crystal to dissolve. The state of the salt could be classified as either crystalline or dissolved and we could seek the typical time required to transition between the two macroscopic, or coarse-grained, states. The inverse of this timescale is a phenomenological rate constant describing the dynamics of macростates [25].

Reducing complex dynamics to phenomenological rate constants can be viewed as a form of dimensionality reduction. We average over many high dimensional trajectories to extract a low dimensional object, a rate constant. There are, of course, many dimensionality reduction techniques popular in the fields of computer science and statistics, but we want to also utilize what we know from physics. Namely, Hamilton's equations give a physical model for dynamics in the full-dimensional space, and ideally we should use this dynamics before projecting the trajectories down to a lower-dimensional space. The alternative requires concocting an effective dynamics without the benefit of classical mechanics. This philosophy of prioritizing the molecular dynamics underscored the creation of a method known as transition path sampling (TPS), which uses Monte Carlo (MC) techniques to sample trajectories evolving in the full classical phase space [20, 32, 33]. By averaging over the statistical ensemble of trajectories, we can characterize particular features of the trajectories: the typical

time for a reaction to occur, the propensity of the trajectories to loop around cycles, or the likelihood that nanoparticles will assemble into useful macroscopic structures. Path sampling methods can extract these features in a uniquely efficient manner by harvesting rare trajectories which exemplify the critical dynamical behaviors, i.e., trajectories illustrating reactions, cycles, or particle assembly, respectively. Let us elaborate upon this connection between rare trajectories and reaction rates in the specific context of nanoparticle assembly.

1.2 Rare Events, Reaction Rates, and a Search for Optimal Protocols

Modern experimental methods provide a remarkable ability to manipulate matter on the molecular scale. Using one such technology, colloidal nanoparticles are coated with complementary strands of DNA to sensitively modulate the attractions between particles in solution [51]. Application of equilibrium theory has contributed to an improving capability to control the macroscopic structures that form when many of these particles interact with each other [41, 89, 116]. Early experiments with DNA-coated particles controlled the crystallization of colloids, directing them toward face-centered cubic or body-centered cubic lattices [15, 93, 95]. These methods have been extended to, e.g., generate colloidal clusters [85] and even to design self-replicating colloidal chains [76].

Two extensions of this experimental program demand a consideration of non-equilibrium effects. Firstly, as targeted structures grow in size and complexity, the final structures become pathway-dependent due to kinetic traps [37]. The energy and time scales for a large cluster of particles to meaningfully rearrange become sufficiently large that it is not reasonable to assume that the dynamics is in a quasi-equilibrium. Rather, a particle's future positioning is intimately linked to its dynamical history. This history-dependence is a hallmark of a non-equilibrium process. Secondly, there are active efforts to construct dynamic machines with DNA nanotechnology [84, 104, 123]. Much like biological machines inside a cell, these synthetic machines could be driven by ATP or some other form of accessible chemical energy. By consuming energy, it is possible for these machines to generate cycles in phase space, meaning, e.g., that a motor can rotate clockwise more than counterclockwise. Such cycles cannot be designed in an equilibrium system [101].

Motivated by the challenges presented by non-equilibrium dynamics, the first half of this thesis addresses computational methods to design protocols which guide trajectories toward desired dynamical outcomes. The probability that a trajectory is steered toward a desired target depends sensitively on a huge set of control parameters (temperature, pressure, the choice of DNA sequences, salt concentrations, etc.), and the space of possible controls is typically much too vast to experimentally search. A central goal of this thesis is to evaluate numerical approaches which could identify the fruitful regions of parameter space. In effect, we would like to be able to understand how the assembly rate depends on the protocol.

Designing optimal protocols is, of course, a common engineering goal which arises in

other contexts. When we piece together resistors, capacitors, and operational amplifiers to build an analog circuit, we *are* designing an out-of-equilibrium system. What is so different about the chemical design problems? A core difference is that it is generally unclear how to decompose complex molecular dynamics into cleanly-separated subunits, of the sort provided by the lumped components of analog electronics. In the world of electronics, we control the interactions between separate well-characterized subsystems, say by soldering a resistor to a capacitor. A test tube of diffusing DNA-coated colloids affords less of an opportunity to isolate subsystems—all colloids have the potential to chemically associate with the others. There has been recent progress in extending engineering approaches to biomolecular design by working with specialized units whose molecular features can be abstracted away, i.e., a molecular unit can be treated as a lego brick which always binds to its mated neighbors. We pursue a complementary line of inquiry. When we lack the luxury of specialized subunits which interact strongly and simply, can we nevertheless design macroscopic properties? The essential feature of our study is the explicit numerical propagation of microscopic models. Given a model for dynamics, we focus on methods to explore the effect of different protocols on the behavior of trajectories.

Whether in or out of equilibrium, it is straightforward to simulate classical trajectories and compare the outcome generated from different protocols. It might seem that we should just try simulations with all possible protocols and see which one works best, for example, which protocol causes nanoparticles to assemble into a target structure. This direct strategy is doomed in all but the simplest cases. We typically cannot even enumerate all protocols, much less simulate trajectories using each one. Furthermore, there is a timescale problem. In particular, an assembly of nanoparticles that might take fractions of a second to occur in a test tube, takes much more time for a computer to simulate. Thus even “good” parameters which lead to rapid assembly on experimental timescales might not result in rapid assembly on the timescale that computers simulate. On those shorter timescales, assembly is an exceptionally rare event.

When the transformation from unassembled to assembled structures is a Poisson process, we can actually learn about the assembly rate from trajectories which are much shorter than the typical assembly event. These short trajectories offer a route to calculating rate constants which is far more computationally efficient than waiting for the typical assembly time [21]. More specifically, we obtain the rate by quantifying the likelihood that a short trajectory will exhibit assembly. Transition path sampling, an importance sampling in the space of trajectories, highlights these rare transitions so their probability can be measured. If protocols are sampled in concert, we can also compare the relative rates of assembly under different protocols. Chapters 2 and 3 develop, analyze, and discuss these methods for sampling trajectories and protocols.

1.3 Dynamic Fluctuations

In many dynamical systems it is important to characterize rather than control trajectories. The need for dynamical characterization is especially significant in biophysical contexts, where stochasticity of dynamics is often underappreciated. As an example, a frequently displayed animation of kinesin depicts regular unidirectional steps which transport cargo along a microtubule [79]. Notably, the cargo is never shown to take a backward step and the time between steps is uncannily uniform. This type of regular motion is common in our everyday macroscopic lives, but it inappropriately represents the molecular scales. A more nuanced model must capture fluctuations away from the average behavior. Many dynamical properties are merely renormalized by the incorporation of fluctuations. For instance, allowing kinesin to take occasional backward steps will slow its effective transport velocity. The second half of this thesis addresses how fluctuations can have a more dramatic, qualitative effect.

In particular, we focus on the distribution of time-additive dynamical observables. These observables, which can be as simple as a count of the total number of steps taken by a kinesin molecule, convey coarse-grained features of the dynamics while ignoring the finer particularities of any given trajectory. In many contexts, it is known that these *dynamic order parameters* exhibit broad distributions characteristic of trajectory spaces which have different classes of trajectories that yield distinct dynamical behavior [56, 114, 115, 121]. TPS methods have been applied to glass-forming chemical systems to isolate such classes of trajectories, thereby illustrating a *dynamic phase transition* that divides two *dynamic phases* [64, 72]. Demonstrations of dynamic phase transitions can be made rigorous using formal methods of large deviation theory [112], which we review in Chapter 4. We use these methods in Chapter 5 to analyze dynamical fluctuations in simple non-equilibrium models, showing that dynamic phase transitions can emerge from very innocuous models.

1.4 Outline

This thesis is organized into four self-contained chapters which address ways to sample rare trajectories, manipulate phenomenological rate constants, and compute dynamical fluctuations. Chapters 2 and 3 discuss numerical methods for sampling paths and protocols, respectively. Chapters 4 and 5 are more analytical in nature. These chapters review formal methods for analyzing rare Markovian trajectories generated by master equations and introduce a new solvable model that exhibits a dynamic phase transition. Before advancing to the main text, let us embed each of the chapters more firmly in the context of prior work, starting with trajectory sampling.

Numerical sampling of rare trajectories is useful to understand both reactions rates [21] and dynamic phase transitions [56, 64, 114, 115, 121]. When we know a low-dimensional coordinate along which the trajectories of interest proceed, methods like Transition Interface Sampling [42, 90] or Forward Flux Sampling [1] may be employed to great benefit.

Unfortunately it is generally difficult to identify such a “reaction coordinate,” and there are well-documented challenges when an inappropriate coordinate is selected [20, 33]. In contrast, TPS requires no prior knowledge of reaction pathways. While TPS has been an invaluable tool for many problems in physics and chemistry [20, 53, 64], the method has its own shortcomings. The algorithm becomes profoundly inefficient when the timescale of the sampled trajectories grows too long [23, 59]. Chapter 2 explains the source of this inefficiency and illustrates a way around the problem when simulating the dynamics of an Ising model. We use what we learn about effective sampling of paths in Chapter 3, where we discuss the concurrent sampling of trajectories and protocols. We show that sampling the protocol space gives a convenient and computationally efficient way to quantitatively determine how rate constants depend on experimental protocols. Notably, this methodology applies equally well to protocols in and out of equilibrium, but out-of-equilibrium processes must consume energy that is dissipated to the environment. We show that the same framework naturally lets us study the protocol-dependence of this dissipative cost.

In the second half of the thesis we discuss analytical methods to compute the probability of rare dynamical fluctuations. The formal large deviations framework is well-established, and Chapter 4 serves as a review of these methods. We use this formalism in the final chapter, where we investigate the impact of dynamical disorder on single-body dynamics. The well-known phenomena of Anderson localization addresses how disorder in a potential energy surface can force an electron to localize. We consider a different type of disorder in a classical setting. Suppose a set of N states are connected in a ring and a single particle can hop clockwise or counterclockwise in Markovian manner with some rate constants. Introducing a unique set of transition rates between one pair of nearest neighbors is sufficient to introduce a localization/delocalization transition which markedly affects the probability of rare trajectories on the ring. In Chapter 5, we introduce this model and solve for the fluctuations in two dynamic order parameters, demonstrating the existence of a dynamic phase transition. While dynamic phase transitions are known in many more complicated many-body systems [49, 64, 75], our work emphasizes that dynamic phases can also emerge in much simpler systems. Since dynamic phase transitions can be expected even in very simple models, we close by noting how intuition from the model may inform our understanding of large dynamical fluctuations in biological contexts.

Chapter 2

Sampling Paths

2.1 Introduction

Recent advances in non-equilibrium statistical mechanics have given fresh perspectives on computational procedures applied to fluctuating molecular systems. The Jarzynski work relation and the Crooks fluctuation theorem, for instance, provide routes to compute equilibrium quantities from non-equilibrium measurements [29, 69, 81, 91, 94, 96]. Here, we demonstrate that traditional Metropolis-Hastings Markov Chain Monte Carlo (MCMC) can be similarly viewed as a procedure to extract equilibrium sampling from generically non-equilibrium processes. Monte Carlo trial moves drive a system away from the steady state distribution, and an entropy production can be assigned to these driven transformations. This interpretation provides an elegant way to understand challenges encountered in MCMC sampling, one that is especially revealing for MCMC sampling of trajectories. Path sampling methods suffer routinely from profound inefficiency when trajectories of interest become long. From a non-equilibrium perspective on MCMC, we provide simple and quantitative ways to understand the inefficiency.

Importance sampling of trajectories has enabled studies of a myriad of dynamical processes in physics and chemistry [2, 3, 20, 53, 64, 66]. In particular, reaction rates and mechanisms can be found by transition path sampling (TPS), which examines the subensemble of trajectories that complete a reaction [21]. The practicality of TPS depends intimately on the design of the Monte Carlo (MC) move set. Namely, the moves must generate correlated trajectories so that a trial trajectory is likely to exhibit similar dynamical behavior as the previously sampled trajectory. Chaotic divergence and microscopic reversibility of equilibrium dynamics informs the construction of two such moves, the so-called “shooting” and “shifting” moves [21]. These methods generate correlated trajectories by propagating alternative histories from highly correlated initial configurations. For sufficiently short trajectories, the imposed correlation at one time serves to strongly correlate the trajectories at all times. Long trajectories, however, are problematic: trial trajectories either lose all useful

This chapter has been submitted to *The Journal of Chemical Physics*.

correlation with the reference path, or else they coincide so closely with the reference that changes are impractically small [59]. In both cases the efficiencies of shooting and shifting moves plummet as trajectories grow longer. Sampling trajectories that involve slow molecular rearrangements and diffusive processes stands to benefit significantly from alternative methods of generating correlated trajectories.

We consider three different ways to guide long trajectories: introducing auxiliary forces; selecting among a series of short trial segments, as in Steered Transition Path Sampling (STePS) [60]; and advancing stochastic integrators with correlated random numbers (which we refer to as “noise guidance”) [30, 110]. Of the three, only noise guidance yields an MC entropy production which is subextensive in the trajectory length. The other schemes, which accumulate extensive entropy production, cannot efficiently extend to sampling of long trajectories. Strong noise guidance is not, however, a panacea; correlated noises need not imply correlated trajectories. We illustrate this point by considering Glauber dynamics of a two-dimensional Ising model and Langevin dynamics of a two-dimensional Weeks-Chandler-Andersen (WCA) fluid. Only when microscopic degrees of freedom have a small number of discrete possibilities, as in the lattice dynamics, is it possible to generate correlated long-timescale trajectories by tuning the noise.

The structure of the chapter is as follows. First we introduce and discuss the perspective of MC moves as non-equilibrium processes which produce entropy, detailing the consequences of constraints analogous to fluctuation theorems and the second law of thermodynamics. Next we review transition path sampling in stochastic dynamics and demonstrate the challenge posed by long trajectories in the context of trajectory sampling of a one-dimensional random walker. We then analyze alternative strategies to correlate long trajectories of a one-dimensional single particle system and of a two-dimensional Ising model. Finally, we explore how strongly noise guidance correlates trajectories in example systems, and then conclude.

2.2 Markov Chain Monte Carlo Entropy Production

We start by discussing a very general perspective on traditional Metropolis-Hastings MCMC sampling [63, 87]. Consider the problem of sampling a configuration, \mathbf{x} , according to probability distribution $P(\mathbf{x})$. For example, \mathbf{x} could be a vector of the coordinates and momenta of N hard spheres, the state of spins in an Ising model, or all coordinates of a classical trajectory. The Metropolis-Hastings algorithm generates a Markov chain, which can be thought of as a dynamics through configuration space with the steady-state distribution $P(\mathbf{x})$. This dynamics obeys detailed balance but is not necessarily physical.

One typically splits each Monte Carlo move into two steps. First, a change from \mathbf{x} to a new state $\tilde{\mathbf{x}}$ is proposed according to a generation probability, $P_{\text{gen}}[\mathbf{x} \rightarrow \tilde{\mathbf{x}}]$. Throughout this chapter we will refer to \mathbf{x} as a reference and $\tilde{\mathbf{x}}$ as the trial. This trial is conditionally accepted with probability

$$P_{\text{accept}}[\mathbf{x} \rightarrow \tilde{\mathbf{x}}] = \min [1, e^{-\omega}] , \quad (2.1)$$

where

$$\omega = \ln \frac{P(\mathbf{x}) P_{\text{gen}}[\mathbf{x} \rightarrow \tilde{\mathbf{x}}]}{P(\tilde{\mathbf{x}}) P_{\text{gen}}[\tilde{\mathbf{x}} \rightarrow \mathbf{x}]}.$$
 (2.2)

Together, these two steps ensure detailed balance, guaranteeing that the equilibrium distribution $P(\mathbf{x})$ is stationary under the MC protocol. Lacking the conditional acceptance step, such an MC procedure would generally drive a system away from its equilibrium distribution. We find it instructive to view this notional process as a genuine non-equilibrium transformation, one that would generate nonzero entropy in most cases. In the formalism of stochastic thermodynamics, the resulting entropy production corresponds precisely to the quantity ω defined in Eq. (2.2) [102].

The MC acceptance step effectively filters realizations of this non-equilibrium process, with a bias towards low values of ω . By construction, the bias exactly negates the tendency of trial move generation to drive a system out of equilibrium. From this perspective, the countervailing tendencies of proposal and acceptance are akin to the operation of a Maxwellian demon, which by contrast filters realizations of *equilibrium* dynamics with a bias that creates a *non-equilibrium* state.

Viewing the procedure in the language of entropy production distributions reveals an important asymmetry of $P(\omega)$. Following the more general demonstration of an entropy production fluctuation theorem [31], note that

$$\begin{aligned} P(\omega) &= \int d\mathbf{x} d\tilde{\mathbf{x}} P(\mathbf{x}) P_{\text{gen}}(\mathbf{x} \rightarrow \tilde{\mathbf{x}}) \delta(\omega - \omega(\mathbf{x}, \tilde{\mathbf{x}})) \\ &= \int d\mathbf{x} d\tilde{\mathbf{x}} e^{\omega(\mathbf{x}, \tilde{\mathbf{x}})} P(\tilde{\mathbf{x}}) P_{\text{gen}}(\tilde{\mathbf{x}} \rightarrow \mathbf{x}) \delta(\omega + \omega(\tilde{\mathbf{x}}, \mathbf{x})) \\ &= e^\omega P(-\omega), \end{aligned}$$
 (2.3)

with $\omega(\mathbf{x}, \tilde{\mathbf{x}})$ representing the entropy produced by a proposal move from \mathbf{x} to $\tilde{\mathbf{x}}$ and δ denoting the Dirac delta function. We are more likely to propose moves with positive entropy production than we are to choose their negative counterparts. The straightforward corollary, $\langle \omega \rangle \geq 0$, is by analogy a statement of the second law, and the equality is satisfied if and only if $P(\omega) = \delta(\omega)$. A further consequence of Eq. 2.3 relates the MC acceptance rate to the probability of attempting a move with a negative value of ω , which we call $p_<$. Specifically,

$$\langle P_{\text{accept}} \rangle = \int d\omega P(\omega) \min[1, e^{-\omega}] = 2p_<,$$
 (2.4)

which has been noted in the related context of replica exchange Monte Carlo [95]. As $\langle \omega \rangle$ increases, $p_<$, and therefore $\langle P_{\text{accept}} \rangle$, tends to decrease. We will see that $\langle \omega \rangle$ scales with the number of driven degrees of freedom, such that Monte Carlo sampling of chain molecules or of long trajectories becomes especially challenging.

We focus below on the sampling of dynamical pathways (rather than individual configurations). In this case ω is an “entropy production” only by analogy, since the “non-equilibrium transformations” effected by MC trial moves occur in the more abstract space of trajectories. Lessons from Eq. (2.3) are nevertheless illuminating in the context of this abstract space.

2.3 Transition Path Sampling with Stochastic Dynamics

Trajectory Space and Trajectory Subensembles

Let us now specialize to the sampling of discrete-time stochastic trajectories with a fixed number of steps, t_{obs} . The probability of observing a trajectory, $\mathbf{x}(t) \equiv \{\mathbf{x}_0, \mathbf{x}_1, \dots, \mathbf{x}_{t_{\text{obs}}}\}$, can be written as

$$P_0[\mathbf{x}(t)] \propto \rho_{\text{init}}(\mathbf{x}_0) \prod_{t=0}^{t_{\text{obs}}-1} p(\mathbf{x}_t \rightarrow \mathbf{x}_{t+1}), \quad (2.5)$$

where ρ_{init} is a distribution for the initial time point, frequently an equilibrium or steady state distribution. The probability of each time propagation step is denoted $p(\mathbf{x}_t \rightarrow \mathbf{x}_{t+1})$, the form of which depends on details of the stochastic dynamics. We refer to this propagation as the natural dynamics. Representative trajectories can be generated by sampling the initial state and propagating natural dynamics.

In many contexts, it is useful to study a biased trajectory ensemble constructed to highlight particular rare events. Common examples include the reactive subensemble,

$$P_{\text{reactive}}[\mathbf{x}(t)] \propto P_0[\mathbf{x}(t)] h_A(\mathbf{x}_0) h_B(\mathbf{x}_{t_{\text{obs}}}), \quad (2.6)$$

and the so-called tilted ensemble,

$$P_{\text{tilted}}[\mathbf{x}(t), s] \propto P_0[\mathbf{x}(t)] e^{-sK[\mathbf{x}(t)]}. \quad (2.7)$$

In the former case, h_A and h_B are indicator functions which constrain the endpoints of the trajectory to fall in regions of phase space corresponding to reactants and products of a chemical reaction or other barrier crossing process [21]. In the latter case, $K[\mathbf{x}(t)]$ is an order parameter reporting on dynamical properties of the trajectory (e.g. the current [36], activity [64, 75], or entropy production [74, 86, 103]) and s sets the strength of bias [50]. These biased ensembles highlight classes of trajectories only rarely sampled by the natural dynamics. To effectively sample them, a Markov chain of correlated trajectories is constructed. The correlations between subsequent steps of the Markov chain ensure that newly-generated trajectories are likely to share the rare features that made the prior trajectory a good representative of the biased ensemble.

Sampling with Shooting Moves

One of the most general and effective methods for generating a trial trajectory is the shooting move, which is particularly well-suited to sampling equilibrium dynamics [21]. The move proceeds as follows. A discrete time, t_{shoot} , between 0 and t_{obs} is uniformly selected and designated the shooting time. The state of the system at t_{shoot} , perhaps slightly modified,

is then propagated forward and backward in time with natural dynamics to yield a trial trajectory, $\tilde{\mathbf{x}}(t)$. The probability of generating this trial takes the form

$$P_{\text{gen}}[\mathbf{x}(t) \rightarrow \tilde{\mathbf{x}}(t)] = p_{\text{gen}}(\mathbf{x}_{t_{\text{shoot}}} \rightarrow \tilde{\mathbf{x}}_{t_{\text{shoot}}}) \prod_{t=0}^{t_{\text{shoot}}-1} \bar{p}(\mathbf{x}_{t+1} \rightarrow \mathbf{x}_t) \prod_{t=t_{\text{shoot}}}^{t_{\text{obs}}-1} p(\mathbf{x}_t \rightarrow \mathbf{x}_{t+1}),$$

where \bar{p} is the transition probability for time-reversed dynamics and p_{gen} is the probability of the perturbation at the shooting time. In the language of Section 2.2, the entropy produced by this trial move is given by

$$\omega = \ln \frac{\rho_{\text{init}}(\mathbf{x}_0) h_A(\mathbf{x}_0) h_B(\mathbf{x}_{t_{\text{obs}}}) p_{\text{gen}}(\mathbf{x}_{t_{\text{shoot}}} \rightarrow \tilde{\mathbf{x}}_{t_{\text{shoot}}})}{\rho_{\text{init}}(\tilde{\mathbf{x}}_0) h_A(\tilde{\mathbf{x}}_0) h_B(\tilde{\mathbf{x}}_{t_{\text{obs}}}) p_{\text{gen}}(\tilde{\mathbf{x}}_{t_{\text{shoot}}} \rightarrow \mathbf{x}_{t_{\text{shoot}}})} + \sum_{t=0}^{t_{\text{shoot}}-1} \ln \frac{p(\mathbf{x}_t \rightarrow \mathbf{x}_{t+1}) \bar{p}(\tilde{\mathbf{x}}_{t+1} \rightarrow \tilde{\mathbf{x}}_t)}{\bar{p}(\mathbf{x}_{t+1} \rightarrow \mathbf{x}_t) p(\tilde{\mathbf{x}}_t \rightarrow \tilde{\mathbf{x}}_{t+1})}. \quad (2.8)$$

For trial trajectories to be accepted by the MCMC scheme, ω must be small. However, when p and \bar{p} are not equal (as is the case in driven processes), the sum in Eq. (2.8) has order t_{obs} nonvanishing terms¹. Consequently, $\langle \omega \rangle$ scales linearly with t_{obs} , and $P(\omega)$ adopts the long-time form

$$P(\omega) \sim \exp[-t_{\text{obs}} I(\omega/t_{\text{obs}})], \quad (2.9)$$

with large deviation rate function $I(\omega/t_{\text{obs}})$. From this asymptotic expression for the entropy produced by a TPS move, one might generally expect that the corresponding acceptance rate decreases exponentially as t_{obs} grows long.

This extensive growth of $\langle \omega \rangle$ with time has an important and general exception, namely the case of microscopically reversible dynamics. Under those conditions, the sum in Eq. (2.8) vanishes and the only entropy production is contributed from the endpoints of the trajectory (e.g., h_A and h_B). Since this entropy production is subextensive in time, long trajectories appear no more difficult to sample than short ones. The acceptability of trial trajectories, however, is also subject to biases like those expressed in Eqs. (2.6) and (2.7). Because long trajectories typically decorrelate strongly from one another, the rare, biased qualities of a reference trajectory (e.g., reactivity or inactivity) are recapitulated in the trial path with a probability that also decays with t_{obs} .

We conclude that the challenges for efficiently sampling long trajectories are twofold. The TPS move must produce entropy that is subextensive in observation time or the method will not scale to long trajectories. Additionally, one must preserve strong correlations between $\mathbf{x}(t)$ and $\tilde{\mathbf{x}}(t)$, so that rare properties of interest are retained in the trial trajectory. In the next section we show that these two goals are often conflicting. In particular, we examine three general schemes for engineering correlations between reference and trial trajectories in shooting-like moves. Two of the schemes fail to exhibit subextensive entropy production scaling while the remaining scheme can only maintain strong trajectory correlations in special cases.

¹Since t_{shoot} is uniformly selected between 0 and t_{obs} , t_{shoot} is of order t_{obs} . Furthermore, while neighboring terms in the sum may be correlated, there will still be order t_{obs} independent terms for sufficiently long t_{obs} .

2.4 Guided Dynamics of a 1d Random Walker

We explore the three methods for trial trajectory generation in the specific context of a one-dimensional discrete-time random walker with equation of motion

$$x_{t+1} = x_t + \xi_t, \quad (2.10)$$

where at the t^{th} timestep, the noise ξ_t is drawn from the normal distribution with zero mean and variance σ^2 . As a simple illustration focusing on the effects of entropy production, suppose we want to sample the unbiased trajectory distribution

$$P_0[x(t)] \propto \delta(x_0) \exp \left[- \sum_{t=0}^{t_{\text{obs}}-1} \frac{(x_{t+1} - x_t)^2}{2\sigma^2} \right], \quad (2.11)$$

where the initial position is set to zero without loss of generality ². To construct a reference trajectory $x(t)$, we draw a value for ξ_t at each timestep and propagate the walker's position according to Eq. (2.10). A trial trajectory is then generated by evolving dynamics from the same initial configuration (with a different realization of the noise or perhaps even a different equation of motion).

We imagine that it is desirable for the trial trajectory to retain a significant correlation with the reference path. This goal is motivated by the challenges of sampling biased ensembles as discussed above, but for the sake of simplicity we do not include such a bias here. To ensure this correlation, we employ shooting moves that differ from the conventional procedure described in Section 2.3. Specifically, we implement and scrutinize three distinct ways to engineer correlation over long times: (a) adding artificial forces that pull the trial trajectory closer to the reference, (b) preferentially selecting among sets of otherwise unbiased short path segments, or (c) using correlated histories of noises. We assess the influence of these three biasing methods on the MCMC efficiency by characterizing the distribution $P(\omega)$.

Guiding Forces

We first consider effecting correlations with guiding forces, i.e., artificial contributions to the effective potential that tend to lead the trial trajectory toward the reference. This strategy is equivalent to using steered molecular dynamics [67] to generate new trajectories. The trial trajectory $\tilde{x}(t)$ is grown with the equation of motion

$$\tilde{x}_{t+1} = \tilde{x}_t + \tilde{\xi}_t + k(x_t - \tilde{x}_t). \quad (2.12)$$

We denote $\tilde{\xi}_t$ as the trial trajectory noise at timestep t , also drawn from a Gaussian with mean zero and variance σ^2 . The linear spring constant k adjusts the strength of correlation

²Typically TPS procedures concurrently sample the initial configuration, but that complication is not necessary for our illustration.

between reference and trial trajectories. The probability that this guided dynamics generates a particular trial from the reference is given by

$$P_{\text{gen}}[x(t) \rightarrow \tilde{x}(t)] \propto \exp \left[- \sum_{t=0}^{t_{\text{obs}}-1} \frac{(\tilde{x}_{t+1} - \tilde{x}_t - k(x_t - \tilde{x}_t))^2}{2\sigma^2} \right]. \quad (2.13)$$

The entropy production associated with the trial move depends also on the probability of generating the reverse TPS move, growing the reference trajectory with extra forces pulling it close to the trial. It is straightforward to compute ω from Eq. (2.2),

$$\omega = -\frac{k}{\sigma^2} \sum_{t=0}^{t_{\text{obs}}-1} (x_t - \tilde{x}_t)(x_{t+1} + \tilde{x}_{t+1} - x_t - \tilde{x}_t). \quad (2.14)$$

In this approach, ω can be physically interpreted as the difference between two work values: that expended by the artificial force to guide the trial trajectory, versus the work that would be required to conversely guide the reference. The resulting distribution of entropy production, obtained from numerical sampling, is shown in Fig. 2.1(a).

Since ω is given by a sum over all t_{obs} timesteps, $P(\omega)$ adopts a large deviation form as in Eq. (2.9), and $\langle \omega \rangle \propto t_{\text{obs}}$. These scaling properties are demonstrated numerically in Fig. 2.2(a) and analytically in Appendix A. In the appendix we re-express ω in terms of the ξ and $\tilde{\xi}$ variables, which can be integrated over to yield

$$\langle \omega \rangle = \frac{2}{(k-2)^2} [(2-k)kt_{\text{obs}} - 1 + (k-1)^{2t_{\text{obs}}}] . \quad (2.15)$$

Indeed, for $0 < k < 2$, this expression gives the anticipated long time scaling with t_{obs} ,

$$\langle \omega \rangle \sim \frac{2kt_{\text{obs}}}{2-k}. \quad (2.16)$$

As seen in Fig. 2.1(a), the negative- ω tail of $P(\omega)$, which gives rise to MCMC acceptances, becomes correspondingly small for large t_{obs} .

Guiding Choices

In both Sections 2.3 and 2.4 we showed that time-extensive entropy production arises generically when we do not use natural (forward) dynamics to generate a trajectory. Dynamical biases can alternatively be achieved by preferentially selecting among different examples of natural dynamics. At a high level, conventional TPS [21] is just such an approach, constructing biased trajectory ensembles through selection rather than artificial forces. Can this strategy be used effectively to impose resemblance between reference and trial trajectories?

We consider a scheme very similar in spirit to the STePS algorithm [60]. Like configurational-bias MC sampling of a polymer [46], the STePS procedure generates a long trajectory by

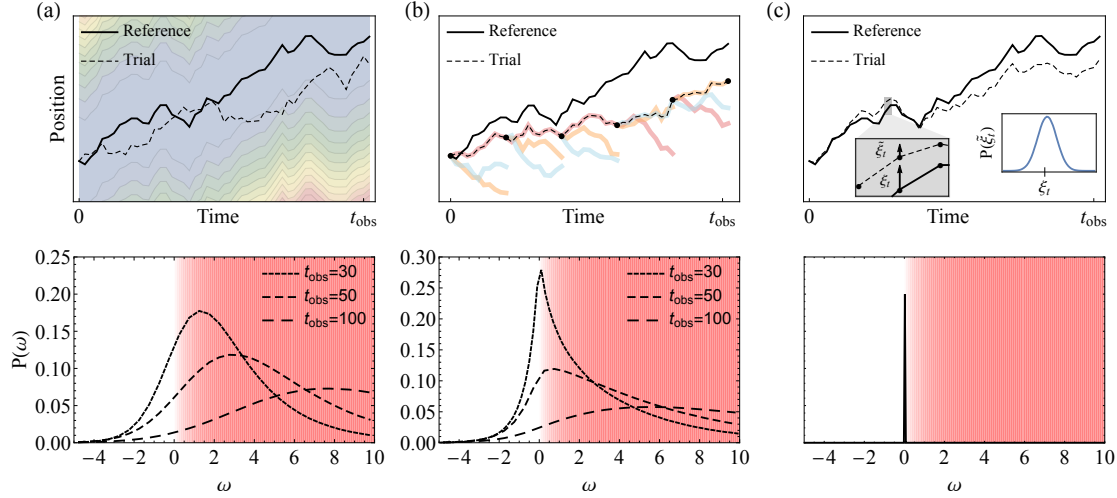


Figure 2.1: Three guidance schemes for generating a trial trajectory that maintains proximity to a reference trajectory. For the specific case of a one-dimensional random walker, upper panels illustrate the consequences of (a) artificial corralling forces (b) preferential selection of short trial branches and (c) correlated noise histories. Bottom panels show the corresponding distributions of trajectory space entropy production ω . The intensity of red shading reflects the probability that trial moves are rejected. For cases (a) and (b), the average entropy production is nonzero and grows with trajectory length t_{obs} . With an appropriately designed noise guidance scheme (c), symmetric selection of noise variables results in identically zero entropy production for all trajectory lengths.

piecing together short segments, as illustrated in Fig. 2.1(b). To generate a new segment, one starts at the end of the previous segment and samples a collection of short, unbiased trajectories according to the natural dynamics, which we will refer to as branches. One of these branches is selected as the next segment of the trial trajectory, with a preference for branches that stay close to the reference trajectory. (Proximity could be judged in different ways, e.g., through Euclidean distance in the full phase space, or with respect to an order parameter). Though each branch is grown with natural dynamics, the added segment is biased. To show that this bias affects acceptance rates in the same manner as the guiding forces bias, we compute the entropy produced by a TPS move.

Starting at the initial condition of the reference trajectory, we grow n branches of length τ according to

$$x_{t+1}^{(\alpha)} = x_t^{(\alpha)} + \xi_t^{(\alpha)}, \quad (2.17)$$

where α is an index over the n independent samples of the natural dynamics. Of these n possibilities for the i^{th} segment of the trial trajectory, we select branch α with probability

$$P_{\text{select}}(\alpha) = \frac{f(|x_{i\tau}^{(0)} - x_{i\tau}^{(\alpha)}|)}{\sum_{\gamma=1}^n f(|x_{i\tau}^{(0)} - x_{i\tau}^{(\gamma)}|)}, \quad (2.18)$$

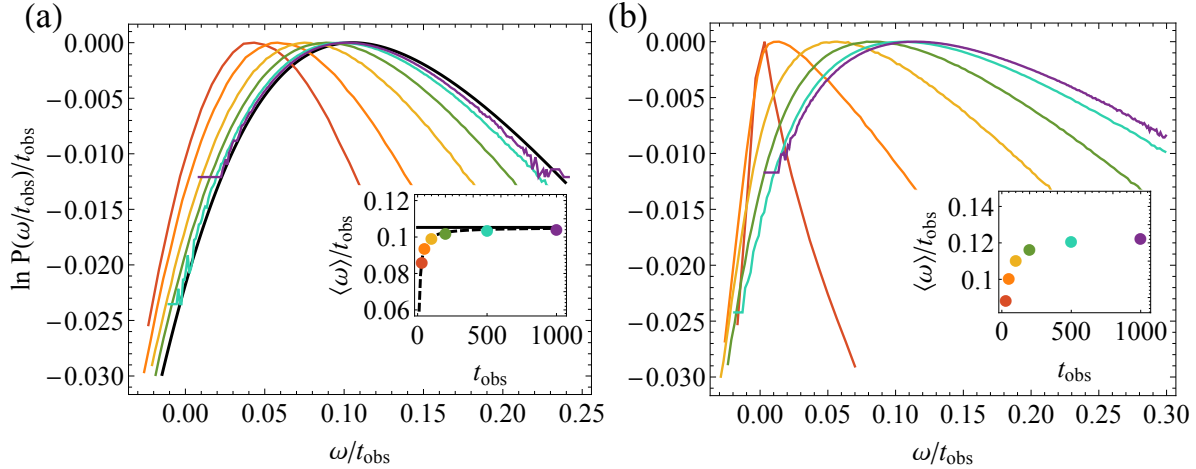


Figure 2.2: Entropy production statistics for trial moves with guiding forces (a) and guiding choices (b), as discussed in Sections 2.4 and 2.4 of the main text. Results in (a) are shown for $k = 0.1$; black curves indicate the long-time behavior determined analytically in Appendix A. Results in (b) are shown for $n = 3, \tau = 10$ and with $f(x) = e^{-|x|}$. In both panels, different colors indicate different trajectory lengths, ascending from left to right: $t_{\text{obs}} = 30$ (red), 50 (orange), 100 (yellow), 200 (green), 500 (cyan), and 1000 (purple).

where f is a weighting function with a maximum when its argument is zero, for example a Gaussian centered on zero. The reference trajectory is indicated by a superscript (0). Starting from the end of the chosen branch, the growth procedure is repeated with n new branches of length τ .

While each time propagation step uses segments of unbiased natural dynamics, the selection of preferred branches exerts a bias which ultimately leads to a nonvanishing entropy production,

$$\omega = - \sum_{i=1}^{t_{\text{obs}}/\tau} \ln \frac{\sum_{\gamma \neq 0} f(|x_{i\tau}^{(\gamma)} - x_{i\tau}^{(0)}|)}{\sum_{\gamma \neq \alpha_i} f(|x_{i\tau}^{(\gamma)} - x_{i\tau}^{(\alpha_i)}|)}, \quad (2.19)$$

where α_i is the index of the selected branch for the i^{th} segment. The calculation of this entropy production requires generation of the backwards TPS move, in which the (0) branch is always selected.

In the preceding section we discussed that the entropy produced by guiding forces could be thought of in terms of a work performed by the bias. From that perspective, this guiding choices scheme trades work for information. We bias the dynamics not by applying explicit forces but instead by selecting the preferred branches based on information about the likelihood that a branch stays close to the reference. In particular, ω is a difference between the Shannon information associated with selecting the set of trial branches which produced the trajectory $\tilde{x}(t)$ and the information associated with selecting the reference branches in a

reverse TPS move. As with biasing forces, the trajectory space entropy production exhibits large deviation scaling with $\langle \omega \rangle \propto t_{\text{obs}}$. Numerical demonstrations of this scaling are provided in Fig. 2.2(b). Consequently, acceptance probabilities drop precipitously in the long time limit.

Guiding Noises

As a third scheme for engineering path correlation, we consider generating a trial trajectory with natural dynamics but with biased noises. Rather than trying to corral trajectories to proceed along similar paths, one may impose much simpler correlations between their underlying noise histories [30]. Consider a TPS trial move which consists of re-propagating dynamics from the initial timestep using new noises $\tilde{\xi}$ that differ only slightly from the old noises ξ ,

$$\tilde{\xi}_t = \alpha \xi_t + \sqrt{1 - \alpha^2} \eta_t, \quad (2.20)$$

where η_t is sampled from a Gaussian distribution with zero mean and variance σ^2 . In Section (2.4), the symbol α was used as an index, but here we redefined α to be the parameter controlling noise correlations. Guiding Gaussian noise variables in this manner has been referred to as a Brownian tube proposal move [110]. Unlike the prior two kinds of moves, the Brownian tube proposal produces strictly vanishing entropy production ω for all trials regardless of trajectory length. The cancellation results from some algebra after writing the path weights and generation probabilities in terms of the noise variables,

$$\frac{P(\xi) P_{\text{gen}}(\xi \rightarrow \tilde{\xi})}{P(\tilde{\xi}) P_{\text{gen}}(\tilde{\xi} \rightarrow \xi)} = \frac{\exp\left[-\frac{\xi^2}{2\sigma^2}\right] \exp\left[-\frac{(\tilde{\xi}-\alpha\xi)^2}{2(1-\alpha^2)\sigma^2}\right]}{\exp\left[-\frac{\tilde{\xi}^2}{2\sigma^2}\right] \exp\left[-\frac{(\xi-\alpha\tilde{\xi})^2}{2(1-\alpha^2)\sigma^2}\right]} = 1, \quad (2.21)$$

where ξ is a vector detailing noises at all times.

The vanishing entropy production is achieved by *independently sampling* the noise variables. In the previously discussed approaches, the bias applied to any one noise variable depended on how far astray the trial trajectory had drifted from its reference up to that point in time. Such history-dependent biasing coupled the sampling of one noise variable to all of the previous noises, ultimately giving rise to the nonvanishing ω (see Appendix A for an explicit demonstration). By sampling all noises independently, we can perturb the ξ variables in a symmetric manner. For noises drawn from a Gaussian distribution, this symmetric perturbation was given in Eq. (2.20), but the strategy of symmetrically sampling independent noises generalizes to other choices of stochastic dynamics. For example, Hartmann has applied these methods with uniform random variable noises to Monte Carlo dynamics in the form of Wolff dynamics of a two-dimensional Ising model [62].

Using correlated noise histories to sample Monte Carlo trajectories avoids the time-extensive bias that arose from guiding paths in configuration space, but this merit comes at a cost. If the reactive or tilted ensembles are to be sampled, it is important that the guidance scheme produces highly correlated trajectories. That is to say, the x coordinates,

not just the ξ coordinates, must be correlated. When will similar noise histories produce similar trajectories? In the remainder of the chapter we address this question in the context of two dynamical systems, one on-lattice and the other off-lattice.

2.5 Efficacy of Noise Guidance

In the preceding section we noted that sampling trajectories with noise-guided shooting moves avoids a time-extensive MC entropy production. However, we seek correlated trajectories, not just correlated noises. When trajectories with correlated noises synchronize, efficient path sampling of long trajectories can be achieved. But under what conditions should such synchronization be expected? We investigate this question by studying lattice dynamics of a two-dimensional Ising model and off-lattice dynamics of a WCA fluid, also in two dimensions. We show that synchronization can be achieved with a suitable treatment of Ising dynamics. This success does not extend to our example of off-lattice dynamics.

Ising Dynamics

Let us first consider a two-dimensional Ising model consisting of N spins. The i^{th} spin, denoted σ_i , takes the value ± 1 . The lattice evolves, at inverse temperature β , under single spin-flip Glauber dynamics with Hamiltonian

$$H = -h \sum_i \sigma_i - J \sum_{\langle ij \rangle} \sigma_i \sigma_j. \quad (2.22)$$

The spins interact in the usual Ising manner; they couple to nearest neighbors with coupling constant J and to an external field h . Each spin-flip trial move requires us to choose two random numbers uniformly from $[0, 1)$. One random number, ξ_{site} , determines which site will be flipped. The other random number, ξ_{acc} , determines whether to accept or reject the flip. Given ξ_{site} and ξ_{acc} , the spin-flip move is deterministic:

1. Choose spin $i = \text{ceiling}(\xi_{\text{site}} N)$ to act on.
2. Construct a trial state by flipping spin i .
3. Compute the energy difference, ΔE , between the original configuration and the trial.
4. Accept the spin flip if $\xi_{\text{acc}} < (1 + \exp(\beta \Delta E))^{-1}$.

By carrying out t_{obs} sequential MC sweeps, each consisting of N spin flip moves, we construct an Ising trajectory, $\sigma(t)$. The effective unit of time is taken to be a MC sweep.

Now consider a noise-guided trial TPS move designed to generate a trajectory $\tilde{\sigma}(t)$ which is correlated with $\sigma(t)$. At every MC step we alter ξ_{site} and ξ_{acc} to some trial values, $\tilde{\xi}_{\text{site}}$ and

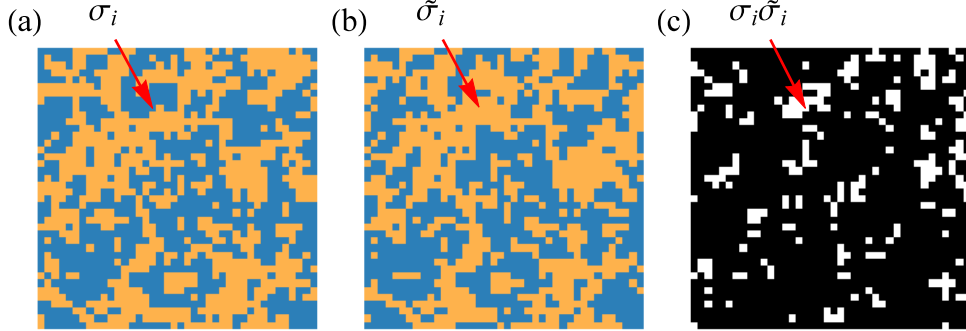


Figure 2.3: Correlations between a reference trajectory and a trial trajectory generated by the noise guidance method described in Section 2.5 using $\epsilon_{\text{dir}} = \epsilon_{\text{site}} = 10^{-3}$ and $\epsilon_{\text{acc}} = 0.1$. The two trajectories begin with identical initial conditions and evolve through 100 sweeps of push up/push down Monte Carlo steps at $\beta J = 0.3, h = 0$. Final configurations of reference and trial trajectories are shown in (a) and (b), respectively. The site-wise overlap between these two configurations is depicted in (c), where black indicates spin alignment and white indicates anti-alignment.

$\tilde{\xi}_{\text{acc}}$. There is significant freedom in doing so, while producing zero entropy³, and we analyze one particular choice. We focus first on updating the noise that chooses which spin to flip. With probability $1 - \epsilon_{\text{site}}$ we reuse the old noise, i.e., $\tilde{\xi}_{\text{site}} = \xi_{\text{site}}$. Otherwise, we uniformly draw a new value of $\tilde{\xi}_{\text{site}}$ from the unit interval. The tunable parameter ϵ_{site} controls the correlation between noise histories of the reference and trial trajectory. We update the noises that control conditional acceptance, ξ_{acc} , in an analogous manner. Another parameter, ϵ_{acc} , is the probability of drawing new noise for $\tilde{\xi}_{\text{acc}}$.

Starting with the initial configuration of $\sigma(t)$, we construct $\tilde{\sigma}(t)$ by performing spin flips with the new trial noise history. The trial and reference trajectories start in identical configurations, but we expect the correlation to decay as MC time advances. To monitor the similarity between reference and trial, we study the site-wise product between σ and $\tilde{\sigma}$ as illustrated in Fig. 2.3. The average of this product over all spins,

$$\sigma \cdot \tilde{\sigma} = \frac{1}{N} \sum_{i=1}^N \sigma_i \tilde{\sigma}_i \quad (2.23)$$

is a measure of correlation between σ and $\tilde{\sigma}$. Decorrelated configurations return a value of zero while identical configurations return one. Fig. 2.4(a) shows that the average correlation between $\sigma(t)$ and $\tilde{\sigma}(t)$ decays to zero at long times. The rate of this decay is tuned by ϵ_{acc} and ϵ_{site} , the parameters controlling the extent of noise correlation. At long

³We want symmetric proposal probabilities, $p(\xi \rightarrow \xi') = p(\xi' \rightarrow \xi)$.

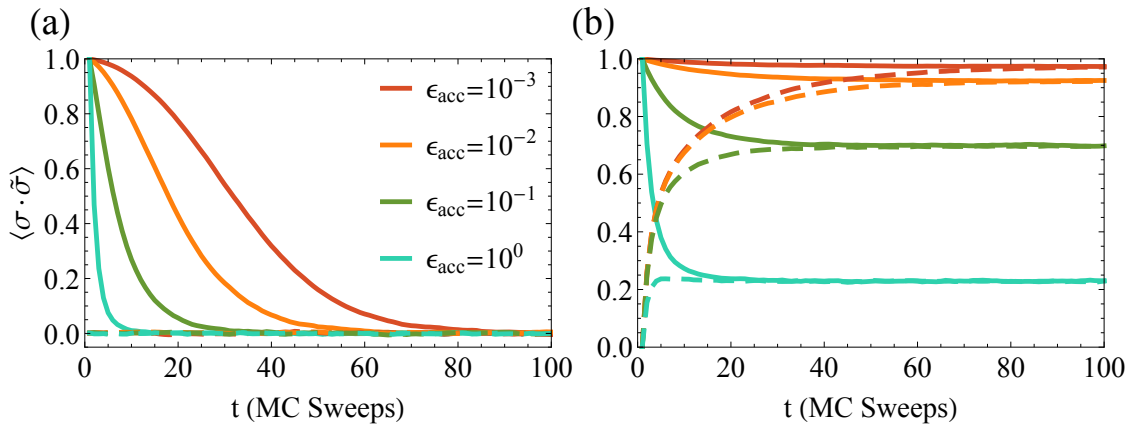


Figure 2.4: Average overlap between reference and trial trajectories of a 40×40 two-dimensional Ising model with $\beta J = 0.3$. Results are shown in (a) for ordinary Glauber spin flip dynamics, and in (b) for the modified directional dynamics described in Section 2.5. Two trajectories with identical initial conditions and different-but-correlated noise histories (solid lines) maintain a nonzero steady state overlap at long times only for the case of push up/push down dynamics. The same steady state values are obtained when the two trajectories evolve from very different initial conditions (dashed lines) generated by independently assigning each spin at random. Different colors indicate different values of the noise guidance parameter ϵ_{acc} . Ensemble-averaged results are shown for $\epsilon_{\text{site}} = \epsilon_{\text{dir}} = 0.001$, with averages performed over 500 independent pairs of trajectories.

times $\langle \sigma \cdot \tilde{\sigma} \rangle$ eventually approaches zero, even with the strongest noise guidance. The corresponding ‘‘uncorrelated’’ configurations, however, bear a subtler resemblance. Some regions are significantly correlated, while others are significantly anti-correlated, averaging to give $\sigma \cdot \tilde{\sigma} \approx 0$.

Motivated by this subtler resemblance, we introduce a minor alteration in the implementation of Glauber spin-flip dynamics. Below we detail this modification and show that it does in fact enable the preservation of correlation between trajectories over very long times. As observed in the context of damage spreading, different choices of Ising model Monte Carlo dynamics can result in identical equilibrium states yet different dynamical properties [65, 83]. The effectiveness of correlated noises in guiding trajectories is, in effect, one such dynamical property.

In particular, we replace step 2 of the spin-flip move to include a directionality. We introduce another random number, $\xi_{\text{dir}} \in [0, 1)$, used to decide the trial state. If $\xi_{\text{dir}} < 0.5$, the trial state is a down spin; otherwise it is up. Whereas the conventional trial move effects an attempted spin flip, this trial move can be viewed as an attempt to push the spin either up or down, depending on the state of ξ_{dir} . As with the other noise variables, correlations

between ξ_{dir} and $\tilde{\xi}_{\text{dir}}$ are tuned by the probability ϵ_{dir} of resampling the noise.

The addition of directionality to the spin-flip dynamics results in moves which are trivially ineffectual. For example, half of the spin moves attempt to “push up” a spin which is already up. These moot moves are absent from the traditional implementation of single-spin-flip Glauber dynamics, which attempts a spin flip at every step of MC time. In every other respect, the two schemes generate Markov chains with identical statistics. They can therefore be made identical by excising moot moves, or, equivalently on average, by scaling time by a factor of two.

As Fig. 2.4(b) illustrates, the push up/push down implementation of single-spin-flip Glauber dynamics allows the trial trajectories, $\tilde{\sigma}(t)$ to remain close to $\sigma(t)$ for long times. By incorporating information about spin change directionality into the noise history, the noises signal not just how likely a spin is to change, but in what direction it will change. Appropriately chosen ϵ parameters can maintain tunable correlations between trajectories for an arbitrarily long time. When averaged over the whole lattice, steady state correlation is maintained, but the correlations are spatially heterogeneous. As MC time progresses, the regions in which two trajectories are highly correlated move throughout the lattice, ensuring ergodic exploration of the trajectory space.

For push up/push down dynamics, noise guidance does not merely preserve correlations that existed at time zero. We find that correlated noise histories can in fact *induce* synchronization between trajectories. To illustrate this synchronization effect, we have characterized the correlation between trajectories that share similar noise histories only intermittently. As shown in Fig. 2.5, such paths acquire similarity during periods of strong noise guidance. This similarity degrades during periods without noise guidance, but can be recovered by re-introducing guidance, regardless of how significantly correlations have decayed. Indeed, even very different initial configurations, propagated with correlated noises, become more similar with time, their ensemble-averaged correlation $\langle \sigma \cdot \tilde{\sigma} \rangle$ converging to the same value as for trajectories that are identical at time zero.

A nonzero steady state value of $\langle \sigma \cdot \tilde{\sigma} \rangle$ is the quantitative signature of synchronization. The origins of this finite asymptotic correlation are transparent in the limit of weak coupling, $\beta J = 0$. With the additional simplification $h = 0$, each attempted spin flip is accepted with probability 1/2 based on the value of ξ_{acc} , regardless of the states of neighboring spins. In this case the steady state overlap can be calculated analytically. To do so, we derive an equation of motion for the probability $p(\tau)$ that a given spin has identical values in the reference and trial trajectories after τ MC steps. Note that τ differs from the unit of MC time, t , by a factor of N . The long-time, steady-state limit of this time evolution, $p_{\text{ss}} = \lim_{\tau \rightarrow \infty} p(\tau)$, yields $\langle \sigma \cdot \tilde{\sigma} \rangle_{\text{ss}} = 2p_{\text{ss}} - 1$. In Appendix B, we tabulate the various ways that a selected spin can become identical in reference and trial trajectories after a single timestep. From this

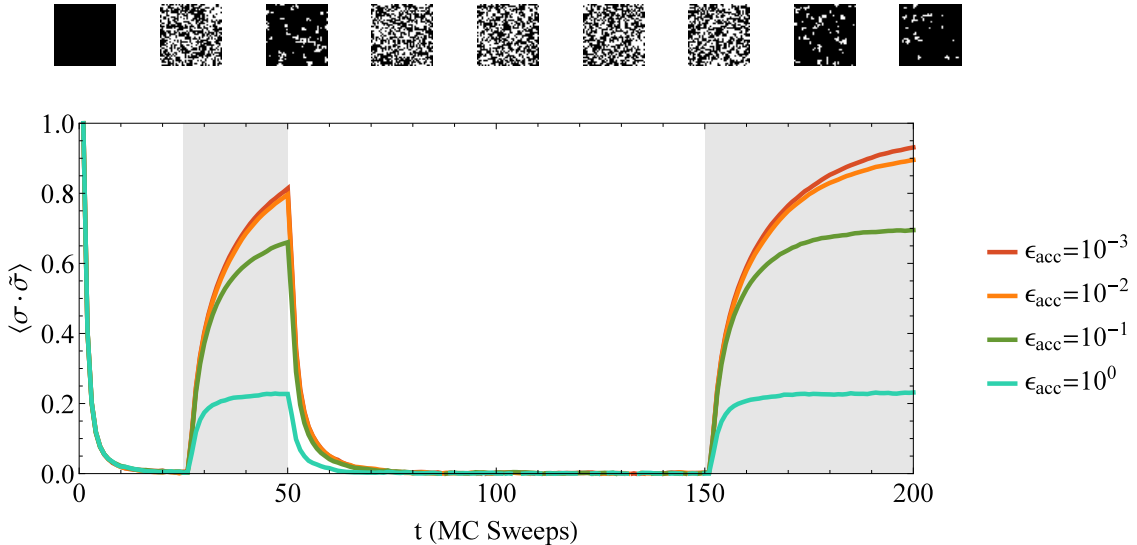


Figure 2.5: Correlation between reference and trial trajectories of a 40×40 Ising model with $\beta J = 0.3$. Plotted lines are averages over 500 independent pairs of trajectories that evolve by push up/push down dynamics. Noise histories of each pair are generated in a correlated manner with $\epsilon_{\text{site}} = \epsilon_{\text{dir}} = 10^{-3}$ during the intervals $t = 25 - 50$ and $t = 150 - 200$ (the shaded regions); noise guidance is absent at all other times. The site-wise correlation between an example trajectory pair (with $\epsilon_{\text{acc}} = 10^{-3}$) is shown above the graph, with time advancing from left to right and adjacent configurations separated by 25 MC sweeps.

enumeration, and the corresponding probabilities, we find

$$\begin{aligned} p(\tau + 1) = & \frac{N-1}{N} p(\tau) - \frac{\epsilon_{\text{dir}}}{4N} \left(1 - \epsilon_{\text{site}} + \frac{\epsilon_{\text{site}}}{N}\right) \left(1 - \frac{\epsilon_{\text{acc}}}{2}\right) \\ & + \frac{1}{2N} \left(1 - \frac{\epsilon_{\text{acc}}}{2}\right) \left(1 - \epsilon_{\text{site}} + \frac{\epsilon_{\text{site}}}{N}\right) p(\tau) + \frac{1}{2N}. \end{aligned} \quad (2.24)$$

The various terms of Eq. 2.24 describe the different ways that a single MC move can impact the state of an arbitrarily chosen spin in trial and reference trajectories. Since each move of our MC dynamics acts on a single site of the lattice, some moves do not involve the tagged spin at all, but instead some other lattice site; the first term in Eq. 2.24 reflects this possibility. The second term accounts for the decrease in overlap when reference and trial trajectories accept a spin-flip at the same site but in opposite directions. The third term results from the constructive action of correlated noises on the tagged spin, either maintaining existing correlation or inducing synchronization, as detailed in Appendix B. The final term accounts for random alignment of the tagged spin despite uncorrelated noise variables, a possibility particular to degrees of freedom with a limited number of discrete

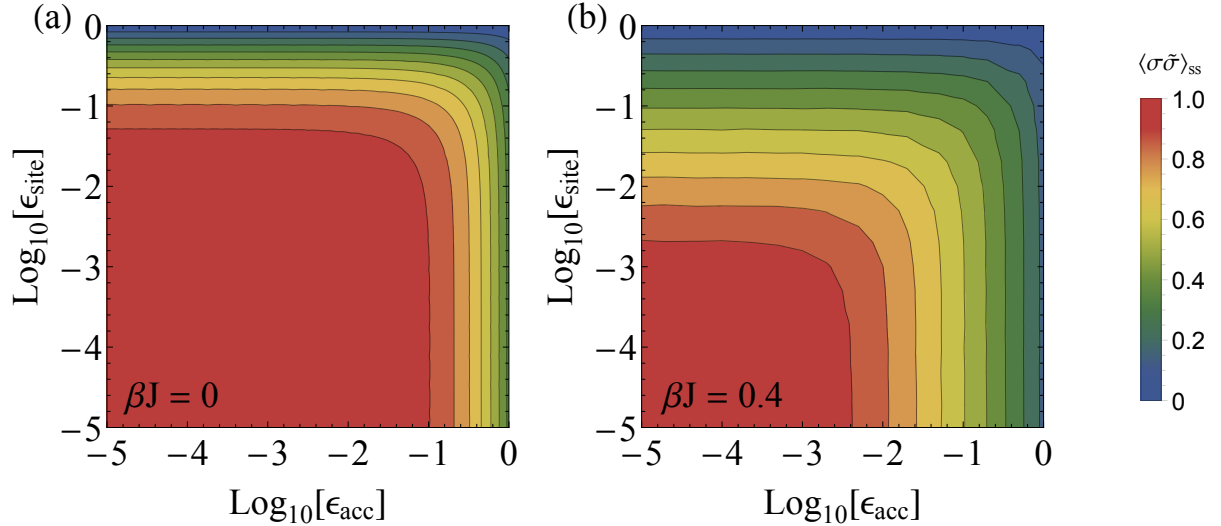


Figure 2.6: Steady state correlations between reference and trial trajectories of a 40×40 Ising model, as a function of noise guidance strength. Results are shown for push up/push down dynamics with $\epsilon_{\text{dir}} = 0.001$. The high-temperature limit Eq. 2.25 is shown in (a). Finite temperature behavior (b) was obtained by sampling 4×10^4 pairs of trajectories for 340 MC sweeps each, with $\beta J = 0.4$.

states. Equating $p(\tau)$ and $p(\tau + 1)$ gives the steady state probability,

$$p_{\text{ss}} = \frac{1 - \frac{\epsilon_{\text{dir}}}{2} \left(1 - \frac{\epsilon_{\text{acc}}}{2}\right) \left(1 - \epsilon_{\text{site}} + \frac{\epsilon_{\text{site}}}{N}\right)}{2 - \left(1 - \frac{\epsilon_{\text{acc}}}{2}\right) \left(1 - \epsilon_{\text{site}} + \frac{\epsilon_{\text{site}}}{N}\right)}. \quad (2.25)$$

Analytically calculating steady-state overlap at finite temperature is not straightforward. Numerical results, shown for $\beta J = 0.4$ in Fig. 2.6, indicate that the dependence of overlap on strengths of noise perturbation is generically similar to the $\beta J = 0$ case analyzed above. Increasing βJ from zero does, however, slow the rate of convergence to the steady state, while decreasing the degree of steady state correlation. For all coupling strengths we have examined, $\langle \sigma \tilde{\sigma} \rangle_{\text{ss}}$ can be made arbitrarily close to unity by decreasing the various ϵ parameters. This level of control ensures that one can generate trial trajectories which are correlated with a reference for all times, an essential capability for efficient path sampling of long trajectories.

WCA Dynamics

The success we have achieved in synchronizing Ising dynamics with noise guidance should not be expected for complex dynamical systems in general. We demonstrate this limitation for

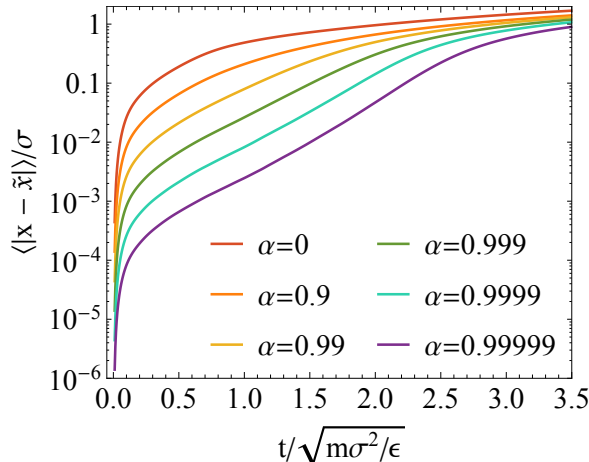


Figure 2.7: Divergence between reference and trial trajectories of a two-dimensional WCA fluid with Brownian tube noise guidance of strength α . Average distance between the two trajectories, as defined in Eq. 2.26, is shown for a system of 400 particles with mass m and diameter σ , in a square box with side length 24σ (i.e., density $\rho\sigma^2 = 0.694$). Underdamped Langevin dynamics was propagated with inverse temperature $\beta = 0.2$ and friction coefficient $\gamma = 0.1$ using a timestep of 0.005τ , where $\tau = \sqrt{m\sigma^2/\epsilon}$ and ϵ is the Lennard-Jones interaction energy scale [107]. Data are averaged over 500 independent trial trajectories.

the specific case of a two-dimensional WCA fluid [122] evolving by underdamped Langevin dynamics. The purely repulsive particles are propagated using an integration scheme that requires generating a collection of Gaussian random variables [9, 108]. These noises are guided by a Brownian tube proposal, Eq. 2.20. The similarity between trial and reference noise histories is controlled by a parameter α that ranges from zero (no noise guidance) to one (complete noise guidance).

Starting from identical initial configurations, we propagate dynamics with correlated noise histories and monitor the difference between trial and reference as

$$\langle |\mathbf{x} - \tilde{\mathbf{x}}| \rangle = \frac{1}{N} \sum_{i=1}^N |\mathbf{x}^{(i)} - \tilde{\mathbf{x}}^{(i)}|, \quad (2.26)$$

where $\mathbf{x}^{(i)}$ and $\tilde{\mathbf{x}}^{(i)}$ are the positions of particle i in the reference and trial and $|\cdot|$ is the two-dimensional Euclidean distance. At short times, the difference between trial and reference trajectories is small, but this difference grows exponentially, a hallmark of chaotic dynamics. Even with exceptionally strong noise guidance, trajectories cannot be held arbitrarily close to each other for long times, as shown in Fig. 2.7.

Why are we unable to guide the evolution of WCA particles as effectively as we guided Ising dynamics? A principal difference between the two systems is the likelihood of spontaneous local recurrences. In either case, trajectories with similar initial conditions but different noise histories wander away from one another in a global sense, eventually exploring very

different regions of configuration space. Correlating their noise histories generally acts to defer, but not defeat, this divergence. In the case of Ising dynamics, however, a given small block of adjacent spins will occasionally align spontaneously in two trajectories with reasonable probability. Following such a spontaneous, local recurrence, correlated noises again work to hold trajectories close. Global spontaneous recurrence of a large number of spins is, of course, highly improbable, but the noise guidance seems to “lock in” local correlations every time they spontaneously reoccur.

2.6 Conclusion

Transition path sampling has proven useful for a variety of equilibrium, as well as non-equilibrium, problems in chemical dynamics. The problem of sampling long trajectories, particularly those with multiple intermediates, has hindered a variety of extensions and applications of the methodology. We have outlined a modern physical perspective from which to assess and address these challenges. We have demonstrated and discussed successful trajectory guidance in the case of Monte Carlo dynamics of an Ising model. Substantial difficulties remain for systems with continuous degrees of freedom.

Our results suggest that effective noise guidance of long trajectories requires a nonnegligible probability of spontaneous local recurrence, i.e., a significant chance that reference and trial trajectories transiently align within small regions of space. Such synchronization could be particularly helpful for sampling reactive trajectories that traverse metastable intermediate states, for example the coarsening or assembly of colloidal systems as they organize on progressively larger scales. In such cases, trial trajectories in the course of path sampling should maintain correlations with the reference while passing through the intermediates, not just at the endpoints. Even without identifying metastable configurations, correlated noises could be applied during some intervals but not others. A tendency to synchronize would enable trial trajectories to explore widely during unguided periods, but to be reined in globally by intermittent guidance.

We anticipate that these noise-guidance methods will be effective for other lattice systems as well, but their usefulness could depend sensitively on the exact manner in which the noise influences dynamics. In particular, without incorporating directionality into proposed spin changes, we were not able to guide long Ising trajectories. Furthermore, Ising dynamics can exhibit spontaneous recurrence, i.e., transient local alignment between two trajectories regardless of their noise histories. Because small blocks of Ising spins can adopt only a modest number of configurations, such random local synchronization occurs with an appreciable probability. The probability of recurrence will likely be lower for models with a larger collection of possible local configurations, e.g., a Potts model or an Ising model with more neighbors. We thus expect that the application of noise-guided path sampling could face substantial challenges for long trajectories of these more intricate lattice models.

Chapter 3

Sampling Protocols

3.1 Introduction

In biology, chemistry, and materials science there is a widespread ambition to rationally engineer molecular systems. The common adage that structure determines function suggests that in order to design a molecular system with a particular functionality, our big challenge is to determine an appropriate structure. Unfortunately, even when we know the “right” structure, we do not necessarily know how to make it. In practice, coaxing molecules to assemble into a designed pattern is no less challenging than coming up with the design in the first place. As a tangible example, crystals with photonic bandgaps are understood theoretically but remain challenging to fabricate using either photolithography or colloidal self-assembly [92].

If we consider equilibrium experimental protocols, then the design problem is independent of molecular dynamics—we must engineer molecular interactions such that the desired structure is a minimum of free energy. However, free energy minimization is not an applicable design principle when we manipulate matter in a non-equilibrium manner. Frequently these non-equilibrium protocols happen out of experimental necessity, e.g., laser tweezers heat a medium, so they cannot be used in an equilibrium process [82]. Other times, we purposefully want to drive a system far from equilibrium to access molecular configurations that would be very uncommon in equilibrium. A temperature quench to form a glass is one example. Fig. 3.1 illustrates a second example, assembling a structure out of two types of colloidal particles, identical except that they are driven in opposite directions by an applied field [118]. In that example, the phase space of possible configurations can be partitioned into regions according to the mixing of the two types of colloids: one region is well-mixed, another forms crisp vertical stripes. Without the driving, a typical equilibrium trajectory primarily visits configurations in the well-mixed region. Subject to an appropriate periodic field, a trajectory that begins well-mixed, is strongly steered toward the vertical stripe region of phase space. This chapter addresses how we might identify the protocols which most strongly steer collective dynamics toward desired products.

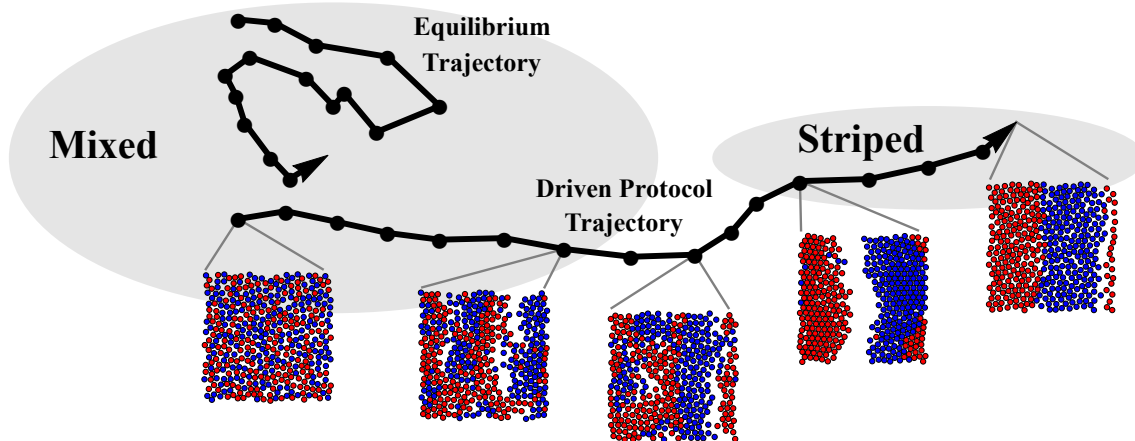


Figure 3.1: In equilibrium systems, the molecular configurations visited by a trajectory depend on designing interactions between particles. If we drive those same particles with out-of-equilibrium protocols, they can visit corners of phase space which are very atypical of equilibrium dynamics. By specifying only the desired final region of phase space, are there smart ways to discover the protocols which most effectively steer the dynamics toward the target? Inset images depict two-dimensional WCA particles evolving under a protocol which periodically pushes red and blue particles in opposite directions. For appropriate amplitudes and frequencies of driving, the particles tend to align in stripes.

To guide trajectories through phase space, we want to search the vast space of possible protocols, which are generically non-equilibrium. At face value this aim may seem a preposterous proposition. We can never try all possible protocols! A similar complaint could be raised, however, about sampling microscopic configurations in an Ising model or a hard sphere fluid: we could never enumerate all the microstates. In that context, we know that Monte Carlo sampling is immensely effective. While we never try all the possibilities, we *can* learn from representative sampling over the microstates. Can an analogous approach teach us about protocol spaces too vast to enumerate?

Suppose we want to sample protocols, with a preferential bias towards protocols that generate trajectories with particular properties, e.g., trajectories which are especially likely to evolve from mixed to striped configurations. The effort of scanning all the possible protocols scales horribly with the number of tunable parameters, so we consider a route to explore the space with a random walker (see Fig. 3.2). By simultaneously sampling the space of trajectories and protocols, we show that such a protocol search is possible, and, for certain systems, very advantageous. The efficacy of the methodology depends on the ability to efficiently sample trajectory spaces, so the limitations described in Chapter 2 must be considered. For that reason, we confine our study of protocol sampling to two models whose paths can be successfully sampled: a one-dimensional barrier crossing and two-dimensional Ising dynamics.

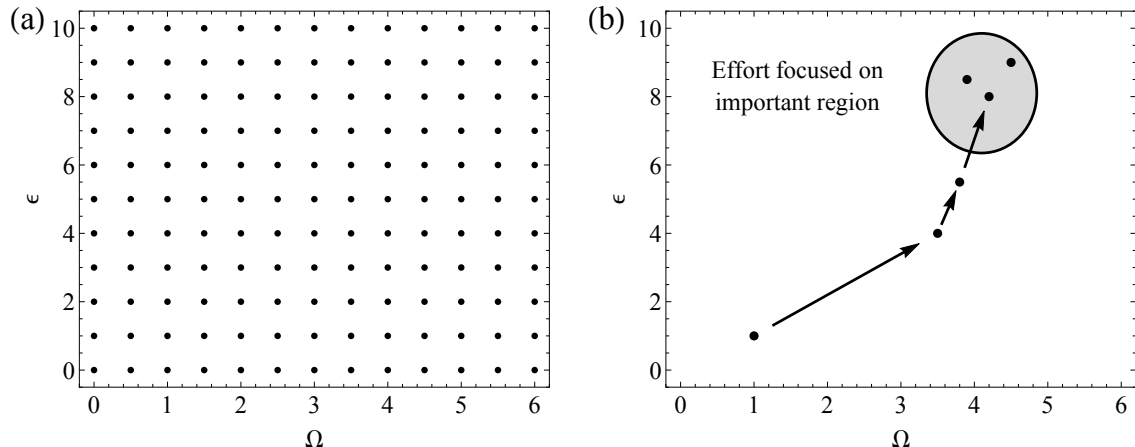


Figure 3.2: Suppose a protocol depends on two parameters, ϵ and Ω , as in the double well example introduced in Section 3.2. Scanning all possible protocols grows exponentially in the number of parameters. Alternatively, the space could be explored according to a random walk in protocol space. If we construct an appropriate dynamics for the random walker, effort can be focused on the protocols which are most significant.

3.2 Direct Sampling of Protocols: One-Dimensional Barrier Crossing

The conceptual problem of protocol sampling is straightforwardly illustrated in a one-dimensional toy model. Consider a particle of mass m , whose position r evolves according to an underdamped Langevin equation with friction coefficient γ ,

$$m\ddot{r} = -\nabla V(r, t) - \gamma\dot{r} + \sqrt{2\gamma k_B T}\xi(t). \quad (3.1)$$

The equation can be used to model the stochastic dynamics of a colloid in a liquid bath at temperature T when subjected to a time-dependent potential energy $V(r, t)$. As usual, k_B is the Boltzmann constant. The Langevin equation describes the effective motion of the single particle without explicitly representing the state of the bath. Rather than retaining many bath degrees of freedom, their effect is captured through a friction of the medium and a random force given by the white noise ξ with unit variance. We focus on dynamics in a quartic, double-well potential with an additional small perturbation, which is periodic in time. Specifically,

$$V(r, t) = \frac{a}{4}r^4 - \frac{b}{2}r^2 + \epsilon \sin(\Omega t)r, \quad (3.2)$$

where the positive constants a and b control the barrier height and the strength and periodicity of the external perturbation is determined by ϵ and Ω . If we set $a = 1$ and $b = 9$ to generate a $20k_B T$ barrier, then transitions from the left well (region A, defined by

$r < -\sqrt{b/3a}$) to right well (region B, defined by $r > \sqrt{b/3a}$) are rare events, and transitions from A to B are described by a first-order rate constant k_{AB} . Suppose we set the

$$V(r,t) = U(r) + \epsilon \sin(\Omega t)r$$

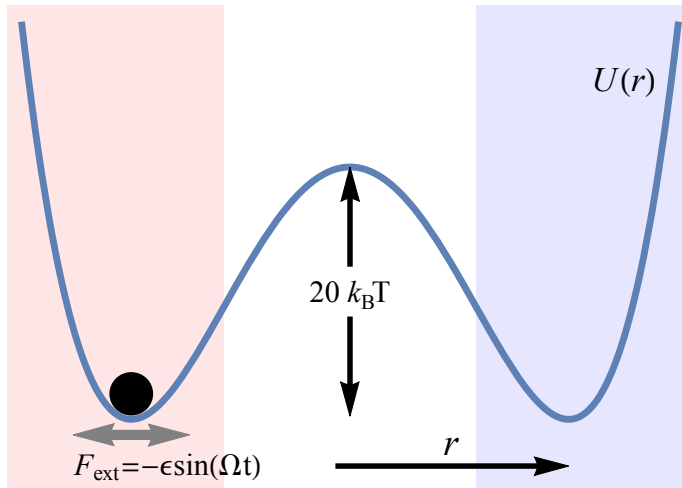


Figure 3.3: We investigate barrier crossing rates for a one-dimensional Langevin equation, assisted by a periodic external perturbation. We define the “A” and “B” regions for reactants and products, shaded red and blue, by the inflection points in the double well.

perturbation strength, ϵ , to the modest value of $2k_B T$. What frequencies Ω will amplify the transition rate k_{AB} ? When the bath only weakly dampens the inertial motion of the tracked particle, it is physically obvious that driving at the resonant frequency of a well, $\sqrt{2b/m}$, will facilitate transitions to the other side, but it is instructive to see how this answer can be found by different computational approaches. We start with the straightforward parameter scan, corresponding to Fig. 3.2(a).

Numerical Integration

To compute transition rates, we could simulate stochastic dynamics with different choices for ϵ and Ω . This simulation requires us to discretely propagate the particle according to the Langevin equation. We use an integrator, introduced by Manuel Athènes and Gilles Adjanor, which naturally treats forward and reversed dynamics in a symmetric manner [9]. As in the leapfrog integrator for molecular dynamics, we assign momenta at “half timesteps” for conceptual convenience. Each timestep requires the selection of two Gaussian random numbers, $\xi_{i+\frac{1}{4}}^+$ and $\xi_{i+\frac{3}{4}}^+$, which occur at quarter timesteps (the superscript + indicates that these noises propagate dynamics forward). We modify the integrator slightly to include a timestep rescaling factor, $c = \sqrt{\frac{2}{\gamma \Delta t} \tanh \frac{\gamma \Delta t}{2}}$, that recovers, for all possible timesteps Δt ,

the exact mean-squared displacement of a freely diffusing particle [107]¹.

Denoting the position and momenta at timestep i as r_i and p_i , respectively, we propagate the trajectory according to

$$\begin{aligned} p_{i+\frac{1}{2}} &= \left[p_i e^{-\gamma \Delta t / 2} + \xi_{i+\frac{1}{4}}^+ \right] + f_i \frac{c \Delta t}{2} \\ r_{i+1} &= r_i + p_{i+\frac{1}{2}} \frac{c \Delta t}{m} \\ p_{i+1} &= \left[p_{i+\frac{1}{2}} + f_{i+1} \frac{c \Delta t}{2} \right] e^{-\gamma \Delta t / 2} + \xi_{i+\frac{3}{4}}^+. \end{aligned} \quad (3.3)$$

The noises are each drawn from the distribution

$$P(\xi) = \frac{\beta}{\sqrt{2\pi} (1 - e^{-\gamma \Delta t}) m} e^{-\frac{\xi^2 \beta}{2(1 - e^{-\gamma \Delta t}) m}}, \quad (3.4)$$

where $\beta = (k_B T)^{-1}$. Brute force calculations of the transition rate for various choices of ϵ and Ω are accessible by counting the number of transitions per unit time observed over the course of many long trajectories. Representative trajectories, shown in Fig. 3.4, illustrate that transition rates are amplified for driving frequencies near the resonant frequency ($\Omega_0 \approx 4.24$ for $m = 1, b = 9$). When the barrier height is $20k_B T, m = 1, \gamma = 1$, and no driving field is applied, a typical trajectory transitions from region A to B once every 10^9 units of time. Obtaining a good estimate of such a small rate requires at least 10^{12} integration steps with a timestep of $\Delta t = 0.01$, a steep computational cost to observe ten transition events. In the next section, we show how a transition path sampling approach extracts relative transition rates (comparing the rate of one choice of Ω to another Ω') with much less computational effort.

3.3 Protocol Sampling in a TPS Framework

Brute force rate calculations directly measure the rarity of transitions, but most of the computational effort is expended in generating non-transitioning dynamics. For our purposes, it is wasteful to simulate details of the long waiting periods between transitions, so we make use of a shortcut to computing the transition rate. Provided the transitions are rare, each transition is independent of the previous crossing event, so the elapsed time between subsequent transitions, τ , is Poisson-distributed,

$$P(\tau) = k e^{-k\tau}, \quad (3.5)$$

with rate constant k [70]. The brute force calculation estimates k by computing the average time between transitions, $\langle \tau \rangle$. But because the waiting time distribution is Poissonian², it

¹The Athènes integrator would set $c = 1$. For small timesteps in the underdamped limit, $c = 1 - \mathcal{O}(\gamma^2 \Delta t^2)$, so the Athènes integrator is effectively equivalent to the time-rescaled form used here.

²To be careful we must put some timescale restrictions on the assertion of Poisson statistics. At very short times, subsequent events can be correlated. See Reference [25] for a more thorough discussion.

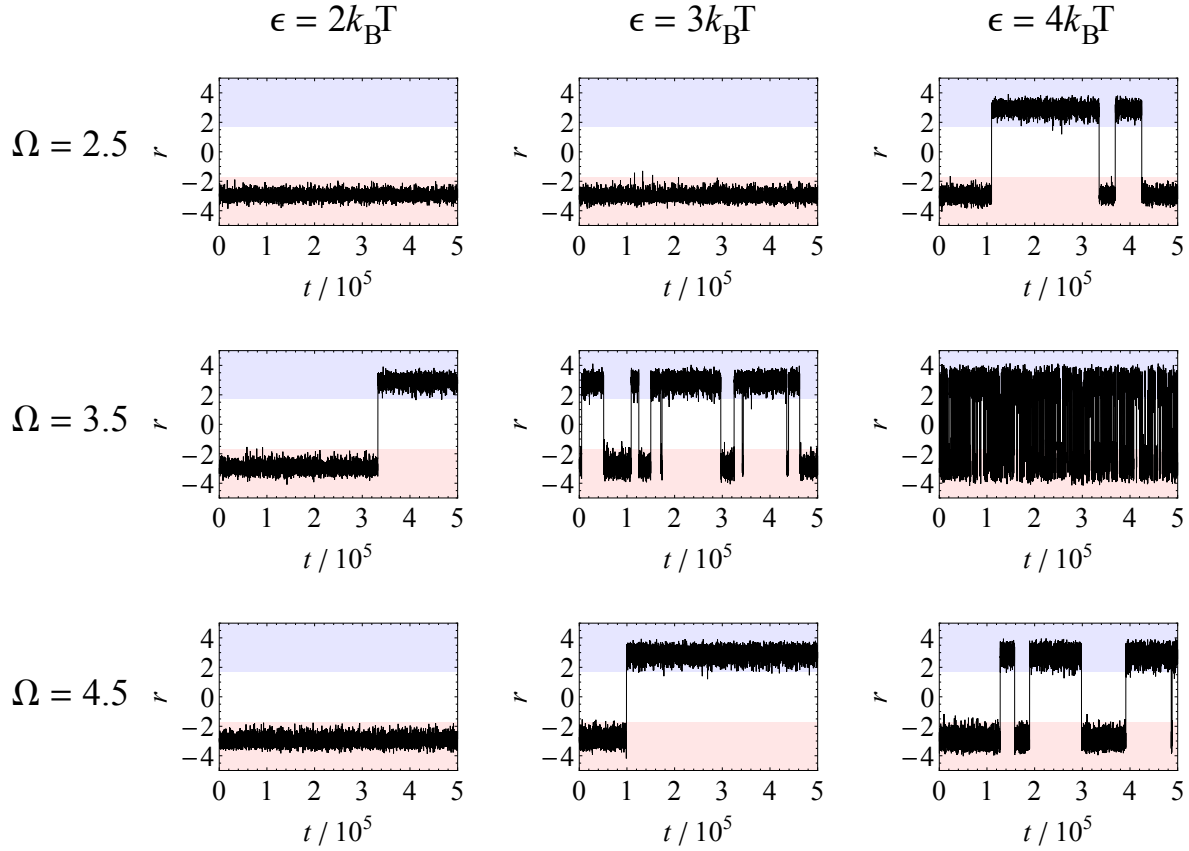


Figure 3.4: Representative trajectories for a variety of protocols. Trajectories are propagated as described in the text with $\Delta t = 0.01$, $\beta = 1$, $a = 1$, $b = 9$, $\gamma = 1$, $m = 1$.

is also possible to extract k by measuring the probability to observe an anomalously quick transition. In effect, we can skip the long waiting periods and focus our efforts on the transitions.

Instead of simulating very long trajectories, we restrict our attention to an ensemble of short trajectories of length t_{obs} with a constraint that the trajectories must transition from A to B. This collection of trajectories is the reactive ensemble discussed in Chapter 2, Eq. (2.6). Let the time required for a particle to climb up and over the barrier be t_{cross} . We choose an observation time long enough that a particle has time to climb up and over the barrier, but short enough that we exclude most of the waiting time between transitions: $t_{\text{cross}} < t_{\text{obs}} \ll k^{-1}$. This biased trajectory ensemble is sampled as discussed in Chapter 2 using correlated noise histories. Briefly, we start from a seed trajectory which transits from A to B and propose trial trajectories using shooting moves with correlated noise histories. Trials are accepted only if they exhibit a transition. Technical details are included in Appendix C. This Monte Carlo sampling of trajectory space yields a representative collection of possible

transition routes, as plotted in Fig. 3.5(a). In this one-dimensional example, transition paths differ most noticeably by the time of the transition, but in many body systems multiple crossing mechanisms can be sampled [52].

We obtain the transition rate constant by quantifying the small probability that an unbiased trajectory of length t_{obs} will exhibit a transition. This probability can be computed as a free energy calculation in trajectory space, the “reversible work” to constrain trajectories to start in A and end in B [21]. We extract the relative transition rates between different protocols even more simply. Consider the extended ensemble,

$$P_{\text{extended}}[r(t), \Omega] \propto P_0[r(t)|\Omega] h_A(r_0) h_B(r_{t_{\text{obs}}}), \quad (3.6)$$

analogous to Eq. (3.6), but now sampling both trajectories and protocols. As in Chapter 2, h_A and h_B are indicator functions which identify whether or not the particle is in regions A and B, respectively. $P_0[r(t)|\Omega]$ is the probability that trajectory $r(t)$ is generated by propagating Eqs. (3.3) with driving frequency Ω , given an initial Boltzmann distribution in the equilibrium state with $\Omega = 0$ (equivalently $\epsilon = 0$). This extended ensemble is sampled as in ordinary TPS but with an additional MC move that attempts changes to Ω (details in Appendix C). Fig. 3.5(b) shows that the protocols with the highest transition rates are visited most frequently by the MCMC process.

In fact, the Markov chain samples protocols in proportion to the frequency-dependent transition rate, $k(\Omega)$,

$$P(\Omega) \equiv \int \mathcal{D}r(t) P_{\text{extended}}[r(t), \Omega] \propto k(\Omega). \quad (3.7)$$

To demonstrate this feature, we first note that the MC moves altering Ω naturally sample the marginal distribution found by averaging over the trajectories,

$$P(\Omega) \propto \langle h_A(r_0) h_B(r_{t_{\text{obs}}}) \rangle_\Omega, \quad (3.8)$$

The notation $\langle \cdot \rangle_\Omega$ represents an average over trajectories of length t_{obs} with driving frequency Ω , so the quantity $\langle h_A(r_0) h_B(r_{t_{\text{obs}}}) \rangle_\Omega$ is the probability of observing a transition in time t_{obs} , driven at frequency Ω . This transition probability is simply related to the rate constant via the Poisson distribution for the time until the next transition event. Namely, the probability of observing a transition in time t_{obs} is provided by

$$\langle h_A(r_0) h_B(r_{t_{\text{obs}}}) \rangle_\Omega = \int_0^{t_{\text{obs}}} dt k(\Omega) e^{-k(\Omega)t} = 1 - e^{-k(\Omega)t_{\text{obs}}} \stackrel{k(\Omega)t_{\text{obs}} \ll 1}{\sim} k(\Omega)t_{\text{obs}}, \quad (3.9)$$

where we have used the fact that t_{obs} is much smaller than the typical transition time k^{-1} . Therefore, the relative probability of sampling Ω and Ω' in the extended ensemble is given by

$$\frac{P(\Omega)}{P(\Omega')} \stackrel{k t_{\text{obs}} \ll 1}{\sim} \frac{k(\Omega)}{k(\Omega')}. \quad (3.10)$$

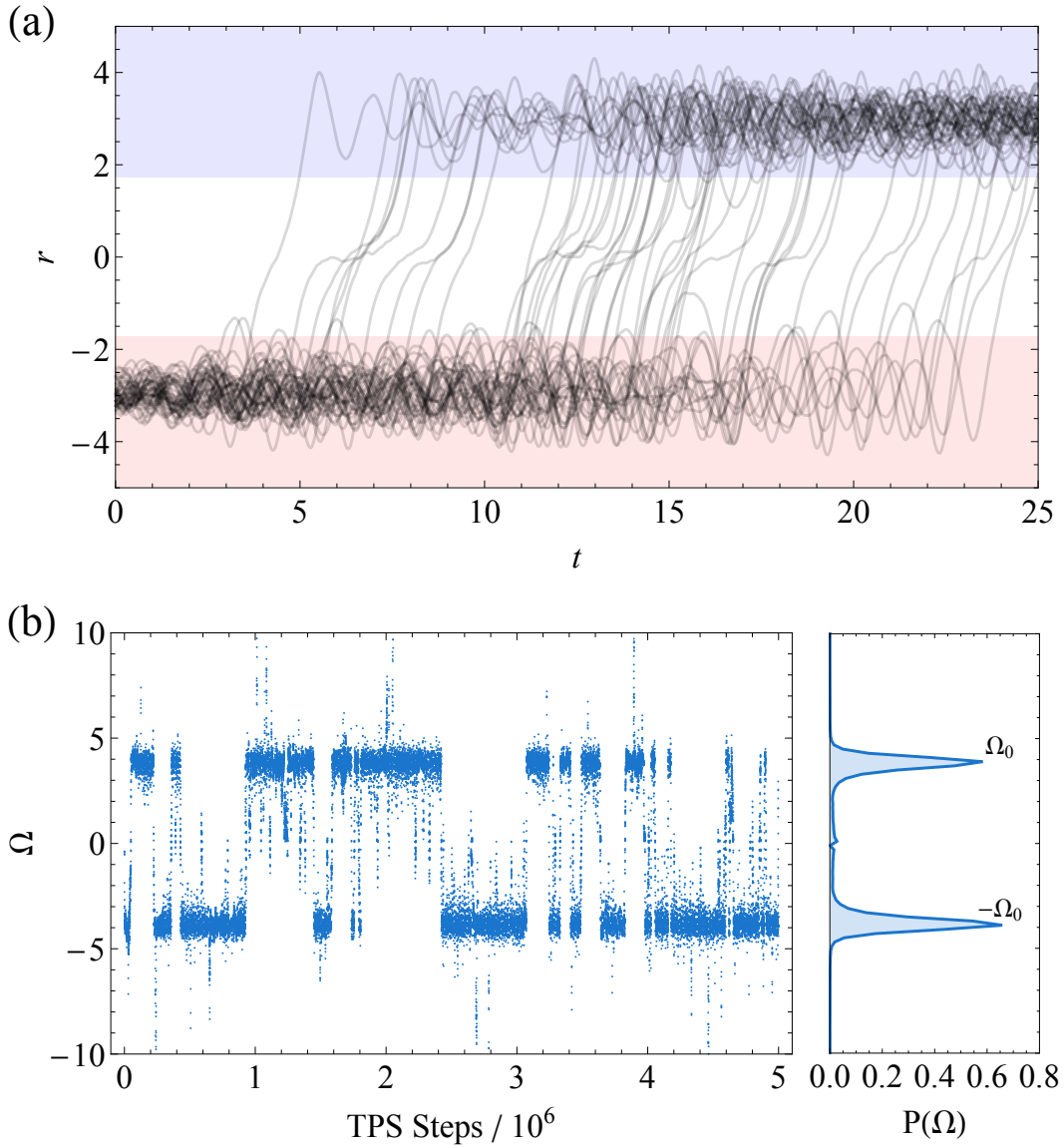


Figure 3.5: Extended ensemble path sampling performs a MCMC dynamics through the space of paths and protocols. Some TPS moves perturb the trajectory, $r(t)$, with noise-guidance TPS moves (the parameter α , introduced in Chapter 2 was set to 0.95). Other TPS moves symmetrically propose a change to the driving frequency, Ω , and generate a new trajectory with that driving frequency, again with noise guidance. Details of the MCMC move set are discussed in Appendix C. Fig. (a) shows the sampling of double-well transitions over a $20k_B T$ barrier ($\Delta t = 0.01, \beta = 1, a = 1, b = 9, \gamma = 1, m = 1, \epsilon = 2$). Fifty representative trajectories are shown with 50,000 TPS moves between each recorded trajectory. Fig. (b) shows the simultaneous sampling of protocols, with Ω recorded every 100 TPS moves. Frequencies are visited in proportion to the transition rate for that choice of Ω .

Using the extended ensemble to sample protocols in proportion to transition rates can serve two purposes. In high-dimensional protocol spaces, it acts as an exploratory tool. The Markov chain wanders through the vast space, tending toward parameters with larger rate constants. When the protocol space has few parameters, the method also provides an efficient way to quantitatively compare the rate constants of different protocols. For example, umbrella sampling allows us to compute the relative double well transition rates for various driving frequencies, shown in Fig. 3.6. The relative transitions rates agree with the brute force rate calculation, with one notable exception. When the period of external driving is long compared to t_{obs} , the extended ensemble approach cannot be expected to reproduce the transition rates since the simulated short trajectories are not driven for a complete period.

3.4 Sampling with a Meta-dynamics on Trajectory Space

We have argued that in order to efficiently extract rate constants we should sample trajectories with a short t_{obs} , thereby avoiding the simulation of uninteresting, and computationally expensive, dynamics leading up to the transition. From a path sampling perspective, the use of a short observation time is fortunate. In Chapter 2, we saw that long- t_{obs} trajectories are particularly hard to sample, but that analysis does not apply to short observation times. Does this mean that path sampling will work efficiently whenever we want to sample transitions in the extended ensemble? Unfortunately, the answer is a resounding no. To clarify, we must become more precise in our use of *short* and *long* to describe the trajectory lengths.

The lesson of the previous section is indeed that efficiency gains are expected when we sample a trajectory ensemble with short t_{obs} , where by “short t_{obs} ” we mean that $kt_{\text{obs}} \ll 1$. We cannot, however, make t_{obs} arbitrarily short; it must be at least as long as the time it takes to cross the barrier, t_{cross} . Barrier crossings which are rare but fleeting, those processes with very fast crossing times but slow rate constants, are good candidates for TPS methods; a small observation time can be chosen which simultaneously satisfies $t_{\text{cross}} < t_{\text{obs}} \ll k^{-1}$. Slower crossings, e.g., those with many intermediates and those requiring nanoparticles to diffuse large distances, still typically exhibit a separation of timescales, $t_{\text{cross}} \ll k^{-1}$. In principle the extended ensemble approach, with $t_{\text{obs}} > t_{\text{cross}}$, applies equally well to those slower processes, but in practice the value of t_{obs} must be large enough that path sampling becomes problematic for the reasons described in Chapter 2.

When shooting moves fail to sample paths, there is an alternative method for exploring trajectory spaces [33]. A transition pathway can be treated like a long polymer, and a dynamics can be defined such that propagation of the “polymer” samples the trajectory space. The trajectory meta-dynamics, not to be confused with the metadynamics method for free energy calculations, is computationally expensive, so it has largely been superseded by shooting. Nevertheless, when exploring protocol space is the primary goal, the method could be of practical use because it can simultaneously yield equations of motion for the trajectory

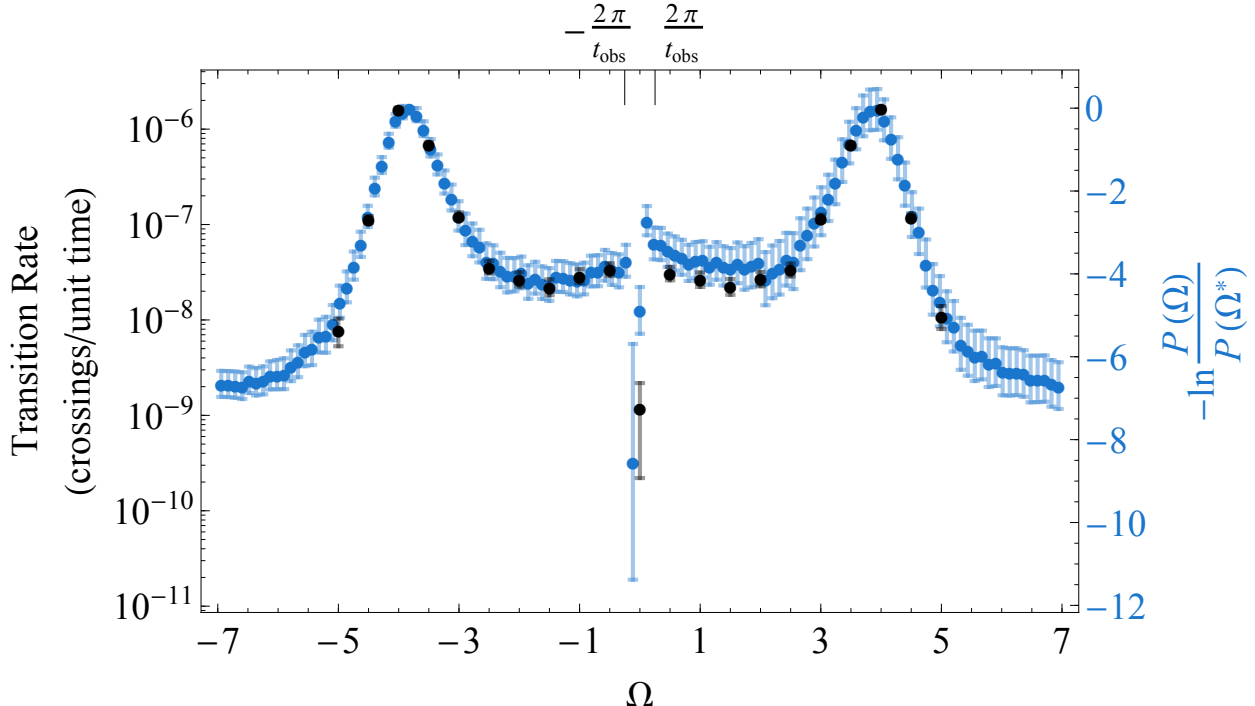


Figure 3.6: Dependence of the transition rate on the driving frequency as computed by brute force sampling from long trajectories (black) and extended ensemble path sampling (blue). At each value of Ω , rate constants are obtained from brute force sampling by counting the transitions in 5×10^6 trajectories with 1000 units of time each ($\Delta t = 0.01, \beta = 1, a = 1, b = 9, m = 1, \gamma = 1, \epsilon = 2$). Relative rate constants are computed from extended ensemble sampling with $t_{\text{obs}} = 25$. By measuring the brute force rate constant for the optimal driving frequency, Ω^* , the relative rates can be converted into absolute rates. To exhaustively sample the different driving frequencies, we employed umbrella sampling, biasing the log probability using 15 evenly spaced harmonic biases with curvature 3.25. 10^7 TPS moves were performed in each umbrella using noise guidance with $\alpha = 0.95$ (see Appendix C for more technical details). The driving frequency was sampled every 2000 TPS moves, and these biased samples were stitched together using the Multistate Bennet Acceptance Ratio (MBAR) method [105]. Reported error bars are twice the variance.

and for the protocol. Trajectory meta-dynamics proceeds slowly, like a long polymer diffusing through a viscous medium, but the meta-dynamics through protocol space can comparatively fast. When meta-motion of paths and protocols proceeds with separate timescales, the protocol can locally equilibrate before the trajectory makes an appreciable change. In that case, protocol sampling can provide a sort of quenched average, comparing relative transition rates for different protocols, conditioned upon the slowly-evolving transition pathway.

To construct the meta-dynamics of the trajectory, it is useful to first review the manner in which polymers sample configuration spaces as they evolve dynamically. Suppose a long polymer, whose configuration is denoted by x , has a potential energy function $V_{\text{polymer}}(x)$. One way to sample the polymer's equilibrium distribution, $P(x) \propto e^{-\beta V_{\text{polymer}}}$ is to propagate dynamics, thermostated to maintain inverse temperature β , using forces given by the gradients of the potential energy, $-\nabla V$. In this particular example, the temperature, potential energy, and forces have physical meanings, but more generically we may apply an isomorphic dynamical scheme to sample arbitrary probability distributions. We can sample the extended ensemble in this way, with the effective potential energy for a trajectory/protocol pair given by the path action³,

$$S[r(t), p(t), \Omega] = -\ln P_{\text{extended}}[r(t), p(t), \Omega]. \quad (3.11)$$

This path action can be expressed explicitly in terms of the positions and momenta at every discrete timestep of the Langevin equation. For our choice of integrator, it is more compactly expressed in terms of the noises,

$$\begin{aligned} S[r(t), p(t), \Omega] = & \text{Const.} + \beta \left(V(r_0) + \frac{p_0^2}{2m} \right) - \ln h_A(r_0) - \ln h_B(r_{t_{\text{obs}}}) \\ & + \frac{\beta}{2(1 - e^{-\gamma \Delta t})m} \sum_{i=0}^{\frac{t_{\text{obs}}}{\Delta t} - 1} \left[\left(\xi_{i+\frac{1}{4}} \right)^2 + \left(\xi_{i+\frac{3}{4}} \right)^2 \right]. \end{aligned} \quad (3.12)$$

Gradients of the path action with respect to all trajectory/protocol degrees of freedom (r and p at every timestep as well as Ω) are the forces for the meta-dynamics. To carry out Hamiltonian mechanics with these forces, we must also introduce momenta and fictitious masses for each degree of freedom. Thus the trajectory/protocol system evolves under Hamiltonian

$$H[r(t), p(t), \Omega, \pi^r(t), \pi^p(t), \pi^\Omega] = S[r(t), p(t), \Omega] + \frac{(\pi^\Omega)^2}{2M_\Omega} + \sum_{i=0}^{\frac{t_{\text{obs}}}{\Delta t} - 1} \left(\frac{(\pi_i^r)^2}{2M_x} + \frac{(\pi_i^p)^2}{2M_p} \right), \quad (3.13)$$

where the conjugate momenta are denoted by π 's and the fictitious masses by M 's⁴. In practice, this Hamiltonian can be propagated with Verlet or Nosé-Hoover integrator, thermostatted to sample with an inverse temperature of the meta dynamics of $\beta_{\text{meta}} = 1$.

Formally, the transition pathway dynamics samples the extended ensemble, so the marginal distribution $P(\Omega)$ that remains after integrating over all paths must be the same as the $P(\Omega)$ distributions we found using shooting moves in Fig. 3.6. Carrying out meta-dynamics on the trajectories, however, is not an efficient way to explore unique transition paths. We

³Here, the path probability depends on the momenta at every time, $p(t)$, which we had integrated out in the earlier section.

⁴The characteristic functions, h_A and h_B are step functions, so they must be softened to avoid impulsive forces. This is easily achieved by, e.g., replacing the step function with a Fermi function.

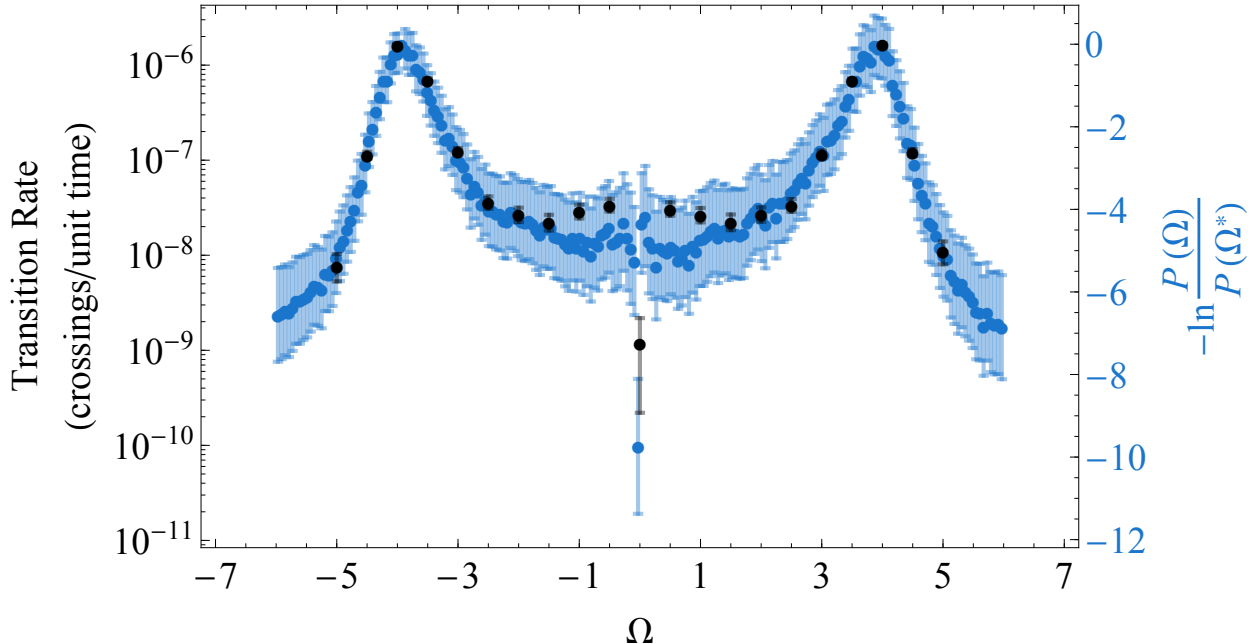


Figure 3.7: Dependence of the transition rate on the driving frequency as computed by brute force sampling from long trajectories (black) and using the dynamical scheme for sampling the extended ensemble (blue). The dynamical sampling scheme does not efficiently sample the trajectory space, but as discussed in the text, it could allow for exploration when other path sampling methods fail. To confirm that such dynamical sampling would be statistical unbiased, the method was used to exhaustively sample double well transitions. The brute force rate constants are the same as in Fig. 3.6. Relative rate constants are computed from the extended ensemble sampling with $t_{\text{obs}} = 50$ with a larger timestep, $\Delta t = 0.1$, to aid the sampling. Obtaining decorrelated samples of the rare values of Ω was challenging, so umbrella sampling was employed with a variety of locations and strengths of harmonic biases: (a) 40 harmonic biases evenly spaced from $\Omega = -6$ to $\Omega = 6$ with curvature 50, (b) 75 harmonic biases from $\Omega = -6$ to $\Omega = 6$ with curvature 70, (c) harmonic biases with curvature 2000 placed at $\Omega = -0.035$ and $\Omega = -0.06$, and (d) 10 evenly spaced biases from $\Omega = -6$ to $\Omega = 6$ with curvature 0.2. Each of the four sets of simulations included replica exchange MC moves that swapped replicas between neighboring harmonic biases. The values of $r(t)$, $p(t)$, and Ω were propagated according to the Hamiltonian, Eq. (3.13), using Hybrid Monte Carlo with a Verlet integrator and an Andersen thermostat for 2×10^9 timesteps of size 0.0005 (resampling of highly correlated momenta, π^r , π^p , π^Ω , every 2×10^5 steps, all fictitious masses set to unity). The small timestep was necessary due to stiff coupling between neighboring Langevin timesteps. The data from all umbrellas was subsampled to take only statistically independent samples of the driving frequency, and all of the subsampled data was combined using MBAR. Reported error bars are twice the variance.

must sample the Hamiltonian in Eq. (3.13) with timesteps small enough that the integrator remains stable. In practice, we find, as others have before, that the requisite timestep for transition path dynamics results in very slow path space sampling. Despite slow path sampling, Ω can evolve toward the optimal driving frequency quickly. The speed of Ω dynamics indicates that, in this example, exhaustive averaging over paths $r(t)$ is not necessary to discover optimal protocols. Sampling akin to a quenched protocol average, in which $r(t)$ stays near its initial transition path, captures the essential protocol-dependence of the transition rates. More fully sampling the paths will undoubtedly be important to more complex, higher-dimensional problems, but this dynamical sampling of paths and protocols could still provide a useful, if slightly uncontrolled, method for identifying protocols which amplified transition rates.

3.5 Finding Low-dissipation Protocols

In the previous sections, we saw that transition rates in a double well potential could be amplified by periodic driving, but this non-equilibrium process comes with an energetic cost. The oscillatory force performs work on the particle, some of which is dissipated to the environment, and the rate of dissipation depends sensitively on the protocol driving the non-equilibrium process. Managing this dissipative cost is a crucial design principle in both physical and algorithmic processes. In physical processes, any excess dissipation indicates that energy is being wasted to heat the environment. More abstractly, Chapter 2 showed how Monte Carlo moves can be thought of in the language of non-equilibrium statistical mechanics, and efficient Monte Carlo moves correspond to protocols that attempt to drive the Markov chain with nominal dissipation. Here, we show how the extended ensemble TPS methods can be adapted to incorporate a bias that prefers these low-dissipation protocols.

Our adaptation retains an essential component of extended ensemble protocol sampling—we evaluate the desirability of a protocol based on the behavior of a single trajectory. When extracting relative rate constants, we preferred values of Ω with large transition rates by accepting or rejecting altered driving frequencies based on whether or not a new short trajectory passed from A to B. While comparing two short trajectories, driven at frequencies Ω and Ω' , is insufficient to decide which driving frequency has a faster transition rate, the correct decision can be made *on average*. Just as we could not determine a rate constant from a single short trajectory, we cannot use a single trajectory to extract the dissipative cost, an ensemble property that requires us to average over all trajectories. Nevertheless, a single trajectory dissipation can be defined such that the average dissipation is coincident with macroscopic notions of dissipation [103]. This single-trajectory dissipation, also known as the entropy production of the trajectory, is given by

$$\omega[\mathbf{x}(t), \Lambda(t)] = \ln \frac{P_0[\mathbf{x}(t)|\Lambda(t)]}{P_0[\hat{\mathbf{x}}(t)|\hat{\Lambda}(t)]}, \quad (3.14)$$

where the forward and reversed trajectories are $\mathbf{x}(t)$ and $\hat{\mathbf{x}}(t)$. The protocol $\Lambda(t)$ and

reversed-time protocol $\hat{\Lambda}(t)$ could be a periodic driving as before, or they can denote more complex time-dependent protocols. We show that by biasing trajectories and protocols based on the *single-trajectory* entropy production, we can, in effect, sample a protocol ensemble which is biased to curtail the average dissipation.

The macroscopic dissipation associated with protocol $\Lambda(t)$ is given by the average over the trajectory ensemble,

$$\langle \omega \rangle_{\Lambda} = \int \mathcal{D}\mathbf{x}(t) P_0[\mathbf{x}(t)|\Lambda(t)] \omega[\mathbf{x}(t), \Lambda(t)]. \quad (3.15)$$

To study the protocols with little dissipation, we therefore choose to investigate the distribution

$$P_{\gamma}[\Lambda(t)] \propto e^{-\gamma \langle \omega \rangle_{\Lambda}}, \quad (3.16)$$

where γ is a parameter controlling the strength of biasing ⁵. In the limit that γ becomes infinite, the probability accumulates at the minimum-dissipation protocol, Λ^* . With finite γ , protocols which are near optimal retain non-vanishing probability. We will see in the next section that these protocol ensemble fluctuations teach us which aspects of the protocol must be controlled most sensitively to reduce dissipation. However, we first need a method to sample the protocol distribution, Eq. (3.16). The straightforward approach would construct a Markov chain in Λ -space; $\langle \omega \rangle_{\Lambda}$ would act like an effective energy for each protocol and γ an inverse temperature. Unfortunately, we can only compute $\langle \omega \rangle_{\Lambda}$ by averaging over all trajectories with fixed Λ . It is tempting to replace the average by the sample mean of n trajectories,

$$\langle \omega \rangle_{\Lambda} = \int \mathcal{D}\mathbf{x}(t) P_0[\mathbf{x}(t)|\Lambda(t)] \omega[\mathbf{x}(t), \Lambda(t)] \approx \sum_{i=1}^n \omega[\mathbf{x}_i(t), \Lambda(t)], \quad (3.17)$$

where $\mathbf{x}_i(t)$ is the i^{th} trajectory sampled from $P_0[\mathbf{x}(t)|\Lambda(t)]$. If we make this approximation, the effective energy in our MC procedure has errors due to finite sampling, and these errors are exponentiated in Eq. (3.16). This problem of sampling exponential distributions with a noisy energy function has been considered in several contexts [7, 11, 12, 24, 80]. Inspired by the “pseudo-marginal approach” [7], we propose that Eq. (3.16) can be sampled as the marginal distribution of a joint distribution,

$$P_{\lambda}[\mathbf{x}(t), \Lambda(t)] \propto P_0[\mathbf{x}(t)|\Lambda(t)] e^{-\lambda \omega[\mathbf{x}(t), \Lambda(t)]}. \quad (3.18)$$

The parameter λ controls the strength of biasing on the single-trajectory dissipation ω , while γ biases the average dissipation $\langle \omega \rangle_{\Lambda}$. Note that $P_{\lambda=0}$ is the same distribution as P_0 , the previously-defined distribution of natural dynamics. The joint distribution in Eq. (3.18) can be sampled without error since the distribution depends on ω , which, unlike $\langle \omega \rangle_{\Lambda}$, can be computed exactly at every MC step.

⁵Choosing to sample this distribution means we are using a uniform distribution over the protocols as a prior.

In a linear response limit of slow protocols operating over long times, the marginal distribution is simply related to Eq. (3.16). The trajectory can be subdivided into τ independent segments, and the total entropy production $\omega[\mathbf{x}(t), \Lambda(t)]$ is the sum of the entropy production of each segment. For sufficiently large τ , we expect the total entropy production of the trajectory to be Gaussian distributed on central limit theorem grounds, so

$$P(\omega|\Lambda(t)) \propto e^{-(\omega - \langle \omega \rangle_\Lambda)^2/(2\langle \delta\omega^2 \rangle_\Lambda)}, \quad (3.19)$$

where $\delta\omega \equiv \omega - \langle \omega \rangle_\Lambda$. For this Gaussian form, the entropy production fluctuation theorem, Eq. (2.3), requires that $2\langle \omega \rangle_\Lambda = \langle \delta\omega^2 \rangle_\Lambda$ ⁶. Therefore, in the linear response regime, we can replace an integral over trajectory space by a Gaussian integral over possible single-trajectory dissipations,

$$\begin{aligned} P_\lambda[\Lambda(t)] &\propto \int \mathcal{D}\mathbf{x}(t) P_0[\mathbf{x}(t)|\Lambda(t)] e^{-\lambda\omega[\mathbf{x}(t), \Lambda(t)]} \\ &\propto \int d\omega P(\omega|\Lambda(t)) e^{-\lambda\omega} \\ &\propto \int d\omega e^{-(\omega - \langle \omega \rangle_\Lambda)^2/(4\langle \omega \rangle_\Lambda)} e^{-\lambda\omega} \\ &\propto e^{-\lambda(1-\lambda)\langle \omega \rangle_\Lambda}. \end{aligned} \quad (3.20)$$

By sampling from the joint distribution we effectively sample protocols in proportion to an exponential of their average dissipation as in Eq. (3.16) with $\gamma = \lambda(1 - \lambda)$. The argument holds away from linear response provided $P(\omega|\Lambda(t))$ is well-approximated by Eq. (3.19) for values of ω near $\omega = (1 - 2\lambda)\langle \omega \rangle$. Notably, the scheme exerts a maximal bias, $\gamma = 1/4$, on the average dissipation when $\lambda = 1/2$. For $\lambda > 1/2$, the single-trajectory entropy production is biased so strongly that typically sampled trajectories have negative entropy production. Though even if the λ -biasing is strong enough that ω is typically negative, the average dissipation, $\langle \omega \rangle_\Lambda$, remains positive.

To understand why γ does not grow monotonically with λ , it is instructive to consider the case that $\lambda = 1$. For that choice of bias, the probability of sampling a trajectory from $P_{\lambda=1}[\mathbf{x}(t), \Lambda(t)]$ equals the probability of sampling its time-reversal using natural dynamics and a time-reversed protocol,

$$P_{\lambda=1}[\mathbf{x}(t), \Lambda(t)] \propto P_0[\mathbf{x}(t)|\Lambda(t)] e^{-\omega[\mathbf{x}(t), \Lambda(t)]} = P_0[\hat{\mathbf{x}}(t)|\hat{\Lambda}(t)]. \quad (3.21)$$

The second equality is a simple rearrangement of Eq. (3.14). Note, also from Eq. (3.14), that the single-trajectory dissipation can be negative, and the dissipation of a trajectory, $\omega[\mathbf{x}(t), \Lambda(t)]$ is equal and opposite the dissipation of the time-reversed trajectory, $\omega[\hat{\mathbf{x}}(t), \hat{\Lambda}(t)]$. The dissipation of a typical trajectory, sampled from the $\lambda = 1$ ensemble, is therefore opposite in sign from the dissipation of a typical trajectory generated with natural dynamics

⁶This uses the fact that the dissipation distributions for forward and reversed protocols are the same in the linear response regime.

and the time-reversed protocol. Since trajectories simulated using natural dynamics must have positive average dissipation, following from a restatement of the second law, we see that the $\lambda = 1$ ensemble typically produces trajectories with negative dissipation. The λ bias was introduced to reduce the typical value of $\omega[\mathbf{x}(t), \Lambda(t)]$, but this reduction can be achieved in two different ways: we may alter the protocol such that $\langle \omega \rangle_\Lambda$ decreases or we may alter the trajectory so it “runs backwards in time” and achieves a negative dissipation. We seek the first method of reducing ω , but when the λ bias exceeds a strength of $1/2$, the second strategy becomes more important. Thus the strength of the effective bias acting on $\langle \omega \rangle_\Lambda$ decreases as λ increases beyond $\lambda = 1/2$. In fact, both Eq. (3.20) and Eq. (3.21) make it explicit that the $\lambda = 1$ ensemble samples the protocols uniformly, without regard to the average dissipation.

The $\gamma \leq 1/4$ limitation can be overcome by constructing a joint distribution over the protocols and a set of n trajectories. In particular, we can sample from

$$P_{n,\lambda} [\{\mathbf{x}(t)\}_{i=1}^n, \Lambda(t)] \propto \prod_i P_0[\mathbf{x}_i(t)|\Lambda(t)] e^{-\frac{\lambda}{n}\omega[\mathbf{x}_i(t), \Lambda(t)]}. \quad (3.22)$$

In intuitive terms, while it may be possible to harvest one negative-entropy trajectory, it is much harder to simultaneously harvest n of them. Marginalizing over the trajectories yields

$$\begin{aligned} P_{n,\lambda}[\Lambda(t)] &\propto \left(\int \mathcal{D}\mathbf{x}_i(t) P[\mathbf{x}_i(t)|\Lambda(t)] e^{-\frac{\lambda}{n}\omega[\mathbf{x}_i(t), \Lambda(t)]} \right)^n \\ &\propto \left(\int d\omega e^{-(\omega - \langle \omega \rangle_\Lambda)^2/(4\langle \omega \rangle_\Lambda) - \frac{\lambda\omega}{n}} \right)^n \\ &\propto \left(e^{-\frac{\lambda}{n}(1-\frac{\lambda}{n})\langle \omega \rangle_\Lambda} \right)^n \\ &= e^{-\lambda(1-\frac{\lambda}{n})\langle \omega \rangle_\Lambda}. \end{aligned} \quad (3.23)$$

The first line again assumes a Gaussian dissipation distribution, which can be justified in a linear response regime as before ⁷. By increasing the number of trajectories, n , the average dissipation can be biased more strongly, with $\gamma = \lambda(1 - \frac{\lambda}{n})$. In the limit $n \rightarrow \infty$, we see that $\lambda = \gamma$ because the sample mean in Eq. (3.22) converges to the average, but we have shown that it is not necessary to compute the (expensive) converged averages. By adjusting λ appropriately, we can effectively bias the mean dissipation by sampling a finite, and potentially small, number of trajectories.

⁷ To pass from the second to third line we need only that $P(\omega|\Lambda(t))$ is well-approximated by Eq. (3.19) near $\omega = (1 - \frac{2\lambda}{n})\langle \omega \rangle$. In the large n limit, we require Gaussian $P(\omega|\Lambda(t))$ near values of ω which shift closer to the mean. For any sharply-peaked probability distribution, we can choose a value of n which is sufficiently large that the small deviations about $\langle \omega \rangle_\Lambda$ appear Gaussian, but we are not guaranteed that the variance is simply related to the mean by $2\langle \omega \rangle_\Lambda = \langle \delta\omega^2 \rangle_\Lambda$ except in the case of time-symmetric or linear-responding protocols.

3.6 Low-dissipation Ising Inversions

Using the protocol sampling framework, we can efficiently interrogate the interplay between dissipation and control of a non-equilibrium transformation. As a concrete example, we consider inverting a lattice of Ising spins from a state with all spins pointing up to a state with all spins pointing down by controlling a time-dependent temperature, $T(t)$, and magnetic field, $h(t)$. This scenario could be pertinent, e.g., to bit erasure when memory is stored as the state of a magnetic domain. If we carry out the spin flip infinitely slowly, we can induce a flip reversibly with no dissipation, but how much energy must be dissipated to cause the spin inversion in finite time? What is the form of $T(t)$ and $h(t)$ that minimizes dissipation, and how sensitive is the dissipation to deviations from optimal protocols?

To address these questions, it is customary to seek the optimal, minimum-dissipation protocol. Such optimal protocols have been computed for single-particle control problems. For example, we can steer a Brownian particle in a harmonic well by adjusting, as functions of time, either the center or the stiffness of the well. In both the overdamped [100] and underdamped [57] cases, Euler-Lagrange equations can be analytically solved to obtain the optimal protocols. If we simultaneously tune the well stiffness and the temperature of the particle's environment, it is also possible to analytically solve for the minimum dissipation paths as geodesics of an inverse diffusion tensor in a linear-response framework [124]. Brownian particles in anharmonic potentials are not easy to handle analytically, but the problems can be addressed numerically. Interestingly, one such numerical study has shown that there can be protocols, which differ significantly from the optimal protocol, but which have nearly identical dissipation [111]. This observation suggests that it could be fruitful to not only compute the optimal protocols but to also investigate fluctuations around the optimal protocols.

We present this complementary approach, focusing on the collection of protocols which have very low, though not exactly optimal, dissipation. As in the previous section, we can sample a distribution biased by dissipation as well as by h_A and h_B ,

$$P[\sigma(t), \Lambda(t)] \propto h_A(\sigma_0)h_B(\sigma_{t_{\text{obs}}})P_0[\sigma(t)|\Lambda(t)]e^{-\lambda\omega[\sigma(t), \Lambda(t)]}. \quad (3.24)$$

$P_0[\sigma(t)|\Lambda(t)]$ is the probability of generating a trajectory of spins, $\sigma(t)$, using the protocol $\Lambda(t) \equiv \{T(t), h(t)\}$. The time-evolution of the two-dimensional, Ising magnet is carried out with the push up/push down Ising dynamics, introduced in Chapter 2, and implemented as described in Appendix D. Ferromagnetic nearest-neighbor coupling is set to unity, and periodic boundary conditions are employed. The constraints, h_A and h_B , select out those trajectories which start with all spins aligned upward and end with them all aligned downward after t_{obs} sweeps; this notation is not to be confused with the external magnetic field, $h(t)$. An effect similar to the action of h_A and h_B is achieved if constraints are imposed on the protocols rather than the initial and final configurations of the spins. In this scheme, we sample the set of protocols which start at low temperature with a positive magnetic field and end at low temperature with a negated field. In effect, the constraint on the protocols

imposes the h_A and h_B constraints on the trajectories. The sampled joint distribution with protocol constraints can be written as

$$P_\lambda[\sigma(t), \Lambda(t)] \propto \delta(\Lambda_0 - \Lambda_A)\delta(\Lambda_{t_{\text{obs}}} - \Lambda_B)P_0[\sigma(t)|\Lambda(t)]e^{-\lambda\omega[\sigma(t), \Lambda(t)]}, \quad (3.25)$$

where Λ_A and Λ_B are the enforced initial and final values of the protocol. The extension to the case of n Ising trajectories is straightforward, following Eq. (3.22),

$$P_{n,\lambda}[\{\sigma(t)\}_{i=1}^n, \Lambda(t)] \propto \delta(\Lambda_0 - \Lambda_A)\delta(\Lambda_{t_{\text{obs}}} - \Lambda_B)\prod_i P_0[\sigma_i(t)|\Lambda(t)]e^{-\frac{\lambda}{n}\omega[\sigma_i(t), \Lambda(t)]}. \quad (3.26)$$

This extended ensemble can be sampled using Monte Carlo methods, which are detailed in Appendix D. Briefly, the trajectories are sampled using noise-guided shooting-like TPS moves forward and backward in time. The protocols are discretized and are defined by their value at ten evenly spaced times, $(\Lambda_0, \Lambda_{t_{\text{obs}}/10}, \Lambda_{2t_{\text{obs}}/10}, \dots, \Lambda_{t_{\text{obs}}})$. For times $it_{\text{obs}}/10 < t < (i+1)t_{\text{obs}}/10$, the temperature and magnetic field are ramped linearly between their values at time $it_{\text{obs}}/10$ and $(i+1)t_{\text{obs}}/10$. Protocols are sampled with MC moves that perturb the value of one of the eight interior points in the (T, h) plane defining the discretized protocol. In practice it is not desirable to consider protocols which utilize arbitrarily high temperatures or fields, so we also constrain the protocols to remain in a bounded region which we take to be the experimentally-accessible protocols⁸. As in low-temperature sampling of rugged potential energy surfaces, the high- λ sampling could explore the protocol space slowly. We employ standard replica exchange, swapping between replicas simulated with different values of λ but the same value of n , to alleviate this problem [46].

Figs. 3.8 and 3.9 show the result of protocol sampling for $n = 1$ and $n = 10$, respectively. Sampling with $\lambda = 0$ does not bias the protocols ($\gamma = 0$), so the protocols sample the “experimentally-accessible” protocols uniformly subject to the constraints on the initial and final points of the protocol. Fig. 3.8 shows that protocols are also sampled uniformly when $n = 1$ and $\lambda = 1$, a consequence of γ vanishing under those conditions. If λ and n are chosen such that $\gamma > 0$, the protocols are biased toward low values of $\langle\omega\rangle_\Lambda$. With large n and large λ , the protocols tend toward the optimal protocol. When the protocols fluctuate in a basin around the optimal protocol, averaging over protocol fluctuations yields a protocol which is similar to the optimal protocol, and which would exactly equal the optimal protocol in the $\gamma \rightarrow \infty$ limit. This average, plotted as a black line in Figs. 3.8 and 3.9, shows that the low dissipation protocols first heat the spins above the critical temperature, T_c , then tune the external field to negative values, and finally cool the spins. For finite γ , the average protocol is influenced by the manner in which we limit protocols to those which are “experimentally accessible.” An analogy with statistical mechanics is instructive, with Λ playing the part of a molecular configuration, $\langle\omega\rangle_\Lambda$ an energy function, and γ the inverse temperature. The typical molecular configurations are influenced by both energetic and entropic considerations. At low enough temperature, entropy is less important than energy,

⁸This means we sample a protocol distribution with a prior that is uniform over the experimentally-accessible protocols, but zero for all inaccessible protocols.

so the typical configurations are very similar to the minimum energy states. The manner in which we limit the experimentally-accessible protocol space affects the protocol entropy, but at high γ , the sampling of protocols is dominated by energetics (that is to say by $\langle \omega \rangle_\Lambda$).

If the average of the sampled protocols teaches us how to minimize dissipation, then what do we learn from the fluctuations about this average? These fluctuations teach us about how susceptible the dissipation is to changes in the protocol. The magnitude of the protocol fluctuations varies at different stages of the protocol, e.g., fluctuations in the value of h at time $t_{\text{obs}}/10$ are much greater than at time $t_{\text{obs}}/2$, indicating that to mitigate dissipation we require stricter control over the protocol at some times than at others. The source of the large h fluctuations early in the protocol can be understood by inspecting the protocols which cross the first-order phase transition line running along $h = 0$ from $T = 0$ to T_c . While the typical low-dissipation protocol avoids this line, some protocols cross it if γ is modest ($\lambda = 0.5, n = 1, \gamma = 0.25$, for example). Without exception, these protocols then re-cross the phase transition line while the protocol is still at a temperature below the critical temperature. Physically, these protocols involve flipping the magnetic field to point downward while the spins are still pointed up. As long as the temperature remains below T_c , it takes some time to nucleate a spin inversion. If h is tuned to positive values again before that nucleation, then the process is not dissipative—whatever work went into first crossing the phase transition line is recovered upon re-crossing.

These protocols that cross the phase transition line have low dissipation because the protocol is carried out in finite time. If the same protocols were performed more slowly, a spin inversion would have time to nucleate, and the procedure would be very dissipative. By acting on a small system in finite time, we manage to keep the the system far from equilibrium while h is temporarily negative. Does the Gaussian dissipation approximation, made in Eq. (3.20), break down for these far-from-equilibrium protocols? To address this question, two protocols were selected from the $n = 1, \lambda = 0.5$ ensemble, one of which crossed the phase-transition line, and the dissipation distribution of each protocol was computed with umbrella sampling. Fig. 3.10 shows that both dissipation distributions are profoundly non-Gaussian, in contrast to our linear response assumption. The assumption allowed us to estimate the mean $\langle \omega \rangle_\Lambda$ from the small- ω tails of $P(\omega|\Lambda)$, e.g., relating the mean dissipation to the behavior of $P(\omega|\Lambda)$ near $\omega = 0$ when $n = 1, \lambda = 0.5$ ⁹. The dashed lines, superimposed on the dissipation distributions in Fig. 3.10, show the estimated Gaussian form, assuming the linear response restriction $2\langle \omega \rangle_\Lambda = \langle \delta\omega^2 \rangle_\Lambda$, and fit to the small- ω branch of the distribution. Remarkably, this Gaussian form recovers the location of the dissipation distribution's peak, but this most likely value of ω does not equal the mean due to the fat tail at large values of dissipation. Based on these anecdotes, we anticipate that even when the dissipation distribution is not Gaussian, the linear response treatment could be practically useful. The ensemble sampled in Eq. (3.26) is equivalent to the ensemble that would be sampled if Eq. (3.17) were used to approximately sample the distribution in Eq. (3.16). Thus the

⁹The integral in Eq. (3.20), $\int d\omega e^{-(\omega - \langle \omega \rangle_\Lambda)^2/(4\langle \omega \rangle_\Lambda)} e^{-\lambda\omega}$, is dominated by the behavior of $P(\omega|\Lambda)$ around $\omega = 0$, so the estimate for $\langle \omega \rangle_\Lambda$ depends almost entirely on the trajectories with $\omega \approx 0$.

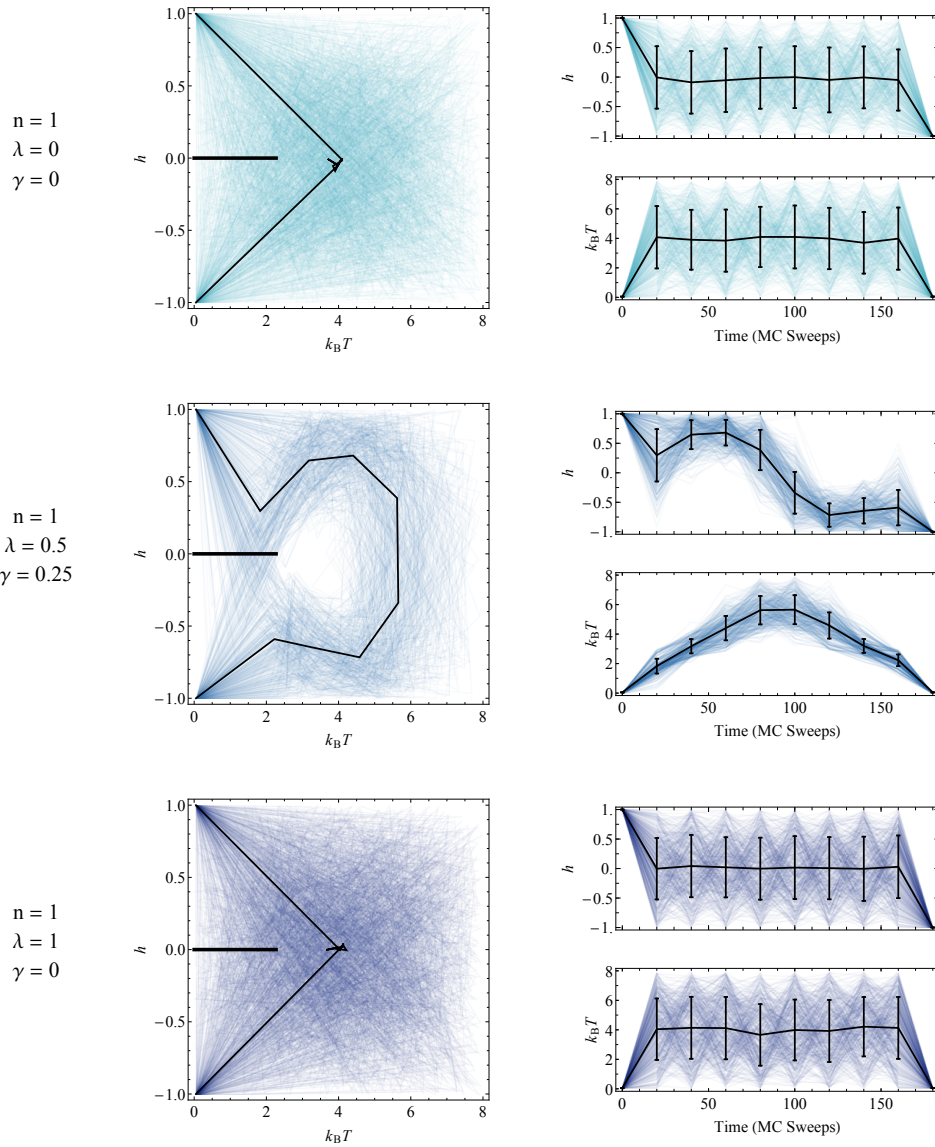


Figure 3.8: Protocols sampled from the joint distribution, $P_\lambda[\sigma(t), \Lambda(t)]$. Monte Carlo updates to the protocol are evaluated based on the dissipation of a single Ising trajectory, biased by λ to have low dissipation. When the effective bias acting on the average dissipation, γ , is positive, low-dissipation protocols are sampled. Data are shown for a 40×40 two-dimensional Ising lattice with periodic boundary conditions and nearest-neighbor coupling strength set to unity. Protocols start and end with $T = 0.05$ and $h = \pm 1$. Ising dynamics was performed as described in Appendix D with $\epsilon_{\text{acc}} = \epsilon_{\text{site}} = 0.001$. Replicas were simulated for $\lambda = 0, 0.1, \dots, 0.9, 1$, and replica exchange moves were attempted every 100 TPS steps. The plots show 450 protocols, sampled every 1000 TPS steps after an equilibration period of 50,000 TPS moves. The mean of the samples is shown in black, with error bars serving to highlight the standard deviation of this distribution, not the sampling errors.

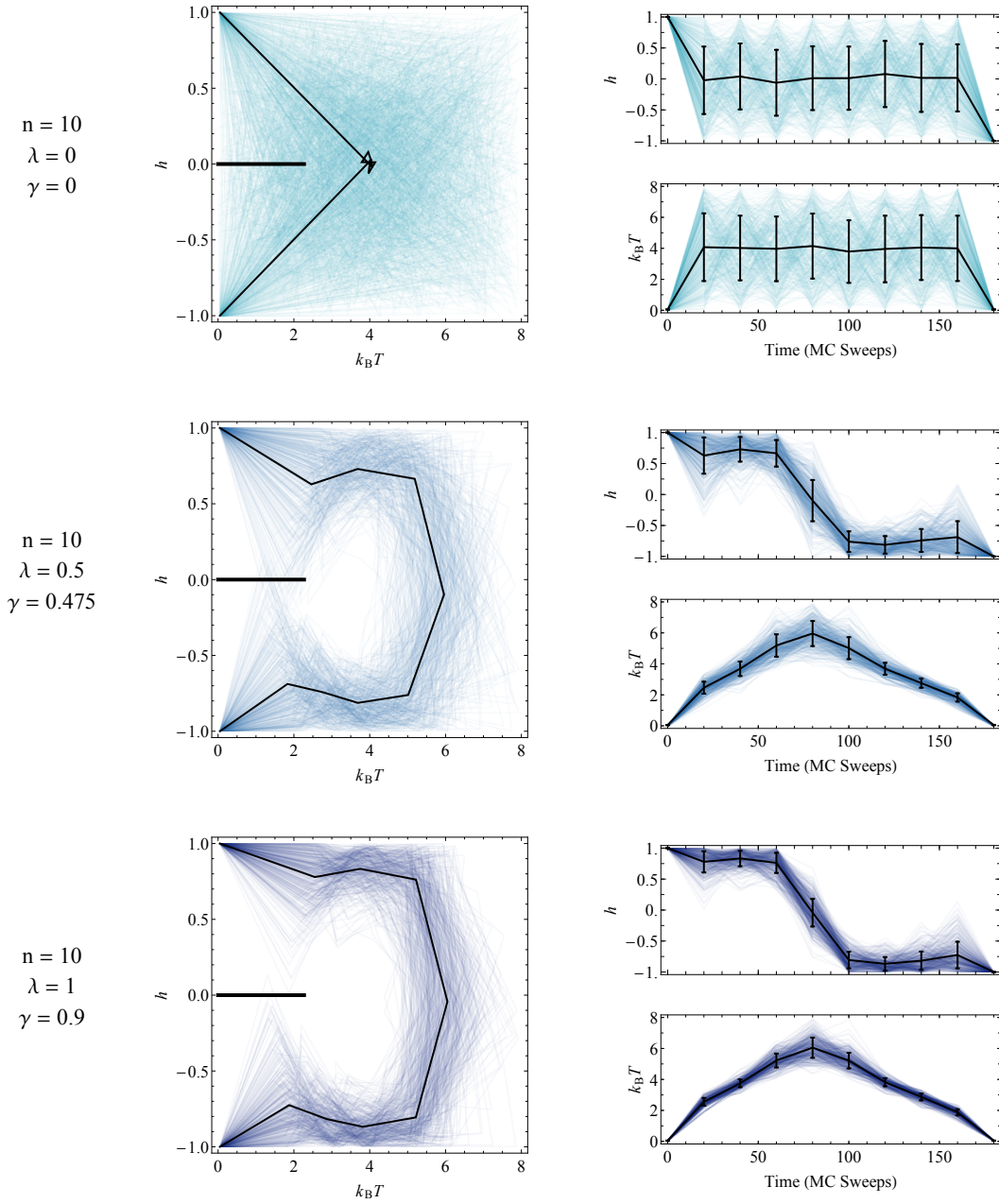


Figure 3.9: Protocols sampled from the joint distribution, $P_{n,\lambda}[\{\sigma(t)\}_{i=1}^n, \Lambda(t)]$. Monte Carlo updates to the protocol are evaluated based on the sample mean of $n = 10$ Ising trajectories, each of which is biased by λ/n to have low dissipation. All sampling parameters are the same as Fig. 3.8.

large n limit must be well-behaved. Future work is necessary to understand the relationship between this limiting behavior and the Gaussian linear response approximations.

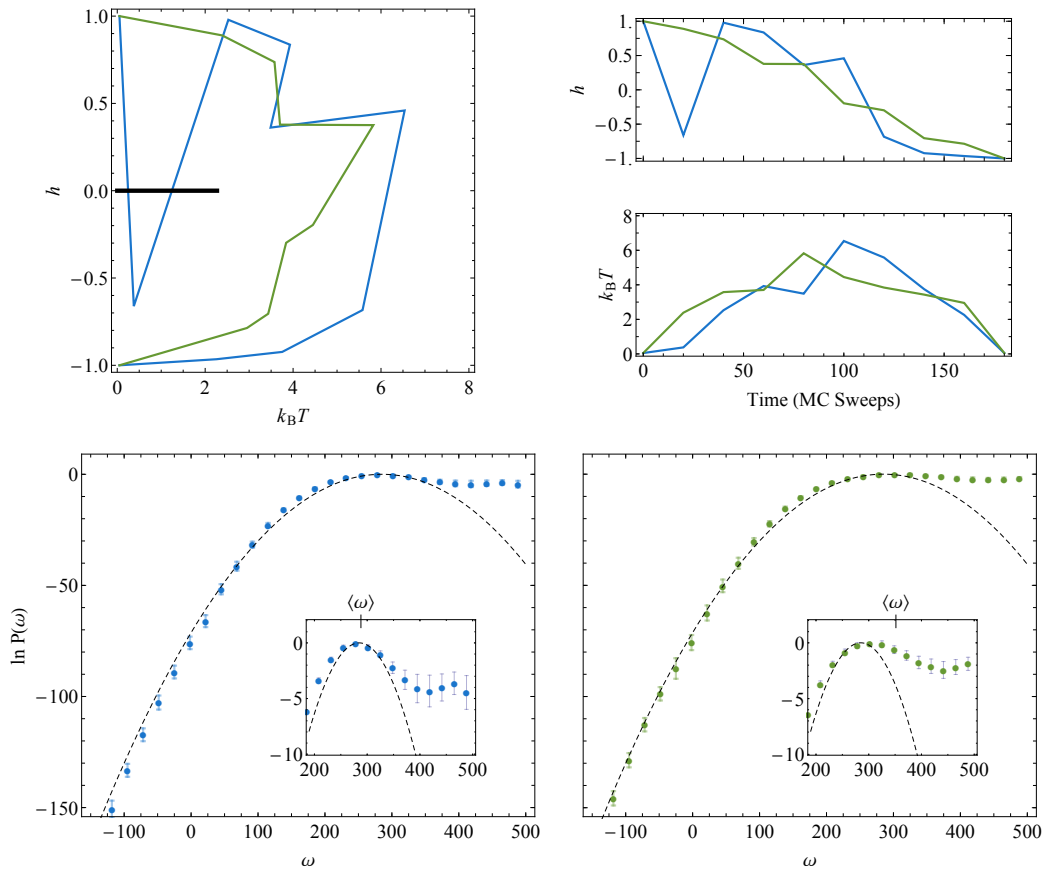


Figure 3.10: Two representative protocols selected from those sampled by the $n = 1, \lambda = 0.5$ ensemble, one of which transiently crosses the Ising model's first order phase transition line. The dissipation distribution (using a 200 sweep observation time) for both protocols is profoundly non-Gaussian, with a fat tail at large values of dissipation. Inset figures are zoomed in around the peak of the distribution. Dissipation distributions were collected using noise-guided TPS moves with a fixed protocol. Umbrella sampling was employed with exchange between replicas sampling $P_\lambda[\sigma(t), \Lambda_{\text{fixed}}]$ with $\lambda = 0, 0.05, 0.1, \dots, 1$.

Chapter 4

Large Deviation Methods for Markov Processes

4.1 Introduction

The preceding chapters discussed simulation methodology designed to investigate rare trajectories in Markov processes. We had in mind Markov processes evolving chaotically in high-dimensional spaces. Under such conditions, exactly-solvable problems are scarce, so our focus was on computational sampling. Analytical methods should not be completely discarded, however. Path sampling is computationally expensive, so it is worthwhile to develop complementary analytical tools and solvable toy models to guide intuition and validate methods. The final chapter of this thesis introduces a set of non-equilibrium Markov models for which the rare trajectories can be characterized analytically by the methods of large deviation theory. Because that analytical work utilizes large deviation methods, this chapter reviews necessary background material ¹.

Drawing heavily from Hugo Touchette's review [112], this chapter surveys elementary large deviation methods and their application to trajectory spaces. We introduce the rate function, or large deviation function (LDF), and discuss its connection to the scaled cumulant generating function (SCGF) via the Legendre transform. Particular attention is given to the case that the SCGF possesses a cusp, which gives rise to a first order phase transition. These general tools can be applied to the thermodynamic limit of any system with many degrees of freedom, regardless of whether the degrees of freedom are in a physical configuration space or in trajectory space. We discuss the application to Markovian trajectories and the titled operators used to isolate rare trajectories. Finally, we demonstrate that an auxiliary dynamics, which highlights the rare trajectories, can be constructed.

¹This chapter is a review of prior work in the field. It is included to make the thesis more self-contained. The next chapter contains novel work.

4.2 What is a Rate Function?

A central object of large deviation theory is the *large deviation rate function*, which quantifies the probability of fluctuations away from the most likely value of an observable. Free energies are examples of rate functions, but the concept is more general than the typical use in equilibrium statistical mechanics. As an example, imagine recording the value of a random observable many times. The law of large numbers states that the mean of the recorded values will converge to the expectation value of the observable. The rate function teaches us about the rate of convergence to this expectation value. More precisely, we can study the probability distribution for the sample mean after N observations. For finite N , this probability distribution will have a finite width, but in the $N \rightarrow \infty$ limit the law of large numbers says that the distribution should narrow to a delta function positioned at the expectation value. The rate of this narrowing with increasing N is described by a rate function.

As an illustrative example, consider the familiar problem of a sequence of N coin flips. The sample mean of these flips is an intensive quantity and can be written as

$$x = \frac{1}{N} \sum_{i=1}^N \sigma_i, \quad (4.1)$$

where σ_i takes the value 1 or 0 for an up or down flip, respectively. The probability of observing a given value of x is of course given by the binomial distribution

$$P(x) = \frac{1}{2^N} \frac{N!}{(xN)!((1-x)N)!}. \quad (4.2)$$

When N is large, this exact form of the probability is not necessarily the most useful form because the factorials become cumbersome. We are sometimes better off dealing with an asymptotic form of this probability. In the case of this example, the asymptotic form is simple to derive by Stirling's approximation. The result is

$$P(x) \approx e^{-NI(x)}, \text{ with } I(x) = \ln 2 + x \ln x + (1-x) \ln(1-x), \quad (4.3)$$

and the function $I(x)$ is called the rate function. In the $N \rightarrow \infty$ limit only the values $x = x^*$ which minimize $I(x)$ retain nonzero probability, but for finite N , the rate function relates the probability of observing sample mean x to the deviation of $I(x)$ from $I(x^*)$. In other words, the rate function provides information about the fluctuations away from the expectation value. For example, a harmonic rate function corresponds to Gaussian statistics. When N is very large, deviations from x^* are increasingly unlikely, which is why the rate function is also commonly known as a large deviation function —the function describes the probability of large deviations from the mean.

These manipulations for the trivial coin flip problem are not especially deep; the result was already known by Stirling's approximation. We have simply extracted the intensive part

of the exponent,

$$I(x) = - \lim_{N \rightarrow \infty} \frac{1}{N} \ln P(x), \quad (4.4)$$

and given it a special name. To understand the usefulness of this procedure, we must advance to problems for which the asymptotic form of the probability distribution would not be known by other means. We will see that one can compute the rate function from a scaled cumulant generating function for x , thereby providing an alternate route to the asymptotic form of the probability distribution for x .

4.3 Scaled Cumulant Generating Functions and Legendre Transforms

Let us introduce the scaled cumulant generating function, whose derivatives yield the cumulants of the random variable x ,

$$\psi(k) = \lim_{N \rightarrow \infty} \frac{1}{N} \ln \langle e^{kN x} \rangle, \quad (4.5)$$

where $\langle e^{kN x} \rangle = \int e^{kN x} P(x) dx$. Assuming that the asymptotic form of $P(x)$ can be described by the rate function, the exponential average can be expressed in terms of $I(x)$.

$$\psi(k) = \lim_{N \rightarrow \infty} \frac{1}{N} \ln \int e^{N(kx - I(x))} dx. \quad (4.6)$$

Because we are interested in the large N limit, the integrand is sharply peaked and the integral can be approximated by Laplace's method as being roughly equal to the magnitude of the maximal value of the integrand. This maximal value occurs when $kx - I(x)$ is maximized, therefore

$$\psi(k) = \lim_{N \rightarrow \infty} \frac{1}{N} \ln \langle e^{N k x} \rangle \approx \sup_x (kx - I(x)). \quad (4.7)$$

In sufficiently large systems the approximation by Laplace's method is so good that this last relation can be considered an equality. In other words, Eq. (4.7) relates $\psi(k)$ and $I(x)$ by a Legendre-Fenchel transformation. For our purposes, we will neglect technical details and just treat $\psi(k)$ and $I(x)$ as Legendre transforms rather than the generalized Legendre-Fenchel transform. Readers interested in more technical details are directed to [112].

The Legendre transform relation between scaled cumulant generating function $\psi(k)$ and rate function $I(x)$ is significant because Legendre transforms can be inverted. In fact the transform is its own inverse.

$$I(x) = \sup_k (kx - \psi(k)). \quad (4.8)$$

There is a slight danger in the mathematical sloppiness of this presentation. Namely, the computation of $I(x)$ as a Legendre transform of $\psi(k)$ requires that $\psi(k)$ be everywhere

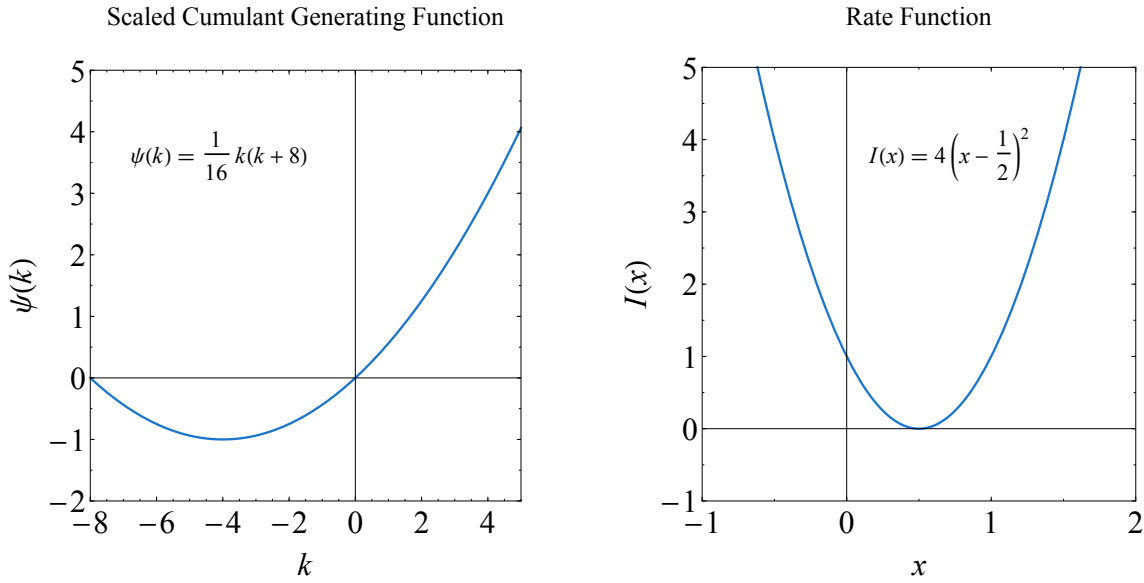


Figure 4.1: Graphical representation of the Legendre transform relationship between a scaled cumulant generating function and a rate function. Note that this rate function is quadratic and does not correspond to the coin flip example of the main text. At $k = 0$ the slope of $\psi(k)$ is $1/2$ so that at $x = 1/2$ the slope of $I(x)$ is 0. Similarly, at $x = 0$ the slope of $I(x)$ is -4 and $\psi'(k) = 0$ at $k = -4$.

analytic. The coin flip calculation provides one example of a smooth SCGF,

$$\psi(k) = \frac{e^k \left(k - \ln \left(\frac{2e^k}{1+e^k} \right) \right) - \ln \left(\frac{2}{1+e^k} \right)}{1+e^k}. \quad (4.9)$$

Provided both $\psi(k)$ and $I(x)$ are analytic, recall the graphical connection between a function and its Legendre transform. The slope of $\psi(k)$ at k is the abscissa of $I(x)$ for which $I(x) = k$. Because the inverse is also a Legendre transform, the same relation relates slopes of $I(x)$ to $\psi(k)$. In Fig. 4.1 we graphically illustrate the relationship with a quadratic rate function ².

The situation is more complicated if $\psi(k)$ is not analytic. Suppose there is a cusp at k^* where the left and right derivatives, x_l and x_r respectively, are not equal. Using Jensen's inequality, it can be shown that $\psi(k)$ is convex. Therefore the existence of the cusp implies that $\psi'(k)$ never attains values between x_l and x_r . As a consequence, $\psi(k)$ contains no information about the value of $I(x)$ between x_l and x_r . Bridging this gap by a straight line is the familiar Maxwell construction from classical thermodynamics, and the slope of this line is k^* , the position of the cusp. A cusp in the scaled cumulant generating function must indicate a bistability in the rate function.

²We retain the notation of the coin flip problem, but the variable x should only be interpreted as the sample mean of coin flips when $I(x)$ takes the form of Eq. (4.3), which is, of course, not quadratic.

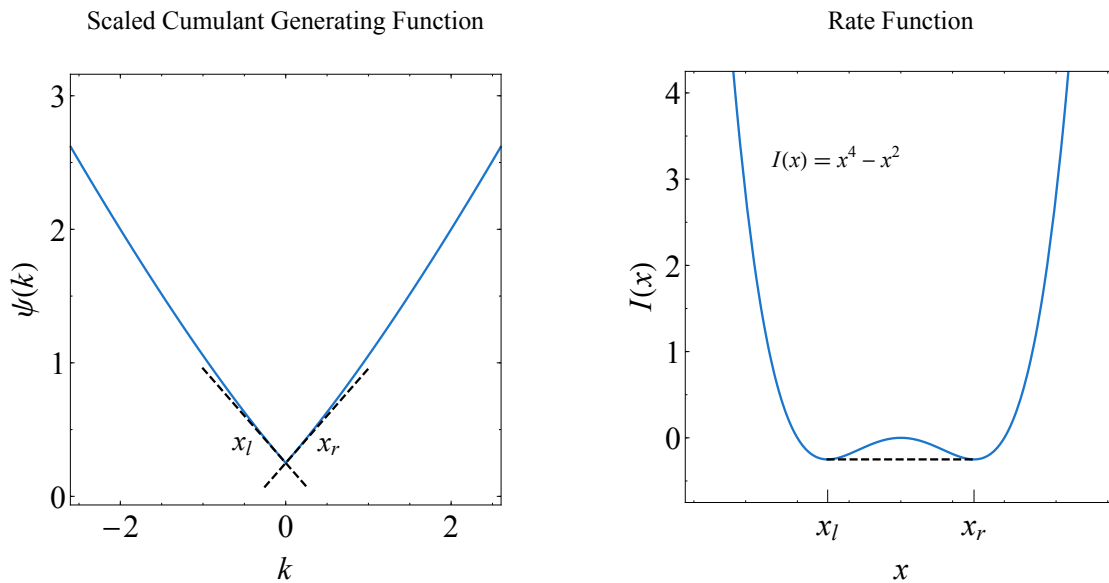


Figure 4.2: Graphical representation of the Legendre transform relationship for $\psi(k)$ and $I(x)$ when $\psi(k)$ has a cusp at $k = 0$. A Legendre transform of $\psi(k)$ gives no information about $I(x)$ between x_l and x_r , but the Legendre transform of $I(x)$ yields all of $\psi(k)$. In particular, the Legendre transform of the solid and dashed lines in the right figure yield the same $\psi(k)$. The presence of the cusp at $k = 0$ implies that the slope of $I(x)$ between x_l and x_r is zero, in other words the system is at co-existence.

In particular, if that cusp occurs at $k = 0$, the bistability corresponds to a first order phase transition at co-existence. This observation is shown graphically in Fig. 4.2. There are two equally likely values of x in the large N limit. Generally there are many microscopic states which are consistent with the same value of the macroscopic order parameter, x . For example, there are many coin flip sequences which share the same sample mean. When there are two equally likely values of x , it implies that there are two equally likely sets of microstates³. These sets are the thermodynamic phases, whose co-existence can be traced back to the SCGF singularity. In Chapter 5 we identify such a singularity in a trajectory space SCGF, which corresponds to a dynamic phase transition.

4.4 Continuous-time Markov Processes

The tools of large deviation theory are particularly useful for analyzing continuous-time Markov processes. For simplicity we consider trajectories which visit a countable number of possible configurations. Let the vector \mathbf{p} be a vector containing the probability of each

³Coin flips do not exhibit such a phase co-existence since $\psi(k)$ is analytic.

configuration. The time-dependence of \mathbf{p} is given by a master equation of the form

$$\frac{\partial \mathbf{p}}{\partial t} = \mathbb{W}\mathbf{p}. \quad (4.10)$$

The matrix \mathbb{W} is a rate matrix whose off-diagonal matrix element, \mathbb{W}_{ij} , is the rate for transitioning from configuration j to configuration i . To ensure conservation of probability, $\mathbb{W}_{ii} = -\sum_j \mathbb{W}_{ij}$ [70]. Formally, the time-evolution of probability is provided by a matrix exponential,

$$\mathbf{p}(t) = e^{\mathbb{W}t} \mathbf{p}(0). \quad (4.11)$$

In the long time limit, $\mathbf{p}(t)$ approaches a steady state distribution \mathbf{p}_{ss} which satisfies

$$\mathbf{p}_{ss} = e^{\mathbb{W}t} \mathbf{p}_{ss}. \quad (4.12)$$

Eq. (4.12) can be read as an eigenvalue relation, guaranteeing that zero is an eigenvalue of \mathbb{W} with right eigenvector \mathbf{p}_{ss} . The associated left eigenvector is a vector of ones.

Representative trajectories generated by rate matrix \mathbb{W} can be simulated in a straightforward way using the Gillespie algorithm [40, 54, 55]. This algorithm takes an initial configuration, often sampled from \mathbf{p}_{ss} , and propagates dynamics in discrete jumps. Suppose that the trajectory begins in state i at time 0. The probability that the next move hops to site j is $\mathbb{W}_{ji}/\sum_{k \neq i} \mathbb{W}_{ki}$, and the elapsed time before the next hop is chosen stochastically from an exponential distribution, whose expectation value is $-\mathbb{W}_{ii}^{-1}$. While hops occur discretely, time advances continuously.

Direct simulation of trajectories provides a way to determine statistical properties of the dynamics. To illustrate what is meant by “statistical properties of the dynamics,” let us start with an example. Consider dynamics around a cycle of three states as depicted in Fig. 4.3. Let us furthermore choose transition rates such that clockwise hops are faster than counterclockwise ones. Typical trajectories complete cycles, so such a Markov model underlies many representations of molecular motors [4, 73, 119, 120]. In the context of motors, it is physically interesting to quantify the net clockwise current, which could be related to the work performed by the motor. The clockwise and counterclockwise rates, k_{CW} and k_{CCW} determine the average current. There are, however, statistical fluctuations, so the current measured for a single trajectory will not generally equal the mean value. Deviations, potentially large deviations, teach us about the probability that the motor fails to function. The most straightforward way to compute such current fluctuations is to generate many trajectories with the Gillespie algorithm and construct the distribution of observed currents. Noise-guided path sampling, discussed in Chapter 2, provides a more sophisticated simulation approach. In the next section we introduce a third option, which bypasses the need for simulation altogether.

4.5 Distributions of Dynamic Order Parameters

To characterize the statistics of current, we can conceptually separate the trajectory space into disjoint sets of trajectories, each consisting of all trajectories which share a particu-

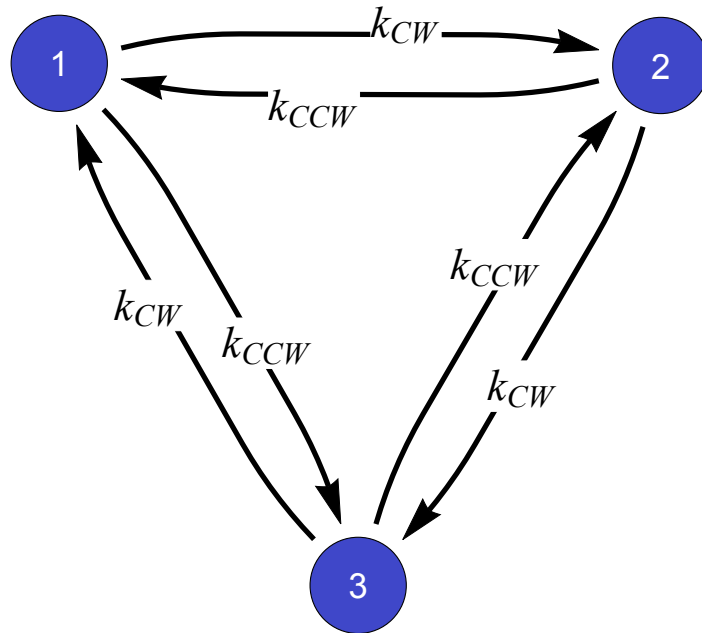


Figure 4.3: Transition rates for a cycle with three states. When $k_{\text{CW}} > k_{\text{CCW}}$ the transitions are necessarily out of equilibrium. Such rates can only be physically maintained by dissipating energy.

lar value of the current. This clustering of microstates (in this case trajectories) based on their value of a macrostate (the current) is, of course, the same thing we did in the coin flip example. There we averaged over all sequences consistent with the order parameter to obtain the probability of observing different fractions of heads. In the case of trajectories, we classify the dynamics using several different *dynamic order parameters*: time-integrated current [36], dynamical activity [64, 75], and entropy production [74, 86, 103]. Each dynamical order parameter highlights one particular aspect of the dynamics. Which order parameter to investigate depends on the physical problems to be solved. We have already given a motivation for when studying current statistics may be biophysically relevant. Dynamical activity, the total number of hops taken by a trajectory, is of interest to the onset of glassy dynamics. The entropy production, defined to be the logarithm of the ratio of the trajectory's forward and reversed probabilities, is interesting for its connection to the dissipation required to drive non-equilibrium processes. This final order parameter will be our primary focus for the remainder of the thesis.

We will discuss how to compute entropy production statistics, but first, let us briefly address the physical interest in the quantity by considering the entropy produced by dynamics

on the three state model of Fig. 4.3. In particular, setting the rates $k_{\text{CW}} > k_{\text{CCW}}$ breaks detailed balance and creates cycles. Such a set of rate constants cannot be maintained by an isolated physical system, which would thermalize to adopt a collection of rates obeying detailed balance. The average entropy production gives a bound on the energy which must be dissipated by other processes, external to the three-state model, in order to maintain the cycles. It remains an active area of research to understand what, if any, physical interpretation should be assigned to the entire distribution of entropy productions. At the very least, our analysis of entropy production distributions in Chapters 2 and 3 shows that the fluctuations away from the average are relevant to algorithmic development.

Formally, we seek the distribution of

$$\Omega[\mathbf{x}(t)] = \ln \frac{P[\mathbf{x}(t)]}{P[\hat{\mathbf{x}}(t)]}, \quad (4.13)$$

averaged over the set of all trajectories. Each trajectory, $\mathbf{x}(t)$, is a sequence of hops and waiting times, which occurs with probability $P[\mathbf{x}(t)]$. The time-reversal of the trajectory, which carries out the same hops in reversed order, is denoted $\hat{\mathbf{x}}(t)$. We index the hop number by α so we can write

$$P[\mathbf{x}(t)] \propto \rho_{\text{ss}}(\mathbf{x}_0) \prod_{\alpha=0} \mathbb{W}_{\mathbf{x}_{\alpha+1}, \mathbf{x}_\alpha} e^{-R_{x_\alpha}(t_{\alpha+1} - t_\alpha)}. \quad (4.14)$$

The (continuous) time of hop α is denoted t_α , and the state of the system at that time is \mathbf{x}_α . R_i is the sum of all rates exiting site i . Under the time-reversed dynamics, we denote the steady-state distribution $\hat{\rho}_{\text{ss}}$ and the sum of the rates for leaving site i as \hat{R}_i , so the probability of a time-reversed trajectory is

$$P[\hat{\mathbf{x}}(t)] \propto \hat{\rho}_{\text{ss}}(\mathbf{x}_{\text{final}}) \prod_{\alpha=0} \mathbb{W}_{\mathbf{x}_\alpha, \mathbf{x}_{\alpha+1}} e^{-\hat{R}_{x_{\alpha+1}}(t_\alpha - t_{\alpha+1})}, \quad (4.15)$$

where $\mathbf{x}_{\text{final}}$ is the state after the last hop of the forward trajectory. By comparing the path probabilities of forward and reversed trajectories, we find that a trajectory has entropy production

$$\Omega[\mathbf{x}(t)] = \ln \frac{\rho_{\text{ss}}(\mathbf{x}_0)}{\rho_{\text{ss}}(\mathbf{x}_f)} + \sum_{\alpha=0} \ln \frac{\mathbb{W}_{\mathbf{x}_{\alpha+1}, \mathbf{x}_\alpha}}{\mathbb{W}_{\mathbf{x}_\alpha, \mathbf{x}_{\alpha+1}}}, \quad (4.16)$$

where we have made use of the fact that $R_{\mathbf{x}_\alpha} = \hat{R}_{\mathbf{x}_{\alpha+1}}$. The second term of Eq. (4.16) grows extensively with the trajectory length, while the first term is a surface term—a contribution just from the initial and final times. We focus only on the time-additive part of the order parameter, which we rename ω ,

$$\omega[\mathbf{x}(t)] = \sum_{\alpha=0} \ln \frac{\mathbb{W}_{\mathbf{x}_{\alpha+1}, \mathbf{x}_\alpha}}{\mathbb{W}_{\mathbf{x}_\alpha, \mathbf{x}_{\alpha+1}}}. \quad (4.17)$$

In analogy with the discussion of coin flip large deviations, we compute the LDF for ω by first calculating the generating function,

$$\psi_\omega(\lambda) = \lim_{t_{\text{obs}} \rightarrow \infty} \frac{1}{t_{\text{obs}}} \ln \langle e^{-\lambda\omega} \rangle. \quad (4.18)$$

The bias introduced by λ serves to favor those trajectories with low entropy production. This generating function differs in sign convention from the true scaled cumulant generating function (SCGF), so odd cumulants are given by derivatives with respect to negative λ ⁴. While it is a minor misuse of language, we will refer to $\psi(k)$, defined as in Eq. (4.18) as the SCGF for entropy production, remembering that we would have to keep track of minus signs to obtain cumulants. Following the method of Lebowitz and Spohn [74], it is productive to define a vector $\mathbf{g}(t)$ whose i^{th} component is given by the conditional average

$$g_i(t) \equiv \langle e^{-\lambda\omega} | \text{in state } i \text{ at time } 0 \rangle. \quad (4.19)$$

The expectation value is an average over all trajectories from time 0 to time t . To convert $\mathbf{g}(t)$ into the SCGF we need only sum over all possible initial states, i .

$$\psi_\omega(\lambda) = \lim_{t_{\text{obs}} \rightarrow \infty} \frac{1}{t_{\text{obs}}} \ln \sum_i g_i(t). \quad (4.20)$$

We can further simplify this expression if we determine the long-time behavior of $\mathbf{g}(t)$. To do so we consider how $\mathbf{g}(t)$ changes as the trajectory is made infinitesimally longer by adding time to the beginning of the trajectory. The additional sliver of time could involve a hop from some other state j to i , or it could just involve the trajectory staying in site i for a little longer. In the event of a hop, the additional contribution to the measurement of $e^{-\lambda\omega}$ can be expressed in terms of the entropy produced by a hop from site j to i , $\omega_{ij} \equiv \ln \mathbb{W}_{ij} - \ln \mathbb{W}_{ji}$. In equations, we have

$$\begin{aligned} \frac{d}{dt} g_i(t) &= \left(\sum_{j \neq i} \mathbb{W}_{ij} e^{-\lambda\omega_{ij}} g_j(t) \right) + R_i g_i(t) \\ &= \sum_{j \neq i} (\mathbb{W}_{ij}^{1-\lambda} \mathbb{W}_{ji}^\lambda g_j(t) - \mathbb{W}_{ji} g_i(t)) \\ &= \sum_j \mathbb{W}_{ij}^{1-\lambda} \mathbb{W}_{ji}^\lambda g_j(t) \\ &= \sum_j \mathbb{W}_\omega(\lambda)_{ij} g_j(t). \end{aligned} \quad (4.21)$$

⁴Our sign convention, with the negative sign in the exponent, amounts to a reflection of the true scaled cumulant generating function about $\lambda = 0$. We have adopted this sign convention to be consistent with the already-published work presented in Chapter 5 and the conventions of the s -ensemble work [49]. The rationale for working with the minus sign in the definition for $\psi(\lambda)$ is that a Legendre transform of $\psi(\lambda)$, thus defined, directly yields a log-probability for x . The Legendre transform of the SCGF (with the positive sign in the definition) yields an effective potential for x , which could be negated to get the log-probability. Whatever the sign convention, the mathematics is, of course, equivalent.

The last line defines a tilted operator $\mathbb{W}_\omega(\lambda)$. Recall that the matrix exponential of \mathbb{W} propagates the vector of probabilities, $\mathbf{p}(t)$. The equation of motion for $\mathbf{g}(t)$ takes the same algebraic form,

$$\mathbf{g}(t) = e^{\mathbb{W}_\omega(\lambda)t} \mathbf{g}(0). \quad (4.22)$$

Let us denote the maximum eigenvalue of $\mathbb{W}_\omega(\lambda)$ by $\nu(\lambda)$ with the associated right eigenvector $|r(\lambda)\rangle$. If we abbreviate the vector of ones by $\langle 1|$ then Eq. (4.20) can be written as

$$\psi_\omega(\lambda) = \lim_{t_{\text{obs}} \rightarrow \infty} \frac{1}{t_{\text{obs}}} \ln \langle 1| e^{\mathbb{W}_\omega(\lambda)t_{\text{obs}}} |\mathbf{g}\rangle = \lim_{t_{\text{obs}} \rightarrow \infty} \frac{1}{t_{\text{obs}}} \ln (\langle 1| r(\lambda)\rangle e^{\nu(\lambda)t_{\text{obs}}}) = \nu(\lambda). \quad (4.23)$$

Since the long-time behavior of the tilted operator is dominated by the largest eigenvalue, we see that $\psi_\omega(\lambda)$ is given by this maximum eigenvalue.

The SCGF, $\psi_\omega(\lambda)$, is converted to a LDF for the entropy production by a Legendre-Fenchel transform as discussed in Section 4.3. In the long time limit, the fluctuating entropy production rate, $\sigma \equiv \omega/t_{\text{obs}}$ satisfies the large deviation form

$$P(\sigma) \sim e^{-t_{\text{obs}}I(\sigma)}. \quad (4.24)$$

The rate function $I(\sigma)$ exhibits bistabilities associated with a first order dynamic phase transition if and only if $\psi_\omega(\lambda)$ possesses a cusp. Since we have expressed $\psi_\omega(\lambda)$ as a maximum eigenvalue of a matrix, it follows that $\psi_\omega(\lambda)$ must change smoothly as a function of λ unless the matrix becomes infinitely large. In the next chapter we will explore that condition in a few models, showing simple conditions for a dynamic phase transition. While the SCGF cannot rigorously have singularities for finite state spaces, we will numerically demonstrate that the mathematical framework remains useful for large but finite state spaces.

4.6 Lebowitz-Spohn Symmetry and the Entropy Production Fluctuation Theorem

The entropy production fluctuation theorem is a straightforward corollary of the preceding analysis. Lebowitz and Spohn noted that replacing λ by $1 - \lambda$ serves to transpose the tilted operator [74]. A matrix and its transpose share an eigenspectrum and thus have the same maximal eigenvalue. Consequently, $\psi_\omega(\lambda) = \psi_\omega(1 - \lambda)$, or equivalently $\psi_\omega(\lambda)$ is symmetrical about $\lambda = 1/2$. The symmetry in the SCGF has implications on the LDF because I and ψ_ω are related by Legendre transform⁵

$$I(\sigma) = \sup_{\lambda} [-\lambda\sigma - \psi_\omega(\lambda)]. \quad (4.25)$$

If we use Lebowitz and Spohn's symmetry of $\psi_\omega(\lambda)$, we can rewrite Eq. (4.25) as

$$I(\sigma) = -\sigma + \sup_{1-\lambda} [(1 - \lambda)\sigma - \psi_\omega(1 - \lambda)]. \quad (4.26)$$

⁵The Legendre transforms are slightly different from Eq. (4.5). Because I flipped the sign on λ in Eq. (4.18), the minus sign must carry through to the relationship between $\psi_\omega(\lambda)$ and $I(\sigma)$.

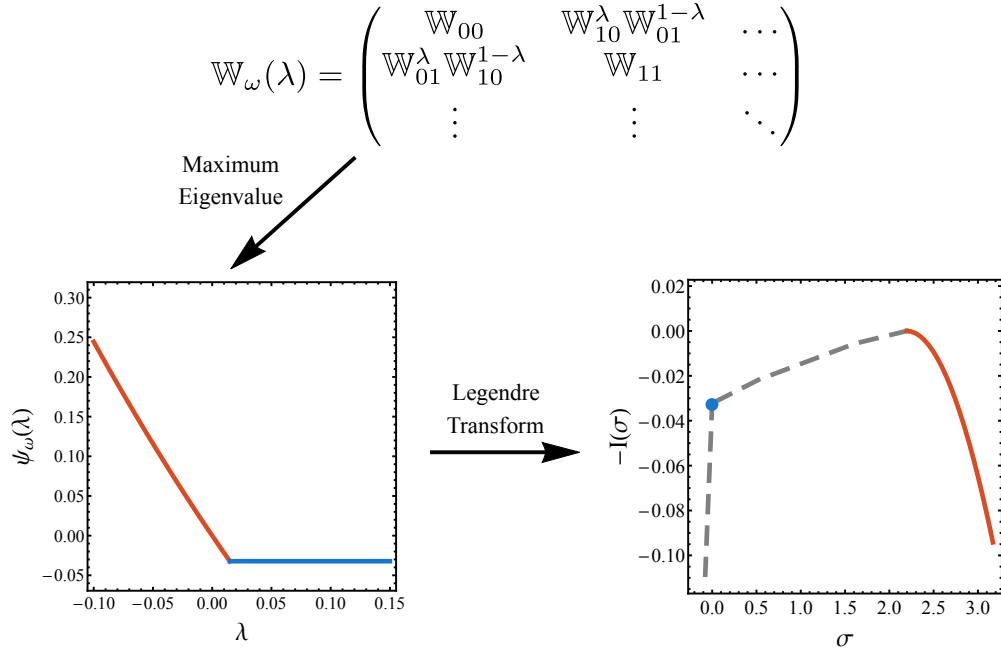


Figure 4.4: Illustration of the connection between the tilted operator, SCGF, and LDF for entropy production fluctuations. A cusp in the SCGF, $\psi_\omega(\lambda)$, causes a linear region of the LDF, which results in large dynamical fluctuations (relative to, for example, a Gaussian distribution). The plotted SCGF and LDF, from the “ring network” of Chapter 5, The slope of the dashed lines in the LDF correspond to the λ value of the SCGF cusps.

Now note that $1 - \lambda$ appears as a dummy variable so the second term can be related to the entropy production rate function,

$$\sup_{1-\lambda} [(1 - \lambda)\sigma - \psi_\omega(1 - \lambda)] = \sup_\lambda [\lambda\sigma - \psi_\omega(\lambda)] = I(-\sigma). \quad (4.27)$$

After plugging this relation into Eq. (4.26), we are left with $I(\sigma) = I(-\sigma) - \sigma$. If we work with the probability distributions rather than the rate functions, we have

$$\frac{P(\omega)}{P(-\omega)} \sim e^{-t_{\text{obs}}(I(\sigma) - I(-\sigma))} = e^{t_{\text{obs}}\sigma} = e^\omega. \quad (4.28)$$

Hence the symmetry of $\psi_\omega(\lambda)$ about $\lambda = 1/2$ is equivalent to a statement of the (asymptotic) entropy production fluctuation theorem.

4.7 Conditioned Dynamics

Suppose we are not content knowing the probability of rare entropy production fluctuations, as provided by the LDF. We might also want to know what the trajectories looked like which yielded the large entropy production fluctuations. We could answer the question by brute force, generating ordinary dynamics with the Gillespie algorithm, which produces trajectory $\mathbf{x}(t)$ with probability

$$P_0[\mathbf{x}(t)] \propto \rho_{ss}(\mathbf{x}_0) \prod_{\alpha=0} \mathbb{W}_{\mathbf{x}_{\alpha+1}, \mathbf{x}_\alpha} e^{-R_{x_\alpha}(t_{\alpha+1} - t_\alpha)}. \quad (4.29)$$

This is the exact same expression as Eq. (4.14), but we have now put a subscript 0 on the path probability as in Eq. (2.5) to indicate the natural dynamics. After collecting enough samples, we would find some trajectories which exhibited the rare behavior, and we could focus our analysis on this subensemble. Of course, this straightforward approach is immensely inefficient if the studied entropy production fluctuations are very rare.

To highlight the trajectories with low entropy production, we can alternatively study trajectories from a tilted ensemble,

$$P_{\text{tilted}}[\mathbf{x}(t), \lambda] \propto P_0[\mathbf{x}(t)] e^{-\lambda \omega[\mathbf{x}(t)]}. \quad (4.30)$$

When λ is large, trajectories from this ensemble give insight into the small- ω wings of the natural dynamics' entropy production distribution. We could sample the tilted ensemble using path sampling methods as in Section 3.6. Trajectories could be generated according to $P_0[\mathbf{x}(t)]$ using the unbiased Gillespie dynamics, then conditionally accepted so as to sample $P_{\text{tilted}}[\mathbf{x}(t), \lambda]$. As discussed in Chapter 2, trajectories grown using natural dynamics differ from tilted ensemble trajectories in a manner that grows extensively with the trajectory length, so path sampling will falter for long trajectories.

Here, we demonstrate that it is possible to define an auxiliary dynamics, whose trajectories differ from those of the tilted ensemble in a sub-extensive manner. This auxiliary dynamics is the effective dynamics which mimics the natural dynamics, conditioned upon a biased entropy production. This conditioning, known as Doob's h -transform, has been recently popularized in the physics literature by Rob Jack, Hugo Touchette, and Raphaël Chetrite [27, 28, 68]. Here we spell out the main result in simpler, but less general, terms than has been previously discussed.

In the Section 4.5, we showed that the largest eigenvalue of $\mathbb{W}_\omega(\lambda)$ teaches us about the probability of finding trajectories which produce rare amounts of entropy. Furthermore, the exponential of the tilted operator acted as the propagator in an equation of motion. Can $\mathbb{W}_\omega(\lambda)$ be interpreted as the rate matrix that generates the trajectories which accentuate the rare values of entropy production? The answer is no, but the intuition is nearly correct. The problem is that the tilted operator is not generally a rate matrix, that is the columns sum to zero only when $\lambda = 0$ or 1 . Consequently, when the time-propagator $e^{\mathbb{W}_\omega(\lambda)t}$ acts on a normalized initial distribution, it does not yield a normalized distribution. By accounting for

the failure to conserve probability, it is possible to relate the tilted operator to an effective dynamics, conditioned to favor rare values of entropy production. Specifically, let us consider an auxiliary dynamics with a λ -dependent rate matrix, $\mathcal{W}(\lambda)$ whose matrix elements $\mathcal{W}(\lambda)_{ij}$ are given by

$$\langle i|\mathcal{W}(\lambda)|j\rangle = \frac{\langle\ell(\lambda)|i\rangle}{\langle\ell(\lambda)|j\rangle} \langle i|\mathbb{W}_\omega(\lambda)|j\rangle - \langle i|j\rangle \psi_\omega(\lambda), \quad (4.31)$$

where I have temporarily switched to Dirac notation to avoid a plethora of subscripts. The bra $\langle\ell(\lambda)|$ is the left eigenvector of the tilted operator which corresponds to maximal eigenvalue $\psi_\omega(\lambda)$. It is straightforward to confirm that \mathcal{W} is a rate matrix by summing over the first index.

$$\begin{aligned} \sum_i \mathcal{W}(\lambda)_{ij} &= \sum_i \frac{\langle\ell(\lambda)|i\rangle}{\langle\ell(\lambda)|j\rangle} \langle i|\mathbb{W}_\omega(\lambda)|j\rangle - \sum_i \langle i|j\rangle \psi_\omega(\lambda) \\ &= \frac{\langle\ell(\lambda)|\mathbb{W}_\omega(\lambda)|j\rangle}{\langle\ell(\lambda)|j\rangle} - \psi_\omega(\lambda) \\ &= 0. \end{aligned} \quad (4.32)$$

The last line follows because $\langle\ell(\lambda)|$ is the left eigenvector of the tilted operator with eigenvalue $\psi_\omega(\lambda)$.

Since $\mathcal{W}(\lambda)$ is a rate matrix for all values of λ , it generates a probability-conserving dynamics, but we still must show that this auxiliary dynamics is in some sense equivalent to conditioning the entropy production. We will do this by explicitly comparing the probability a trajectory, $\mathbf{x}(t)$, is generated by the auxiliary dynamics with its probability in the tilted ensemble. Notice that the tilted ensemble probability can be simplified from Eqs. (4.29) and (4.30),

$$P_{\text{tilted}}[\mathbf{x}(t), \lambda] \propto e^{-\lambda\omega[\mathbf{x}(t)]} \rho_{\text{ss}}(\mathbf{x}_0) \prod_{\alpha=0} \mathbb{W}_{\mathbf{x}_{\alpha+1}, \mathbf{x}_\alpha} e^{-R_{x_\alpha}(t_{\alpha+1} - t_\alpha)} \quad (4.33)$$

$$= \rho_{\text{ss}}(\mathbf{x}_0) \prod_{\alpha=0} (\mathbb{W}_{\mathbf{x}_{\alpha+1}, \mathbf{x}_\alpha})^{1-\lambda} (\mathbb{W}_{\mathbf{x}_\alpha, \mathbf{x}_{\alpha+1}})^\lambda e^{-R_{x_\alpha}(t_{\alpha+1} - t_\alpha)}. \quad (4.34)$$

The probability of generating $\mathbf{x}(t)$ using the auxiliary dynamics can be similarly expressed up to a normalization constant.

$$P_{\text{auxiliary}}[\mathbf{x}(t), \lambda] \propto \rho_{\text{ss}}^{\text{aux}}(\mathbf{x}_0, \lambda) \prod_{\alpha=0} \mathcal{W}_{\mathbf{x}_{\alpha+1}, \mathbf{x}_\alpha} e^{-\mathcal{R}_{x_\alpha}(t_{\alpha+1} - t_\alpha)}, \quad (4.35)$$

where $\mathcal{R}_i = -\mathcal{W}(\lambda)_{ii}$ is the sum of all auxiliary rates leaving site i . From the definition of our auxiliary rates, Eq. (4.31), it is simple to see that

$$\mathcal{R}_i = -\mathbb{W}_\omega(\lambda)_{ii} + \psi_\omega(\lambda) = -\mathbb{W}_{ii} + \psi_\omega(\lambda) = R_i + \psi_\omega(\lambda). \quad (4.36)$$

Using this relation, we simplify the probability of generating $\mathbf{x}(t)$ with auxiliary dynamics,

$$\begin{aligned} P_{\text{auxiliary}}[\mathbf{x}(t), \lambda] &\propto \rho_{\text{ss}}^{\text{aux}}(\mathbf{x}_0, \lambda) \prod_{\alpha=0} \frac{\langle \ell(\lambda) | \mathbf{x}_{\alpha+1} \rangle}{\langle \ell(\lambda) | \mathbf{x}_\alpha \rangle} (\mathbb{W}_{\mathbf{x}_{\alpha+1}, \mathbf{x}_\alpha})^{1-\lambda} (\mathbb{W}_{\mathbf{x}_\alpha, \mathbf{x}_{\alpha+1}})^\lambda e^{-(R_{x_\alpha} + \psi_\omega(\lambda))(t_{\alpha+1} - t_\alpha)} \\ &= \rho_{\text{ss}}^{\text{aux}}(\mathbf{x}_0, \lambda) e^{-t_{\text{final}}\psi_\omega(\lambda)} \frac{\langle \ell(\lambda) | \mathbf{x}_{\text{final}} \rangle}{\langle \ell(\lambda) | \mathbf{x}_0 \rangle} \prod_{\alpha=0} (\mathbb{W}_{\mathbf{x}_{\alpha+1}, \mathbf{x}_\alpha})^{1-\lambda} (\mathbb{W}_{\mathbf{x}_\alpha, \mathbf{x}_{\alpha+1}})^\lambda e^{-R_{x_\alpha}(t_{\alpha+1} - t_\alpha)}. \end{aligned} \quad (4.37)$$

We have taken the initial time, t_0 , to be 0 and have written the time of the final observed hop as t_{final} . The last line results from a telescoping cancellation of almost all terms of the form $(\langle \ell(\lambda) | \mathbf{x}_{\alpha+1} \rangle e^{-t_{\alpha+1}\psi_\omega(\lambda)}) / (\langle \ell(\lambda) | \mathbf{x}_\alpha \rangle e^{-t_\alpha\psi_\omega(\lambda)})$. The ratio of auxiliary and tilted probabilities,

$$\frac{P_{\text{auxiliary}}[\mathbf{x}(t), \lambda]}{P_{\text{tilted}}[\mathbf{x}(t), \lambda]} \propto \frac{\rho_{\text{ss}}^{\text{aux}}(\mathbf{x}_0, \lambda) \langle \ell(\lambda) | \mathbf{x}_{\text{final}} \rangle}{\rho_{\text{ss}}(\mathbf{x}_0) \langle \ell(\lambda) | \mathbf{x}_0 \rangle} e^{-t_{\text{final}}\psi_\omega(\lambda)}, \quad (4.38)$$

depends only on the endpoints of the trajectory, \mathbf{x}_0 and $\mathbf{x}_{\text{final}}$. Thus while the two ensembles are not exactly equivalent, they differ only by surface terms. For long trajectories, this means the auxiliary dynamics is an appropriate mimic of the natural dynamics conditioned upon a biased entropy production.

Armed with the auxiliary dynamics, it is possible to efficiently sample long trajectories in the tilted ensemble. The auxiliary dynamics can be used to generate trial trajectories which are re-weighted according to $P_{\text{tilted}}[\mathbf{x}(t), \lambda]$ in the usual MCMC manner. In Chapter 2 we argued that it is productive to think of these TPS moves as an attempt to produce entropy in the abstract space of trajectories. In that language, generating trial TPS moves with the auxiliary dynamics produces a sub-extensive amount of entropy in the trajectory space, thereby avoiding the problems that were discussed in Section 2.4. Unfortunately, we have seen that constructing the auxiliary dynamics requires knowledge of the maximal left eigenvector of the tilted operator, which typically cannot be found for problems requiring path sampling. There is significant interest in using these insights to develop iterative sampling schemes, i.e., guess a form of the eigenvector, sample with that imperfect auxiliary dynamics, improve the guess, and repeat. However, for many-particle dynamics the tilted operator acts on a vast state space of all possible static configurations. Any guess for the eigenvector of this operator requires introducing an effective (and modest-dimensional) basis set, not unlike the challenges faced by the quantum chemistry community.

Chapter 5

Dynamic Phases

Large dynamical fluctuations and dynamical heterogeneity are characteristic features of non-equilibrium chemical and biological systems. Important examples include fluctuations in currents and transport properties of molecular motors [34], dynamic instability in actin and microtubule growth [22, 39], dynamical heterogeneity in cell migration [8], and intermittency in cell growth rates [10]. Large deviation theories and statistical mechanics on the level of trajectories provide convenient frameworks to characterize the dynamical fluctuations. Of particular interest to the present work are the emergence of dynamic phases analogous to the emergence of phases in the conventional statistical mechanics of first order phase transitions [50, 112]. The existence of dynamic phases indicates that the most probable trajectories naturally cluster into classes with distinct dynamical properties. As in equilibrium statistical mechanics, a very productive perspective on the origins and consequences of dynamic phase transitions can be gained by scrutinizing the statistics of pertinent order parameters. A hump or “fat tail” in the wings of such distributions can reveal the presence of a second dynamic phase. Importantly, the separation of trajectories into distinct classes can be made rigorous by demonstrating a singularity in the appropriate scaled cumulant generating function [112]. Conversely, demonstrating such a singularity implies a broad distribution for dynamical fluctuations, which can rationalize experimentally observed dynamical heterogeneity.

This perspective has been elaborated in several interesting contexts [17, 43], albeit in most cases for complicated many-body systems that do not permit full analytical solutions and are thus not entirely transparent. Notable examples include lattice and molecular models of glasses [19, 64], asymmetric exclusion processes [35] and zero-range processes [61]. It has recently been shown that similarly complex behavior can emerge in seemingly very simple systems which do permit an analytical treatment. Specifically, we have shown that a dynamic phase transition can be demonstrated analytically for a biased random walker on a ring with a single impurity in the transition rates [115]. The relatively simple analytics of our random walker model provides an excellent arena for addressing two basic questions about dynamic

Most portions of this chapter have appeared previously in *Physical Review E* [56, 115].

phase transitions. Firstly, under what conditions will a dynamic phase transition emerge? Secondly, are there physical methods for modulating the dynamics to achieve coexistence between dynamic phases or to induce transitions between them?

To this end, here we investigate the statistics of two dynamical order parameters whose fluctuations can reveal the phase transition. We analytically construct the joint rate function for entropy production (Eq. 5.1) and dynamical activity [49] (Eq. 5.2), which is analogous to a two dimensional free energy surface. The two-dimensional rate function in all cases reveals two basins, corresponding to two distinct classes of trajectories, one localized and the other delocalized. However, when one of the order parameters is integrated out, the remaining marginal distribution does not necessarily reveal the underlying bistability. In particular, we show regimes for which the dynamical activity statistics is influenced by two dynamic phases while the fluctuations in entropy production reveal only a single phase.

The dynamic phase transition implies the existence of a rare localized class of trajectories [115]. We investigate conditions required to induce the transition, thereby causing the localized trajectories to become typical. In conventional statistical mechanics a rare phase can be made dominant by adjusting intensive fields like temperature, pressure, or chemical potential. The statistical mechanics of trajectories is more complicated as the field conjugate to a dynamical order parameter (the λ or s field throughout this chapter) is time-non-local and therefore cannot be experimentally tuned in a straightforward way. We construct Markov matrices which (in the long time limit) are equivalent to the natural dynamics with a λ or s field [28, 68]. These Markov matrices reveal the *physical* values of the rate constants which would place the two dynamic phases at coexistence. In other words, with the computed set of rate constants, long trajectories switch back and forth equally between localized and delocalized behavior. Using the Markov matrices that generate effective λ field dynamics, we also show that λ field biasing cannot induce non-equilibrium currents that violate detailed balance. These biasing techniques can amplify (or suppress) existing non-equilibrium currents, but when applied to an equilibrium system the methods simply transform from one detail balanced dynamics to another.

Finally, we consider the problem of observed heterogeneity in cell growth rates and apply results from our model system to elucidate this phenomenon. In particular, it has been observed that a stochastic subpopulation of cells in an *E. Coli* colony exhibit markedly reduced growth rates [10]. These cells, labeled persisters, are more likely to survive antibiotic treatment [77]. Treating our model system as an extremely simplified version of the cell growth cycle, we argue that the phenomenon of persistence should be a generic consequence of a class of localized trajectories that is rare in the absence of antibiotics. We show how treating cells with different strengths of antibiotics in experiments might be equivalent to effectively tuning a λ field and induce a transition between different dynamical behaviors. We also note that coexistence in the space of trajectories can facilitate massive dynamical fluctuations which are evocative of those observed in other biological contexts such as growing polymers including microtubules [88], actin [47], and bacterial homologs thereof [38, 48, 97], where trajectories exhibit a stark switching between growing and collapsing behaviors. Our work clarifies the conditions required for such phase coexistence in trajectories and also

illuminates the properties of the phase transition.

The structure of the chapter is as follows. In Section 5.1 we review the basic structure of the large deviation calculations. We then introduce our solvable model system in Section 5.2 and derive the scaled cumulant generating function, the Legendre transform of which yields the entropy production and activity statistics. Using this result, we discuss in Section 5.3 the nature of a dynamic phase transition and the conditions for which the transition can be observed by these order parameters. Finally, we address implications of such a dynamic phase transition. We both identify conditions for dynamical coexistence in which the two phases contribute equally and discuss the way in which the response of cells to antibiotic treatment may expose a similar underlying transition.

5.1 Framework

We consider continuous-time Markovian dynamics on a discrete state space. Such a stochastic dynamics is compactly represented by a master equation with rate matrix \mathbb{W} whose off-diagonal elements \mathbb{W}_{ij} detail the rates of transition from state j to state i [70]. The probability distribution of the set of all possible trajectories is well-defined in the steady-state. We investigate both typical and rare dynamical fluctuations by considering the behavior of dynamic order parameters.

Time-additive dynamic order parameters are particularly relevant to many experiments as they report on cumulative dynamical behavior, for example the net current observed in a finite time experiment. In this chapter we consider two such order parameters, the entropy production and the dynamical activity. The entropy production of a trajectory is defined in the stochastic thermodynamics sense as the log ratio of forward and reverse probabilities [103]. We focus on continuous time hopping processes, in which case the time-extensive part of the entropy production can be expressed as

$$\omega = \sum_{\text{hops}} \ln \frac{k_f}{k_r}, \quad (5.1)$$

where k_f and k_r are the forward and reverse rate constants for each hop. The dynamical activity, K , simply counts the total number of hops.

$$K = \sum_{\text{hops}} 1 \quad (5.2)$$

This accounting of microscopic transitions has been used most predominantly in the study of glassy dynamics [49]. Whereas the entropy production provides a measure of the dissipation associated with a trajectory, the dynamical activity indicates how labile the dynamics is. By considering both order parameters we highlight how the statistics of various observables may be differently affected by the dynamic phase transition.

The time-additivity of these order parameters allows their probability distribution to be described by a large deviation form,

$$P(\sigma, K/t) \approx e^{-tI(\sigma, K/t)}, \quad (5.3)$$

where $I(\sigma, K/t)$ is the joint large deviation rate function and $\sigma = \omega/t$ is the entropy production rate. The rate function $I(\sigma, K/t)$ can be computed as the Legendre transform of the scaled cumulant generating function [74, 112],

$$\psi_{\omega,K}(\lambda, s) = \lim_{t \rightarrow \infty} \frac{1}{t} \ln \langle e^{-\lambda\omega - sK} \rangle, \quad (5.4)$$

where the expectation value is taken over trajectories initialized in the steady state distribution. This function can in turn be obtained as the maximum eigenvalue of a tilted operator, $\mathbb{W}_{\omega,K}(\lambda, s)$, which is simply related to \mathbb{W} [74]. Specifically the matrix elements are given by

$$\mathbb{W}_{\omega,K}(\lambda, s)_{ij} = (1 - \delta_{ij}) \mathbb{W}_{ij}^{1-\lambda} \mathbb{W}_{ji}^\lambda e^{-s} + \delta_{ij} \mathbb{W}_{ij}. \quad (5.5)$$

By solving for the eigenspectrum of $\mathbb{W}_{\omega,K}(\lambda, s)$ we can thus compute the long time limit of $P(\sigma, K/t)$ via a Legendre transform.

Fig. 5.1 graphically illustrates the relationships between probability distributions for the dynamic order parameters, rate functions, and scaled cumulant generating functions. In particular, the singularities in $\psi_{\omega,K}(\lambda, s)$ generate bistable order parameter distributions. For the type of ergodic dynamics studied here these bistable distributions tend toward a strictly concave rate function in the long time limit [113], which is the Legendre transform of the scaled cumulant generating function with a Maxwell construction. Despite the underlying bistability of the distribution shown in the Fig. 5.1(d), the marginals of that distribution need not illustrate a bistability, if the two basins are appropriately aligned. We now shift our attention to a particular solvable model, whereby computing $\psi_{\omega,K}(\lambda, s)$ we can determine conditions for phase transitions in the two order parameters.

5.2 Analytic Solution to 1d Random Walker on a Ring with a Heterogeneity

We consider dynamics of a single particle on a network of N states arranged in a ring as depicted in Fig. 5.2. Clockwise rates are given by x and counterclockwise rates by 1 except for the rates at a single heterogeneous link, which are given by h_1 and h_2 , respectively. A trajectory on the network corresponds to a sequence of hops from state to state with a Poisson-distributed waiting time between hops determined by the rate constants x , h_1 , and h_2 . Without loss of generality we focus on the case that $x > 1$ such that typical trajectories cycle in the clockwise direction. For generic choices of h_1 and h_2 the dynamics is out-of-equilibrium, which can be seen most simply since the probability of clockwise cycles differs from that of counter-clockwise cycles [101]. Because the network supports only a single

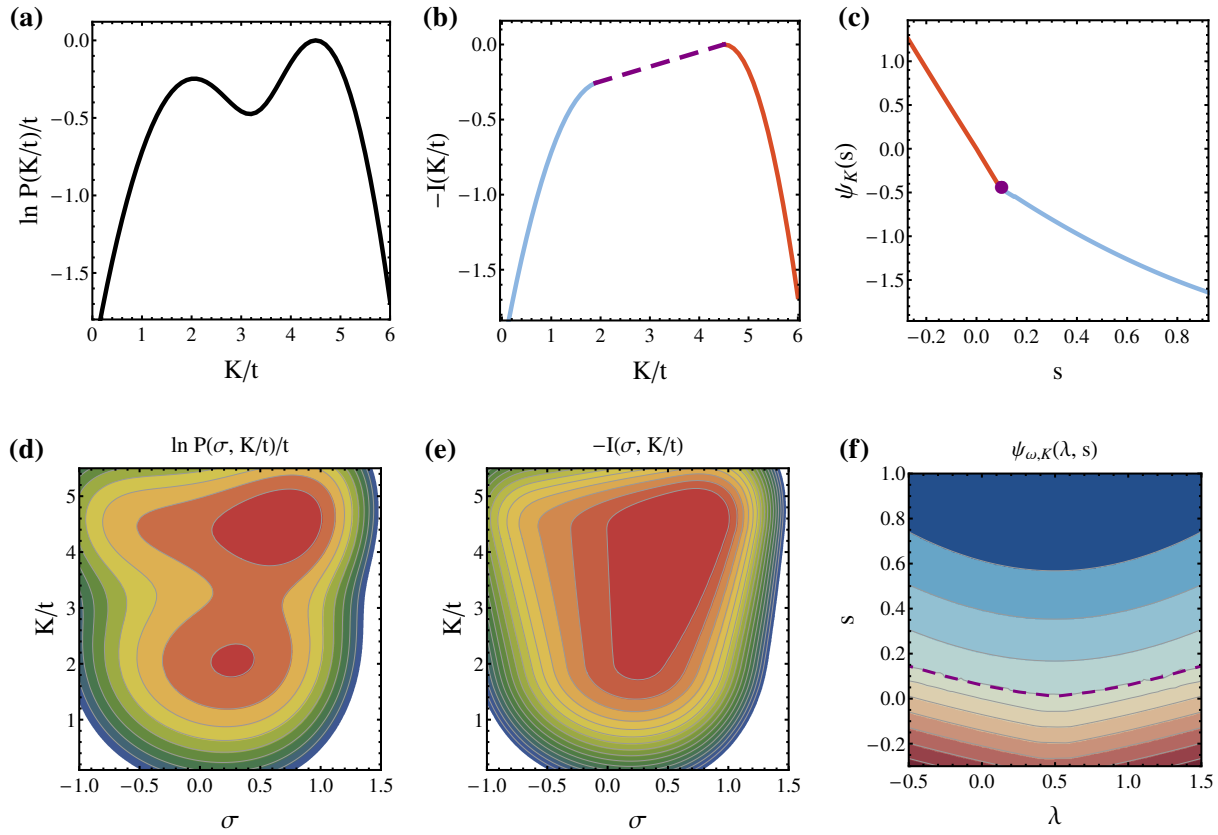


Figure 5.1: Schematic illustrating the relationships between order parameter probability distributions collected in a finite time experiment (a, d), rate functions (b, e), and cumulant generating functions (c, f) in one and two dimensions. The rate function is the concave (for our sign convention) hull of the finite time distribution and the Legendre transform of the scaled cumulant generating function. The bimodality of the finite time distribution results in a so-called tie line in the concave hull, represented as a dashed line in the 1d rate function. The tie line necessitates a singularity in the scaled cumulant generating function, depicted as a dot in (c) and as a dashed line in (f). Note that the 1d cumulant generating functions for activity (entropy production) are given by the $\lambda = 0$ ($s = 0$) slice in (f).

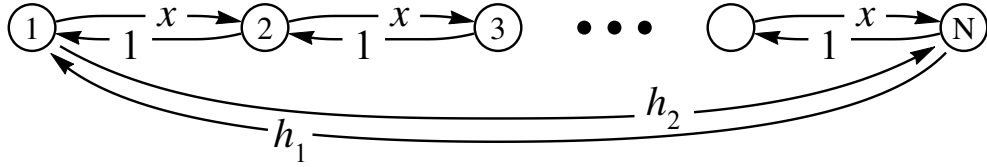


Figure 5.2: Network of states and the rates for transitioning between the states. For certain choices of x , h_1 , and h_2 we demonstrate a dynamic phase transition in entropy production and dynamical activity rates.

cycle, it is one of the simplest models for non-equilibrium dynamics. This simplicity enables an analytic solution in the limit that the ring grows infinitely large. Because analytically solvable non-equilibrium models are few, these solutions can provide a useful reference point.

We focus on a large N limit which maintains the discrete nature of the states. This limit is appropriate for chemical reaction kinetics with transitions among a discrete set of states [70]. It may also be interesting to consider continuum limits with rates scaled by N . Such a continuum limit is pertinent to a Brownian particle confined to a ring [58], and has been discussed in a Freidlin-Wentzell framework without a heterogeneity in the limit of small noise [44].

Following the framework of Section 5.1, the tilted operator can be written down straightforwardly as

$$\mathbb{W}_{\omega,K}(\lambda, s) = \begin{pmatrix} -x - h_2 & x^\lambda e^{-s} & \dots & h_1^{1-\lambda} h_2^\lambda e^{-s} \\ x^{1-\lambda} e^{-s} & -1 - x & \dots & 0 \\ \vdots & \vdots & \ddots & \vdots \\ h_1^\lambda h_2^{1-\lambda} e^{-s} & 0 & \dots & -h_1 - 1 \end{pmatrix}. \quad (5.6)$$

For modest N one can numerically calculate the largest eigenvalue of this matrix to yield the scaled cumulant generating function $\psi_{\omega,K}(\lambda, s)$. In the large N limit, however, we can obtain an analytic form for the limiting behavior using a perturbation theory we recently outlined [115].

Were it not for the heterogeneous link, there would be a translational symmetry allowing the tilted operator to be exactly diagonalized via a Fourier transform. For λ and s in a particular region of the (λ, s) plane, the maximum eigenvalue of the tilted operator in Eq. (5.6) coincides with this solution for the translationally symmetric network in the large N limit. $\psi_{\omega,K}(\lambda, s)$ exhibits a cusp along the boundary of this region. One side of the boundary corresponds to a maximal right eigenvector of the tilted operator which is delocalized while on the other side the eigenvector is exponentially localized around the heterogeneous link. The discontinuity of the slopes of $\psi_{\omega,K}(\lambda, s)$ when crossing this boundary indicates a dynamic phase transition between classes of trajectories which are localized and those which are delocalized. The detailed calculation, provided in Appendix E, reveals that the line of cusps separating localized from delocalized eigenvectors is given by the logarithm of the roots of a

quadratic,

$$s^*(\lambda) = \ln \left(\frac{1 + x - h_1 - h_2 - \sqrt{(h_1 - x - h_2 + 1)^2 + 4(h_2 - 1)(h_1 - x)h_1 h_2 x^{-2(|\lambda - \frac{1}{2}| + \frac{1}{2})}}}{2(h_2 - 1)(h_1 - x)x^{-(|\lambda - \frac{1}{2}| + \frac{1}{2})}} \right) \quad (5.7)$$

This equation, corresponding to the purple dashed curve in the schematic of Fig. 5.1(f), is plotted for particular choices of x, h_1 , and h_2 in Fig. 5.3(a).

Remarkably, the value of $\psi_{\omega,K}(\lambda, s)$ everywhere can be determined by the solution to the translationally symmetric network and the form of $s^*(\lambda)$. This follows since $\psi_{\omega,K}(\lambda, s)$ is continuous and the partial derivatives with respect to λ must vanish in the localized regime¹. The translationally symmetric network solution evaluated along the line of cusps thus provides the maximum eigenvalue in the localized region giving

$$\psi_{\omega,K}(\lambda, s) = \begin{cases} x^{1-\lambda} e^{-s} + x^\lambda e^{-s} - 1 - x, & s \leq s^* \\ x^{1-\lambda^*} e^{-s} + x^{\lambda^*} e^{-s} - 1 - x, & s > s^*, \end{cases} \quad (5.8)$$

where s^* and λ^* are shorthand for $s^*(\lambda)$ given in Eq. (5.7) and for the inverse function $\lambda^*(s)$ ². This is our primary analytical result, which enables the computation of the probability distributions for entropy production and activity rates. To prevent confusion, we note that the schematic of Fig. 5.1 was meant to depict generic joint distributions for activity and entropy production and does not illustrate $\psi_{\omega,K}(\lambda, s)$ for this particular solved model.

5.3 Properties of the Phase Transition

Tilted Operator Eigenvectors

Thus far we have merely asserted that the trajectories have localized and delocalized character in the two dynamic phases, but here we more formally make the claims by analyzing the maximal right eigenvectors of the tilted operator. We write the elements of the maximal eigenvector as (f_1, f_2, \dots, f_N) and note that the eigenvalue equation implies a recursion relation between neighboring f_i 's in the bulk.

$$\begin{pmatrix} f_i \\ f_{i+1} \end{pmatrix} = \begin{pmatrix} \frac{\psi+1+x}{e^{-s}x^{1-\lambda}} & -x^{2\lambda-1} \\ 1 & 0 \end{pmatrix} \begin{pmatrix} f_{i+1} \\ f_{i+2} \end{pmatrix} = B \begin{pmatrix} f_{i+1} \\ f_{i+2} \end{pmatrix},$$

where we have introduced the transfer matrix B and suppressed the subscripts and arguments on $\psi_{\omega,K}(\lambda, s)$. The n^{th} component of the eigenvector can thus be written in terms of the two eigenvalues of B , k_1 and k_2 . Specifically,

$$f_n \propto (k_1^{-1})^n + \epsilon k_2^{(N-n)}, \quad (5.9)$$

¹Localized eigenvectors of the tilted operator correspond to localized trajectories, which cannot produce entropy in the long-time limit. Partial derivatives with respect to λ must then yield a zero entropy production.

²There is not a unique inverse, but the sum $x^{1-\lambda^*} + x^{\lambda^*}$ is the same for either choice of the inverse.

where $k_1 > 1$ and $k_2 < 1$. The parameter ϵ serves to match up the boundary conditions between f_1 and f_N . When $\lambda < \lambda^*$, the eigenvalues of B can be expressed as $k_1 = e^{-\gamma/N}$, and $k_2 = x^{2\lambda-1}e^{\gamma/N}$ correct up to second order in $1/N$. An expression for γ in terms of the rate constants, Eq. (E.6), follows from the full calculation of the maximum eigenvalue in Appendix E. Hence the maximal right eigenvector is found to have components

$$f_n \propto e^{\gamma n/N} + \epsilon_{\text{deloc}} e^{((2\lambda-1)N \ln x + \gamma)(N-n)/N}, \quad (5.10)$$

where $\epsilon_{\text{deloc}} = h_1^{\lambda-1}h_2^{-\lambda}(x^{1-\lambda} + h_2 - 1) - e^\gamma$. The first term in Eq. (5.10) decays slowly over the entire range of the system, giving the eigenvector a delocalized character. This delocalized character indicates that trajectories with high rates of entropy production and activity can be found regularly visiting all of the states of the system.

Under the conditions that $s > s^*(\lambda)$ the expression for γ diverges, and the delocalized form for the maximal eigenvector given in Eq. (5.10) must break down³. We anticipate a similar functional form for the eigenvectors except with some nonzero κ replacing γ/N . Indeed, with some tedious algebra it can be shown that the right eigenvectors are given by

$$f_n \propto e^{\kappa n} + \epsilon_{\text{loc}} e^{((2\lambda-1) \ln x + \kappa)(N-n)} \quad (5.11)$$

with $\kappa = (\lambda^* - \lambda) \ln x$ and $\epsilon_{\text{loc}} = h_1^{\lambda-1}h_2^{-\lambda}(x^{1-\lambda^*} + h_2 - 1) e^\kappa$. Unlike the case of the delocalized eigenvector, this solution is strongly localized around the heterogeneous link. Thus the flat region between the two cusps in $\psi_\omega(\lambda) \equiv \psi_{\omega,K}(\lambda, 0)$ stems from a class of localized trajectories which are incapable of producing entropy in the long-time limit. The two dynamic phases can therefore be thought of as the classes of localized and delocalized trajectories, each of which contributes its own feature to the rate function.

Entropy Production Statistics

We previously reported on the entropy production statistics in the special case that $h_1 = h_2$ [115], but this restriction was lifted in the preceding analysis. Surprisingly, allowing for distinct values of h_1 and h_2 can yield a qualitative difference in the entropy production rate statistics. When h_1 and h_2 are constrained to be equal, all values of h and x give rise to singularities in $\psi_\omega(\lambda)$ and therefore a dynamic phase transition with respect to the entropy production rate. By solving for the conditions when $s^*(\lambda) = 0$ in Eq. (5.7) one can obtain the position of these two cusps in $\psi_\omega(\lambda)$, λ^* and $1 - \lambda^*$.

When h_1 and h_2 are distinct, however, there are conditions for which $s^*(\lambda)$ lacks roots. The fluctuation theorem [74] entails a symmetry in the cumulant generating function $\psi_\omega(\lambda)$ about $\lambda = 1/2$. Because of this symmetry, the marginal case where the dynamic phase transition disappears occurs when $\lambda^* = 1/2$. Solving for the condition that $s^*(1/2) = 0$ thus

³Note that the cusp in the scaled cumulant generating function does not result from a simple eigenvalue crossing nor an avoided crossing as the delocalized vector ceases to be an eigenvector on the wrong side of the transition.

gives a critical value of x ,

$$x_c = \frac{1}{2} \left(1 + 2h_1 - 2h_2 + h_2^2 - (h_2 - 1) \sqrt{1 + 4h_1 - 2h_2 + h_2^2} \right), \quad (5.12)$$

so that $\psi_\omega(\lambda)$ will have cusps indicating a dynamic phase transition if and only if $x > x_c$. Indeed, Fig. 5.3 illustrates that the singularities are no longer present when x drops below the critical value x_c . It is of particular note that the criticality does not occur at the trivial limit $x = h_1/h_2$, the condition for which hops across the heterogeneous link produce the same amount of entropy as hops across any other link.

The existence of a critical value of x can be understood more clearly by examining the large deviation rate function for the entropy production, $I(\sigma)$, which is obtained from a Legendre transform of $\psi_\omega(\lambda)$. In Fig. 5.4 we plot these rate functions for a variety of values of x but for the same value of h_1 and h_2 . As x is decreased, the system is biased less strongly toward clockwise cycles, and the average entropy production rate decreases correspondingly. However, even when the average entropy production rate is large, the class of localized trajectories present a way for a trajectory to produce zero entropy. Therefore a broad entropy production distribution with a hump at $\sigma = 0$ is present for large x . When x is decreased below x_c , this shoulder at $\sigma = 0$ gets completely engulfed by the natural fluctuations in entropy production characterizing the dominant (delocalized) class of trajectories. Thus the disappearance of the dynamic phase transition corresponds to the condition when near-zero entropy production rates are more likely to be obtained by a delocalized trajectory than by a localized trajectory. As we shall demonstrate shortly, the lack of the dynamic phase transition in the entropy production order parameter does not rule out the presence of two classes of trajectories. A dynamic phase transition can still be recovered by studying the statistics of dynamical activity.

Dynamical Activity Statistics

The statistics for the dynamical activity can be deduced in the same way by setting $\lambda = 0$ in Eq. (5.8). The activity does not satisfy a fluctuation theorem, so there is no symmetry corresponding to $\psi_\omega(\lambda) = \psi_\omega(1 - \lambda)$. As a consequence, $\psi_K(s) \equiv \psi_{\omega,K}(0, s)$ has a cusp at $s^*(0)$ for all values of the rate constants as is clear from the $\lambda = 0$ intercepts of Fig. 5.3.

The Legendre transform of $\psi_K(s)$ gives the rate function for dynamical activity, shown in Fig. 5.4. Like the case of entropy production, as x is decreased the average activity decreases, but now the tie line (and correspondingly the dynamic phase transition) persists for all choices of x . Remarkably, this implies that there is a regime with $x < x_c$ where the activity exhibits a dynamic phase transition but the entropy production does not. Consequently the entropy production distribution in this parameter regime converges to the distribution found in a translationally symmetric network, while the distribution for dynamical activity resolves the impact of the heterogeneity.

To better appreciate the manner in which a dynamic phase transition can be observed with respect to one order parameter but not another, we Legendre transform $\psi_{\omega,K}(\lambda, s)$ and

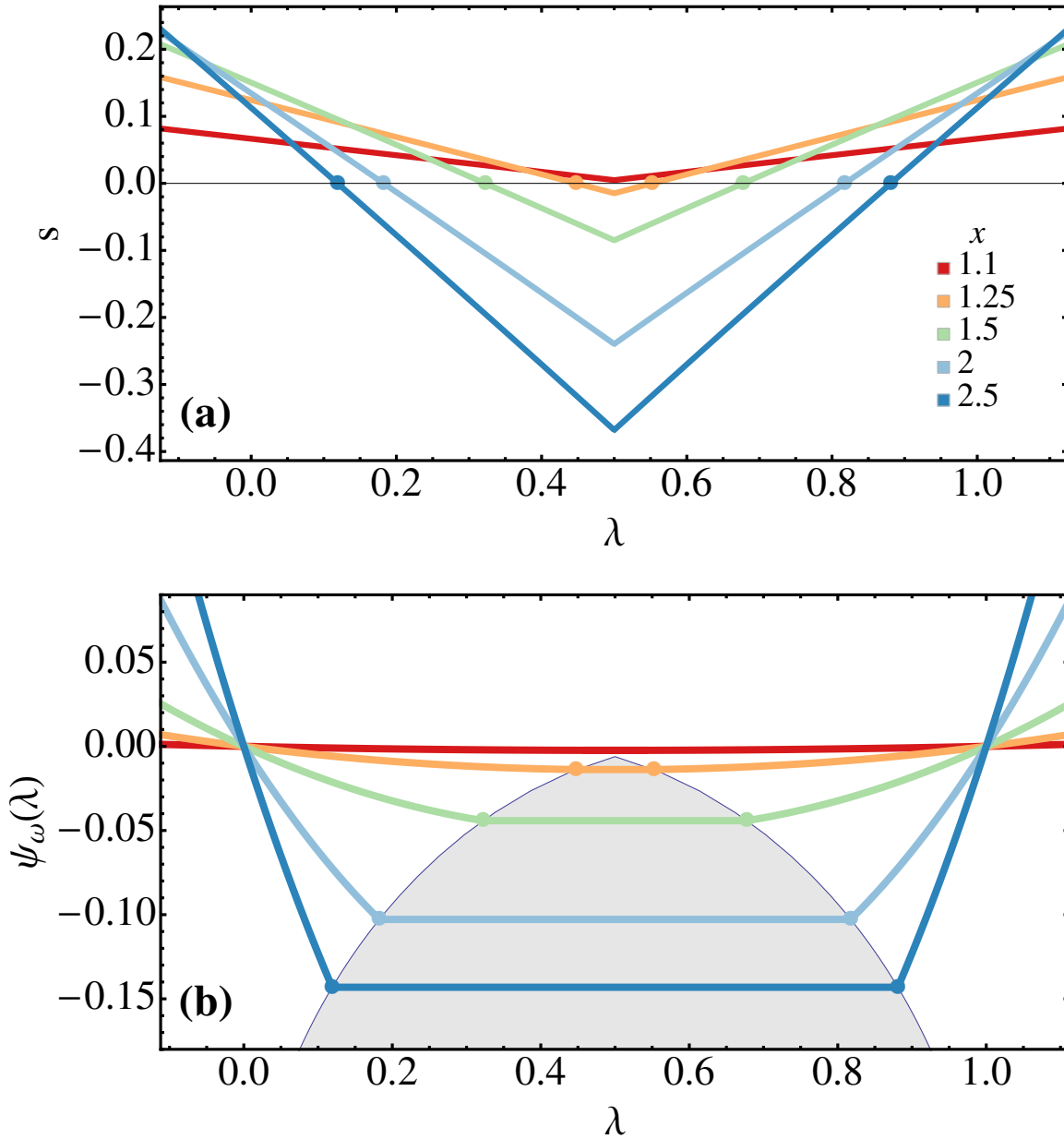


Figure 5.3: (a) Curve of the cusp in $\psi_{\omega,K}(\lambda, s)$ given by Eq. (5.7) plotted for $h_1 = 0.3$ and $h_2 = 0.2$. This curve corresponds to the dashed line in the schematic of Fig. 5.1(f). Below the curve $\psi_{\omega,K}(\lambda, s)$ has a delocalized eigenvector. For these parameters $x_c \approx 1.163$ such that the $x = 1.1$ curve does not intersect the $s = 0$ axis. (b) $\psi_{\omega}(\lambda)$ for the same conditions. Cusps are marked with a filled dot at $(\lambda^*, \psi_{\omega}(\lambda^*))$ and $(1 - \lambda^*, \psi_{\omega}(1 - \lambda^*))$. The shaded area indicates the region arising from the localized phase.

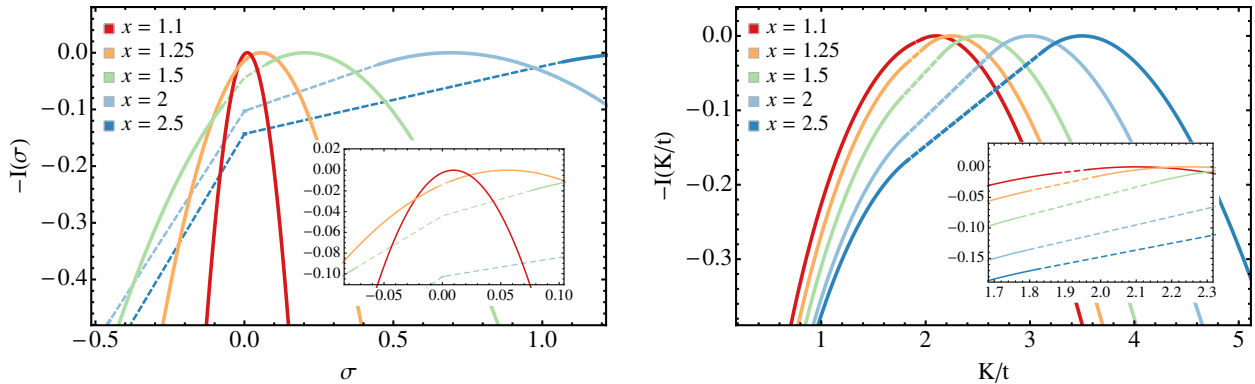


Figure 5.4: Entropy production and activity rate functions for $h_1 = 0.3$ and $h_2 = 0.2$ where $x_c \approx 1.163$. The insets zoom in on the peaks to illustrate that the entropy production rate function lacks a second phase (and consequently does not have the dashed tie lines), while the activity rate function shows two phases even for $x < x_c$. The most likely values of σ and K/t increase with increasing x .

plot the two dimensional rate functions for activity and entropy production. Figs. 5.5(a) and (d) show the rate function for the translationally symmetric network with $x = 1.5$. Note that the surface is smooth, exhibiting only small fluctuations away from the mean behavior. In contrast, when the heterogeneous link is introduced a ridge develops along $\sigma = 0$. This ridge corresponds to the class of localized trajectories, all of which have identically zero entropy production rate in the long time limit. The entropy production and activity rate functions are marginals of this two dimensional surface, which corresponds to projecting the surface onto the σ and K/t axes, respectively. For all values of x , the projection onto the K/t axis results in a broad activity distribution with components from both the localized and delocalized trajectories. The projection onto the σ axis behaves differently. When $x < x_c$ the class of localized trajectories along the ridge are in line with the most likely contributions from delocalized trajectories. Consequently the entropy production distribution will not reveal the localized trajectories since for all possible values of σ there exist more probable delocalized trajectories which produce that particular entropy production rate.

The calculation offers an important lesson which provides insight for more complicated dynamical systems. Our analysis has shown that localized and delocalized trajectories can be clearly separated into two distinct classes. Nevertheless, the underlying transition is only visible in the distribution for certain order parameters. In more complicated systems, one can expect many more than two classes of trajectories. Whether or not these classes constitute a true dynamic phase is intimately related to the symmetries of the dynamic order parameter being probed. Thus an experimenter simultaneously monitoring current, activity, and entropy production distributions may consistently observe large deviations in some order parameters but not in others. We note that similar scenarios can occur in equilibrium statistical mechanics.

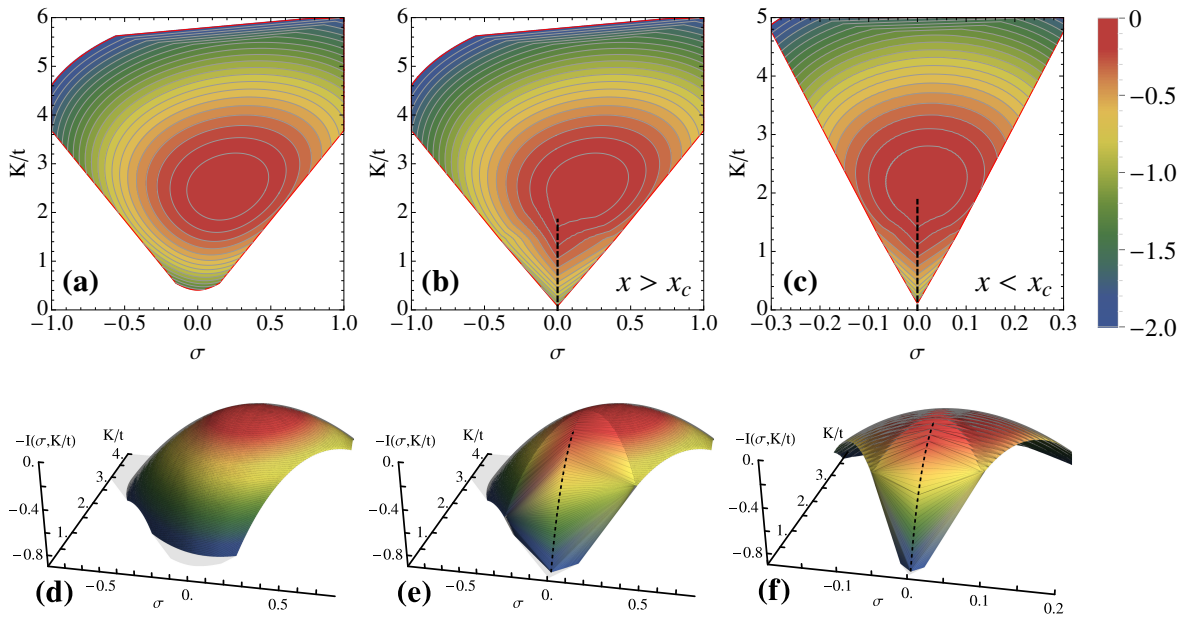


Figure 5.5: Joint rate functions for the activity and entropy production rates. The translationally symmetric case with $x = 1.5$ and no heterogeneity is plotted in (a) and (d). The influence of a heterogeneous link ($h_1 = 0.3, h_2 = 0.2$) is shown in (b) and (e) for $x = 1.5$ and in (c) and (f) for $x = 1.14$. In the presence of the heterogeneity, the rate function develops a set of tie lines to connect two dynamic phases. The localized phase runs along the $\sigma = 0$ ridge (dashed line), enabling fluctuations in K/t but not in σ . The delocalized phase is centered at the peak of the rate function and enables fluctuations in both K/t and σ . Whether x exceeds x_c determines if localized phase is visible to the entropy production axis.

5.4 Flows on Decorated Networks

The ring network of Fig. 5.2 can be thought of as a coarse-grained model for cyclic dynamics, with particular relevance to processes that have heterogeneous rates. We will take this perspective in Section 5.5 when we consider the ring network as a model for cell cycle dynamics. It is clear that cyclical processes, like a cell cycle, must have a ring-like nature since the system returns to its original state. Nevertheless, reduction to a single ring is a particularly crude coarse-graining. Is the perspective of dynamic phase transitions still productive when cyclical processes are coarse grained more gently? In particular, what parts of the analysis change when the dynamical model supports many cycles? To address this question, we introduce a network we call the triangle network, with a collection of N triangular motifs around a ring as shown in Fig. 5.6.

The triangle network tilted operator can be numerically constructed for finite N . The top eigenvalue gives the SCGF for entropy production, $\psi_\omega(\lambda)$, which develops a cusp at λ^* (and

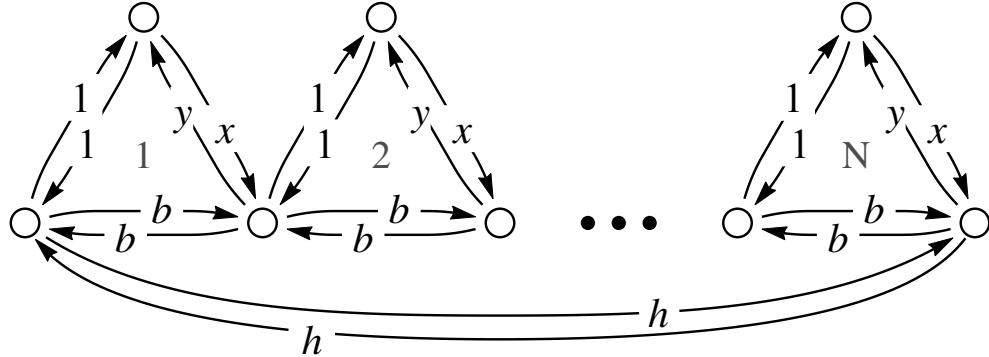


Figure 5.6: A large ring decorated with triangles. This “triangle network” supports local and global cycles unlike the ring network of in Fig. 5.2. Without loss of generality we work with $x > y$ to drive clockwise cycles.

another at $1 - \lambda^*$ by symmetry) as the network grows large. This cusp, shown in Fig. 5.7 for a variety of parameters, emerges in the large N limit for the same reasons it did in the the ring network example. Trajectories may be separated into localized and delocalized dynamic phases based on their propensity to loop around the large cycle. The dynamic phase transition persists when we decorate the global cycle with local loops, but in contrast with the previous calculation, the slope of $\psi_\omega(\lambda)$ does not vanish when $\lambda^* < \lambda < 1 - \lambda^*$. This difference can be understood physically since the behavior of $\psi_\omega(\lambda)$ is determined by the localized phase. The ring network only produces entropy by completing a complete cycle around the macroscopic ring, so the entropy production rate of localized trajectories had to vanish. The triangular motifs, however, enable trajectories which are both localized and entropy-producing.

In the case of the ring network we were able to analytically compute $\psi_\omega(\lambda)$ in the large N limit using a perturbation theory about the symmetric network. While the nature of the triangle network’s localized phase is more complicated, insights from the ring network perturbation theory can be leveraged. In particular, one can introduce localized and delocalized forms of the tilted operator maximal right eigenvector. The delocalized eigenvector behaves as though the triangle network had translational symmetry with no heterogeneous link, and the other eigenvector is localized around the heterogeneity. This approach is carried out in Appendix F. It reduces the computation of the SCGF to the solution of a nonlinear system with two equations and two unknowns. Fig. 5.8 shows that the solution using the ansatz converges to the numerical SCGF in the large network limit.

The triangle network analysis teaches that most of the ring network insights generalize to other pseudo-one-dimensional cyclic networks. We therefore expect that cyclic systems with heterogeneities can exhibit large dynamical fluctuations due to localization/delocalization transitions, even when the ring network appears to be an radical oversimplification. There is

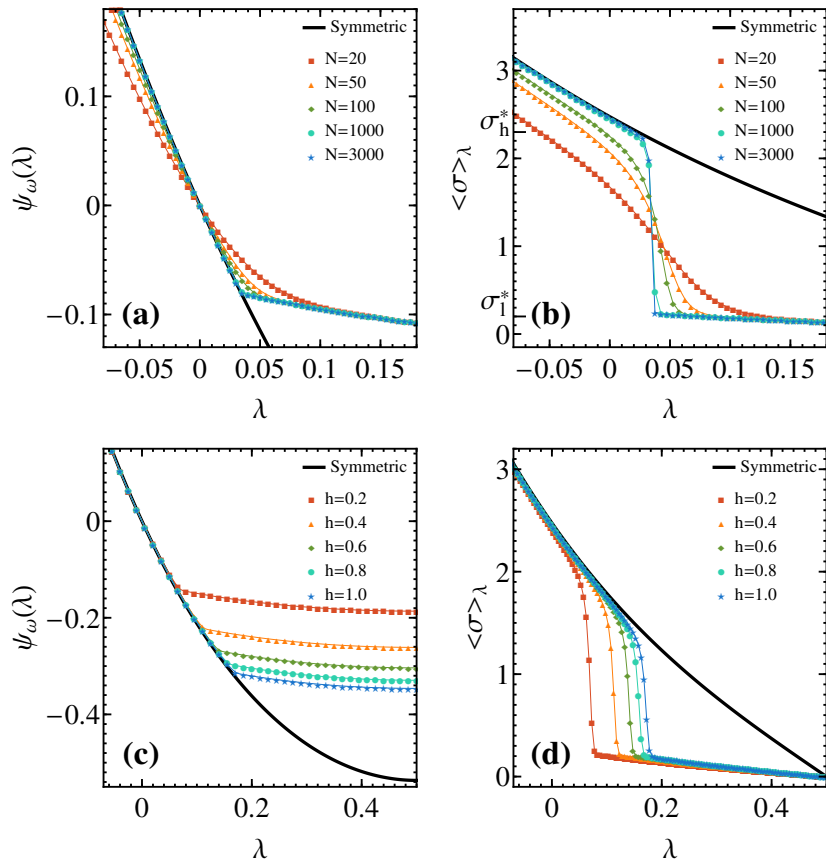


Figure 5.7: Scaled cumulant generating functions and average entropy production rates for the triangle network, depicted in Fig. 5.6. All results are shown for rates $x = 20$, $y = 1$, and $b = 0.1$. Black solid curves show the exact behavior of the symmetric variant for comparison. Plots (a) and (b) show results for a variety of network sizes with $h = 0.1$ for the symmetry-breaking link, suggesting a singularity in the large- N limit. Plots (c) and (d) show results for $N = 200$ with several values for h .

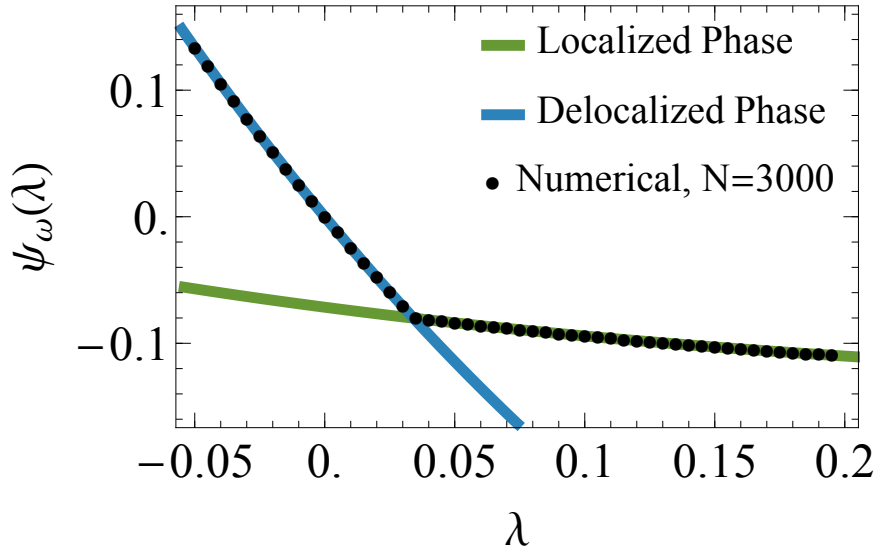


Figure 5.8: Singularity in the SCGF for the triangle network with rate constants $x = 20$, $y = 1$, $b = 0.1$, and $h = 0.1$. Circles show numerical results for the largest eigenvalue of $\mathbb{W}_\omega(\lambda)$ with $N = 3000$ triangular motifs. Analytical treatment of the delocalized and localized phases is provided in the main text.

one minor way in which entropy production fluctuations on the ring are qualitatively different than on a decorated ring. Because decorations enable nonvanishing entropy production in the localized phase, they smooth the corner in the entropy production rate function (compare, for example, the left plot of Fig. 5.4 with Fig. 5.9). The smoothing reflects a distribution for the number of triangular cycles completed by a localized trajectory.

5.5 Physical Implications of Dynamic Phases

Tuning Rates to Coexistence

We have shown that while typical trajectories on the network are delocalized, there exists a rare class of localized trajectories, which in certain cases appears as a distinct dynamic phase. In ordinary statistical mechanics one tunes a Lagrange multiplier like the inverse temperature, β , to induce a transition between phases. Inducing a dynamic transition cannot occur in an identical way since the λ field is conjugate to a time-non-local object. In computer simulations one can place the system in contact with a large bath at a well-defined value of λ , but this treatment requires that the system is the entire trajectory. While it is not possible to directly tune the λ field in an experiment, one can use the eigenvectors of the tilted operator to construct a rate matrix which, in the long-time limit, is equivalent to

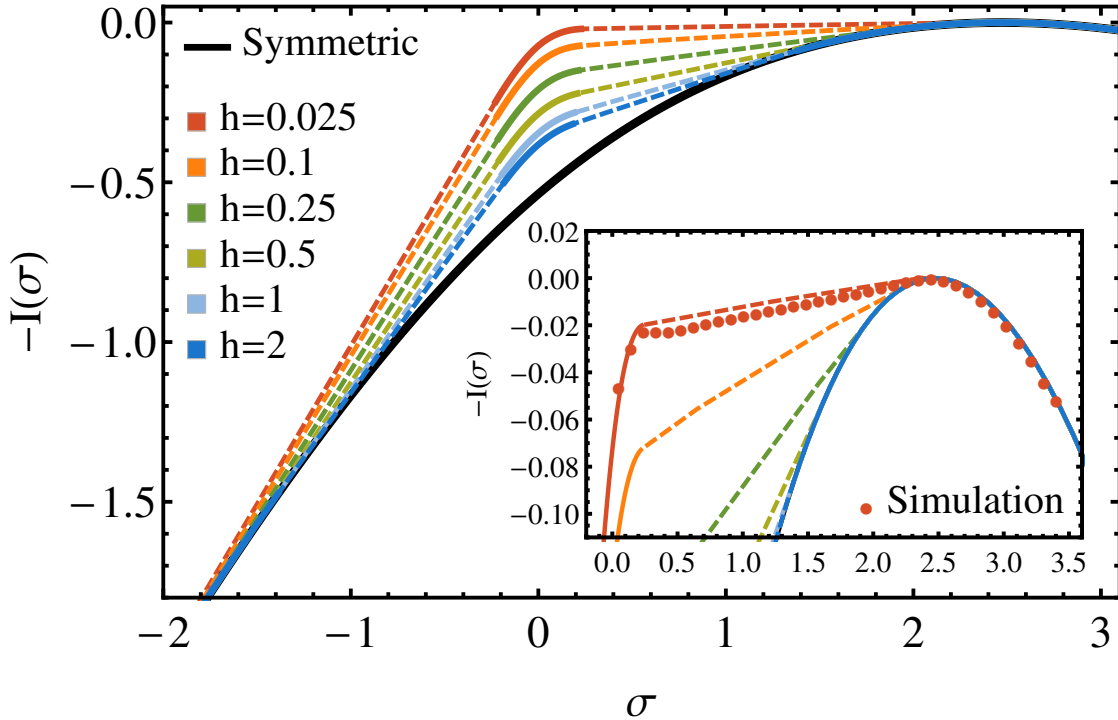


Figure 5.9: Large deviation function $I(\sigma)$ for the entropy production rate of the network in Fig. 5.6 with $x = 20, y = 1, b = 0.1$, and several different values of h . The rate function envelope was determined by the Legendre-Fenchel transform of $\psi_\omega(\lambda)$, whose two singularities require the construction of tie lines (dashed curve). Kinetic Monte Carlo simulation [54] results (10^7 trajectories with $h = 0.025, N = 400$, and $\tau = 250$) are shown as red circles in the inset.

introducing such a λ field [28, 68]. We denote this class of rate matrices for effective λ fields $\mathcal{W}(\lambda)$ with matrix elements given by

$$\mathcal{W}_{ij}(\lambda) = \frac{f_i(\lambda)}{f_j(\lambda)} [\mathbb{W}_\omega(\lambda)]_{ij} - \delta_{ij}\psi_\omega(\lambda), \quad (5.13)$$

where f_n is the n^{th} component of the right eigenvector determined in the large N limit in Eqs. (5.10) and (5.11). A derivation of this result was provided in Section 4.7. For simplicity we limit the analysis to the λ field conjugate to entropy production, but this could of course be repeated for activity.

A cusp in the maximum eigenvalue of the tilted operator $\mathbb{W}_\omega(\lambda)$ indicates that the two dynamic phases will be in coexistence when a λ^* bias is applied. The tilted operator, however, is only a rate matrix at $\lambda = 0$. For all other values of λ the matrix does not conserve probability. In contrast, \mathcal{W} , is a proper rate matrix and can consequently represent physical rates which result in long-time dynamics that exactly mimics the long-time behavior of the

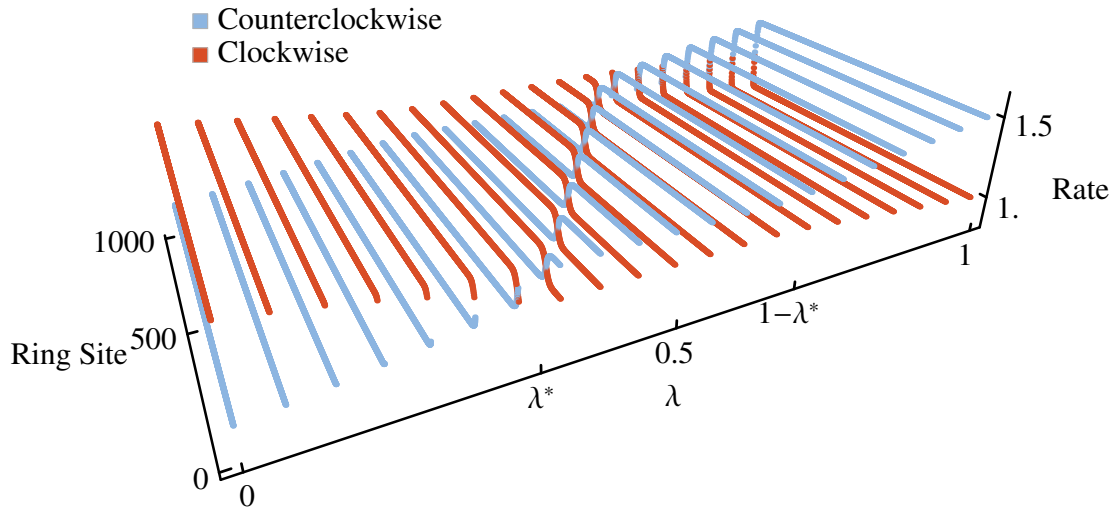


Figure 5.10: The off-diagonal elements of $\mathcal{W}(\lambda)$ give effective rate constants for clockwise and counterclockwise transitions rates after the application of a λ bias. In the absence of λ biasing the transition rates are $h_1 = 0.3$, $h_2 = 0.2$, $x = 1.5$. Note the strong spatial dependence of the effective rate constants between λ^* and $1 - \lambda^*$ where the typical trajectories are localized.

original dynamics subject to a λ^* biasing field. [28, 68]. For our solvable model, we determine the clockwise and counterclockwise rate constants as a function of position around the ring which yield an effective λ bias according to Eq. 5.13. These rates are depicted in Fig. 5.10. When $\lambda = 0$ they are just the rate constants of the natural dynamics, but as λ increases the preference toward low entropy production has two effects. Firstly, the effective clockwise rates decrease while counterclockwise rates increase to yield slower rates of cycling around the ring. With fewer completed cycles per unit time, the trajectories achieve a lower rate of entropy production. Secondly, a strong spatial dependence in the rates arises, particularly as λ nears λ^* . As long as the clockwise rates exceed the counterclockwise rates at every site in the ring, typical trajectories will remain delocalized. In the regime $\lambda^* < \lambda < 1 - \lambda^*$ some regions of the ring prefer clockwise motion while others prefer counterclockwise. The result is a localization at the interface of these regions. As made clear in Fig. 5.10, the effective rates are smoothly tuned by λ , even when passing through the transition. Dynamics evolving under $\mathcal{W}(\lambda^*)$ is particularly interesting as it will exhibit massive fluctuations in entropy production rates. Given that states are connected together in a ring topology, this $\mathcal{W}(\lambda^*)$ gives the physical rate constants which tune the system to dynamical coexistence.

The ring topology is also convenient for demonstrating that λ biasing of detailed balance systems results in dynamics which also obeys detailed balance. This has previously been shown to be the case when biasing activity by an s field by other means [68]. We note that in a network with a cycle loop (like our ring network) the condition of detailed balance is

satisfied if and only if

$$\prod_{i=1}^N \left(\frac{\mathbb{W}_{i,i+1}}{\mathbb{W}_{i+1,i}} \right) = 1 \quad (5.14)$$

i.e. if the product of rates for clockwise transitions equals the product of rates for counter-clockwise transitions [101]. (We have implicitly assumed periodic boundary conventions.) Constructing similar products for effective dynamics under a λ field (Eq. 5.13), we find that the effective dynamics obey detailed balanced if and only if

$$\prod_{i=1}^N \left(\frac{\mathbb{W}_\omega(\lambda)_{i,i+1}}{\mathbb{W}_\omega(\lambda)_{i+1,i}} \right) = 1. \quad (5.15)$$

Using the definition of $\mathbb{W}_\omega(\lambda)$, in Eq. 5.5, Eq. 5.15 can be expressed as

$$\left(\prod_{i=1}^N \frac{\mathbb{W}_{i,i+1}}{\mathbb{W}_{i+1,i}} \right)^{1-2\lambda} = 1. \quad (5.16)$$

In other words, provided $\lambda \neq 1/2$, the effective dynamics satisfy the condition of detailed balance if and only if the underlying physical dynamics are detail balanced. The result is simply extended to networks with multiple cycles using the cycle decomposition theorem [101].

Persister Cells

It has long been observed that a small fraction of a colony of genetically identical bacterial cells are resistant to antibiotic treatment [16]. One important observation is that bacteria which are not dividing are not affected by the antibiotic, which suggests that bacteria have an internal switch allowing rare transitions into non-dividing persister states that could provide protection from the antibiotic [77]. Several detailed mechanisms have been proposed for stabilizing the non-dividing persister state of the bacteria [71, 78], though these pathways have been shown to be not wholly responsible for the appearance of persister cells [117].

We note that the dynamic phase transition of our studied model presents a distinct stochastic hypothesis to explain the long timescale decay of bacterial population in response to an antibiotic. The ensemble of bacteria could be thought of as the ensemble of trajectories evolving in time around the ring, with every completed cycle corresponding to another cell division. While typical cells cycle rapidly, a rare dynamic phase of localized, non-dividing cells could be expected to exist solely because of the heterogeneity of rates around a cell cycle. Provided that antibiotics kill cells which grow rapidly, the localized subensemble of cells predicted by our calculations could result in an anomalously slow decay in survival probability. Notably, our model lacks an explicit degree of freedom capable of differentiating persister and normal states based on a single-time observation since the phases describe classes of trajectories, not of configurations.

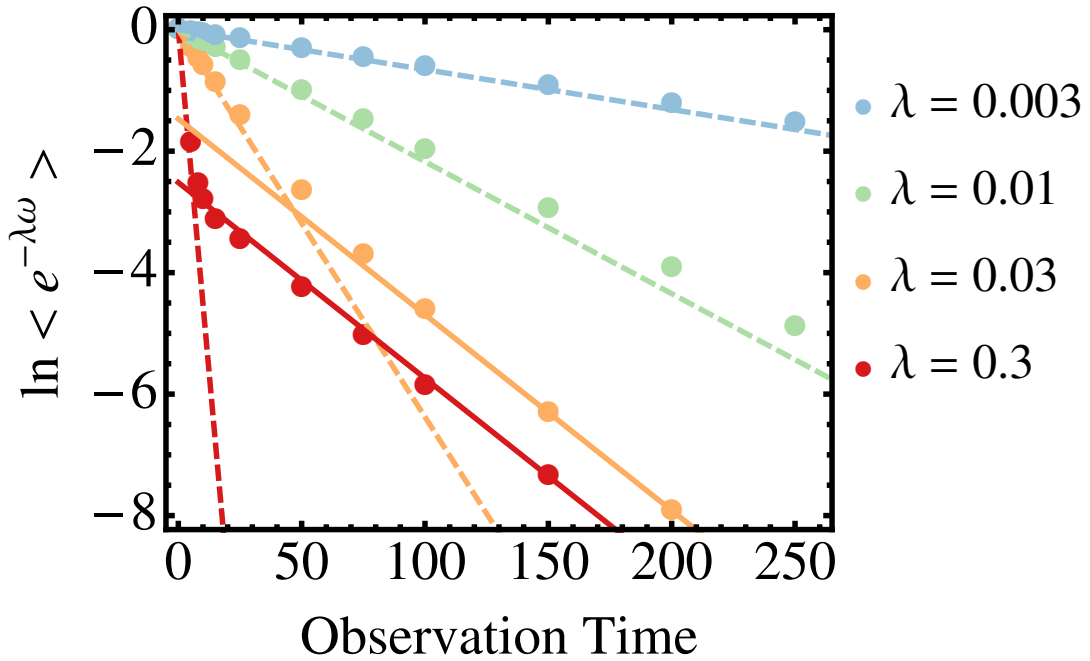


Figure 5.11: Log survival probability for trajectories killed in proportion to $e^{-\lambda\omega}$. Entropy production for 5×10^6 steady state trajectories of various observation times were collected with $x = 3, h_1 = h_2 = 0.05, N = 1000$. For this choice of rate constants, $\lambda^* \approx 0.015$. At the observation time trajectories are killed with a probability tuned by λ , which could act like the strength of an antibiotic in the case of bacterial cells. Dashed lines are lines with slope $\psi^{(ts)}(\lambda)$, which capture the short-time behavior since typical trajectories do not encounter the heterogeneity at short times. Solid lines have slope $\psi(\lambda)$ as given by Eqs. (E.1) and (E.6). As the maximum eigenvalue, $\psi(\lambda)$ must characterize the long-time behavior.

In Fig. 5.11 we use our model system to extract qualitative estimates of the survival probability of cells as a function of time in the presence of an antibiotic. In particular, we kill trajectories in proportion to $e^{-\lambda\omega}$, where ω denotes the entropy produced along the trajectory and λ controls the death rate and is meant to represent the presence of an antibiotic. At long times, the log probability of surviving trajectories decays according to $\psi_\omega(\lambda)$, which differs from the initial decay rate if $\lambda > \lambda^*$ and the dynamic phase transition can be accessed. The decay of survival probability can be expected to change markedly from single exponential to biexponential behavior at a critical value λ^* . An experimental realization of such an observation may be accessible in observing the survival probability of persister cells in response to different classes of antibiotics.

We note that the bi-exponential curves in Fig. 5.11 are similar to those observed experimentally [10] and are attained even without an internal switch that determines the cell's type. This demonstration suggests that persister cells may be a generic feature resulting from inescapable heterogeneity in transition rates, such that removing one pathway impli-

cated in supporting persisters will just reveal new localized phases centered around different heterogeneous links.

5.6 Conclusions

We have investigated the properties of a dynamic phase transition in a recently introduced exactly solvable model. Using methods of large deviation theory we analytically computed the joint rate function for the dynamical activity and entropy production rates for a single-particle system evolving on a simple driven kinetic network. The joint rate function demonstrates two dynamic phases — one localized and the other delocalized — but the marginal rate functions do not exhibit the underlying transition under all conditions. Specifically, the marginal rate function corresponding to the entropy production has a critical point beyond which there is no dynamic phase coexistence even though the system still supports two distinct classes of trajectories. We illustrated the rates that position the system in a state of coexistence between localized and delocalized phases. We also discussed a biophysical implication of the transition, namely the heterogeneity in the growth rates of bacterial cells and the phenomena of persistence, arguing that a bistability of dynamic phases can be found in even the simplest models of a cell cycle which lack an explicit bistability in configuration space.

Our study of a single-particle system reveals one simple manner in which dynamic phase transitions can arise. The two dynamic phases are time independent, a characteristic of the transition shared by some many-particle systems [17], but the model certainly does not encompass the full range of dynamical complexity intrinsic to interacting nonlinear degrees of freedom. This work thus does not directly help to clarify, for instance, rare phases related to the hydrodynamic limit of many-particle dynamics [13, 14, 18]. Nevertheless, our exact analytical results for a schematic model highlight features that could be important in much more exotic phenomena, most notably the possibility that dynamic phase transitions can be visible to some pertinent order parameters yet hidden from others.

Appendix A

Entropy Production Statistics for a One-Dimensional Random Walker with Guiding Forces

A.1 Mean Entropy Production

Here we analytically characterize the entropy production distribution, $P(\omega)$, for shooting moves generated with guiding forces as discussed in Section 2.4. It is useful to first rewrite Eq. (2.2) in terms of the noise variables, ξ and $\tilde{\xi}$. For a one-dimensional random walk, the position x_{t+1} and the difference between reference and trial trajectory, $x_{t+1} - \tilde{x}_{t+1}$, can be compactly expressed in terms of the noises.

$$x_{t+1} = \sum_{u=0}^t \xi_u \quad (\text{A.1})$$

$$x_{t+1} - \tilde{x}_{t+1} = \sum_{u=0}^t (1-k)^{t-u} (\xi_u - \tilde{\xi}_u). \quad (\text{A.2})$$

After straightforward algebra it is possible to express ω as

$$\omega = \frac{1}{\sigma^2} \sum_{t=0}^{t_{\text{obs}}-1} (S_t^2 - S_t \xi_t^+), \quad (\text{A.3})$$

where for convenience we have defined $\xi_t^+ \equiv \tilde{\xi}_t + \xi_t + 2\mu$, $\xi_t^- \equiv \tilde{\xi}_t - \xi_t$, and

$$S_t \equiv \sum_{u=0}^{t-1} k(1-k)^{t-1-u} \xi_u^-. \quad (\text{A.4})$$

The main text presents results for a random walk without drift, i.e., with ξ drawn from a distribution with mean zero. Here we consider the more general case with nonzero mean μ .

Noting that $\langle \xi_t^+ \xi_u^+ \rangle = \langle \xi_t^- \xi_u^- \rangle = 2\sigma^2 \delta_{tu}$ and $\langle \xi_t^+ \xi_u^- \rangle = 0$, the average entropy production is found to be

$$\langle \omega \rangle = 2 \sum_{t=0}^{t_{\text{obs}}-1} \sum_{u=0}^{t-1} k^2 (1-k)^{2(t-1-u)}. \quad (\text{A.5})$$

The two geometric series are summed to yield

$$\langle \omega \rangle = \frac{2}{(k-2)^2} [(2-k)kt_{\text{obs}} - 1 + (k-1)^{2t_{\text{obs}}}] . \quad (\text{A.6})$$

When $k > 2$, $\langle \omega \rangle$ grows exponentially in t_{obs} . This superlinear scaling results from coupling between trajectories so strong that the trial trajectory rapidly tends to infinity due to a numerical instability, much like the instability that arises in conventional molecular dynamics simulations performed with an excessively large integration timestep. For the useful range of coupling strength, $k < 2$, $\langle \omega \rangle \propto t_{\text{obs}}$ in the long time limit. The marginal $k = 2$ case is well-behaved ($\langle \omega \rangle = 4t_{\text{obs}}(t_{\text{obs}} - 1)$), but uninteresting for our purposes.

Cumulant Generating Function

The behavior of the higher-order cumulants can be extracted from the cumulant generating function $\ln \langle e^{-\lambda \omega} \rangle$. This average requires integration over all of the Gaussian ξ and $\tilde{\xi}$ variables at all times, which can be performed inductively. We define $\phi(\lambda, f, g, h, t)$ as

$$\begin{aligned} \phi(\lambda, f, g, h, t) &= f \left(\frac{1}{2\sigma\sqrt{\pi}} \right)^{2t} \int d\xi_0^+ \dots d\xi_{t-1}^+ d\xi_0^- \dots d\xi_{t-1}^- \exp \left[\frac{-(\xi_{t-1}^+)^2 - (\xi_{t-1}^-)^2}{4\sigma^2} \right] \\ &\times \exp \left[\frac{1}{\sigma^2} \left(\lambda (S_{t-1}\xi_{t-1}^+ - h S_{t-1}^2 + 2gk(1-k)S_{t-1}\xi_{t-1}^- + gk^2(\xi_{t-1}^-)^2) \right) \right] \\ &\times \exp \left[\frac{1}{\sigma^2} \sum_{i=0}^{t-2} \left(\frac{-(\xi_i^+)^2 - (\xi_i^-)^2}{4} + \lambda S_i \xi_i^+ - \lambda S_i^2 \right) \right] \end{aligned} \quad (\text{A.7})$$

The integral ϕ is defined such that $\langle e^{-\lambda \omega} \rangle = \phi(\lambda, 1, 0, 1, t_{\text{obs}})$. By introducing f, g , and h we can derive recursion relations as we sequentially integrate out Gaussian noises at the latest remaining timestep. In particular, integration over ξ_{t-1}^- then ξ_{t-1}^+ returns an integral of the same form. That is to say $\phi(\lambda, f_i, g_i, h_i, t) = \phi(\lambda, f_{i+1}, g_{i+1}, h_{i+1}, t-1)$ with

$$f_{i+1} = \frac{f_i}{\sqrt{1 - 4\lambda g_i k^2}} \quad (\text{A.8})$$

$$g_{i+1} = \lambda - h_i + \frac{4\lambda g_i^2 (1-k)^2 k^2}{1 - 4\lambda g_i k^2} \quad (\text{A.9})$$

$$h_{i+1} = 1 - (1-k)^2 \left((\lambda - h_i) + \frac{4\lambda g_i^2 (1-k)^2 k^2}{1 - 4\lambda g_i k^2} \right) \quad (\text{A.10})$$

Iterating the map t_{obs} times corresponds to integrating over all of the $2t_{\text{obs}}$ integrals in Eq. (A.7). After some algebraic simplification,

$$\ln \langle e^{-\lambda\omega} \rangle = -\frac{1}{2} \sum_{i=0}^{t_{\text{obs}}-1} \ln(1 - 4\lambda g_i k^2), \quad (\text{A.11})$$

where $g_0 = 0$ and

$$g_{i+1} = \lambda - 1 + \frac{(1-k)^2 g_i}{1 - 4\lambda g_i k^2}. \quad (\text{A.12})$$

The scaled cumulant generating function is then given by

$$\lim_{t_{\text{obs}} \rightarrow \infty} \frac{1}{t_{\text{obs}}} \ln \langle e^{-\lambda\omega} \rangle = -\frac{1}{2} \ln(1 - 4\lambda g^* k^2), \quad (\text{A.13})$$

where g^* is a fixed point of the map given in Eq. (A.12). Specifically it is the lesser of the two roots of the quadratic equation obtained when $g_i = g_{i+1} \equiv g^*$ is inserted into Eq. (A.12). The numerical Legendre transform of this scaled cumulant generating function gives the solid black curve in Fig. 2.2(a), toward which the results of numerical sampling should converge for long t_{obs} .

Appendix B

Ising Model Steady State Correlations

To derive the steady state correlation between reference and trial trajectories, we examine the time evolution of the probability $p(\tau)$ that reference and trial overlap at site i and MC step τ . Without loss of generality, we focus on a particular site, $i = 1$. Push up/push down moves can be grouped into four classes: (i) the reference and trial each act on spin 1, (ii) the reference acts on spin 1 while the trial acts on a different spin, (iii) the trial acts on spin 1 while the reference acts on a different spin, or (iv) neither reference nor trial acts on spin 1. For each case, we derive a transition matrix which maps the vector $(p(\tau), 1 - p(\tau))$ to its state at MC step $\tau + 1$. The full transition matrix for a step of dynamics is the sum of these transition matrices, weighted by the probability of each case,

$$\begin{aligned} T = & \left(1 - \frac{1}{N} \left(1 + \epsilon_{\text{site}} - \frac{\epsilon_{\text{site}}}{N}\right)\right) I + \frac{1}{N} \left(\epsilon_{\text{site}} - \frac{\epsilon_{\text{site}}}{N}\right) Q \\ & + \frac{1}{N} \left(\epsilon_{\text{site}} - \frac{\epsilon_{\text{site}}}{N}\right) R + \frac{1}{N} \left(1 - \epsilon_s + \frac{\epsilon_{\text{site}}}{N}\right) S. \end{aligned} \quad (\text{B.1})$$

The transition matrix for case (iv) is the identity matrix, since this case cannot alter the overlap at site 1. The transition matrices for cases (i), (ii), and (iii) are Q , R , and S , respectively, the forms of which we now derive.

When reference and trial act on different spins, only one copy of spin 1 (the reference or the trial) can change its state. When the two copies differ at site i after τ steps, overlap is induced with probability 1/4 (i.e., the probability that any given move results in a change of spin state). For initially aligned copies, loss of overlap similarly occurs with probability 1/4. This logic applies equally well to cases (ii) and (iii), so

$$Q = R = \begin{pmatrix} 3/4 & 1/4 \\ 1/4 & 3/4 \end{pmatrix}. \quad (\text{B.2})$$

When both reference and trial act on site 1, we must account for correlated influence on the two copies. As a result, S depends on ϵ_{acc} and ϵ_{dir} . To enumerate these correlated changes, we denote states of spin 1 at step τ in the reference and trial as σ_1 and $\tilde{\sigma}_1$, respectively. After

σ	d	a	σ'	$\tilde{\sigma}$	\tilde{d}	\tilde{a}	$\tilde{\sigma}'$	Probability
1	1	*	1	1	1	*	1	$\frac{p}{2} \left(1 - \frac{\epsilon_{\text{dir}}}{2}\right)$
1	1	*	1	1	-1	0	1	$\frac{\epsilon_{\text{dir}} p}{8}$
1	1	*	1	-1	1	1	1	$\frac{1-p}{4} \left(1 - \frac{\epsilon_{\text{dir}}}{2}\right)$
1	-1	0	1	1	1	*	1	$\frac{\epsilon_{\text{dir}} p}{8}$
1	-1	0	1	1	-1	0	1	$\frac{p}{4} \left(1 - \frac{\epsilon_{\text{dir}}}{2}\right) \left(1 - \frac{\epsilon_{\text{acc}}}{2}\right)$
1	-1	0	1	-1	1	1	1	$\frac{1-p}{4} \left(\frac{\epsilon_{\text{dir}}}{2}\right) \left(\frac{\epsilon_{\text{acc}}}{2}\right)$
1	-1	1	-1	1	-1	1	-1	$\frac{p}{4} \left(1 - \frac{\epsilon_{\text{dir}}}{2}\right) \left(1 - \frac{\epsilon_{\text{acc}}}{2}\right)$
1	-1	1	-1	-1	1	0	-1	$\frac{1-p}{4} \left(\frac{\epsilon_{\text{dir}}}{2}\right) \left(\frac{\epsilon_{\text{acc}}}{2}\right)$
1	-1	1	-1	-1	-1	*	-1	$\frac{1-p}{4} \left(1 - \frac{\epsilon_{\text{dir}}}{2}\right)$

Table B.1: Enumeration of moves yielding $\sigma' = \tilde{\sigma}'$. Without loss of generality, we only list the moves which start with $\sigma = 1$. The moves starting with $\sigma = -1$ are analogous. d is the direction of a push with 1 meaning up. a indicates whether the move is accepted (1) or rejected (0). An asterisk indicates that both options yield the same result.

the MC step, these spins are given by σ'_1 and $\tilde{\sigma}'_1$. Table B.1 lists the possible transformations which result in overlapping spins ($\sigma'_1 = \tilde{\sigma}'_1$) after $\tau + 1$ steps. Collecting terms in the table and making use of the fact that S is a probability-conserving transition matrix, we find

$$S = \frac{1}{2} \begin{pmatrix} 1 + \left(1 - \frac{\epsilon_{\text{dir}}}{2}\right) \left(1 - \frac{\epsilon_{\text{acc}}}{2}\right) & 1 - \frac{\epsilon_{\text{dir}}}{2} \left(1 - \frac{\epsilon_{\text{acc}}}{2}\right) \\ 1 - \left(1 - \frac{\epsilon_{\text{dir}}}{2}\right) \left(1 - \frac{\epsilon_{\text{acc}}}{2}\right) & 1 + \frac{\epsilon_{\text{dir}}}{2} \left(1 - \frac{\epsilon_{\text{acc}}}{2}\right) \end{pmatrix}. \quad (\text{B.3})$$

Propagation according to the transition matrix T gives the overlap probability after a single MC step:

$$\begin{pmatrix} p(\tau+1) \\ 1 - p(\tau+1) \end{pmatrix} = T \begin{pmatrix} p(\tau) \\ 1 - p(\tau) \end{pmatrix} \quad (\text{B.4})$$

The first row of this matrix equation reads, after some algebra,

$$p(\tau+1) = p(\tau) - \frac{p(\tau)}{N} + \frac{\epsilon_{\text{site}} - \frac{\epsilon_{\text{site}}}{N}}{2N} + \frac{1 - \epsilon_{\text{site}} + \frac{\epsilon_{\text{site}}}{N}}{2N} \left[1 - \frac{\epsilon_{\text{dir}}}{2} \left(1 - \frac{\epsilon_{\text{acc}}}{2}\right) + \left(1 - \frac{\epsilon_{\text{acc}}}{2}\right) p(\tau) \right]. \quad (\text{B.5})$$

We are interested in the steady state solution, found by setting $p(\tau) = p(\tau+1)$. Multiplying the equation through by N , followed by algebraic simplification, yields Eq. 2.25 of the main text.

Appendix C

Extended Ensemble Double Well Transition Path Sampling

We sample the extended ensemble over trajectories and protocols from Eq. (3.6) using TPS. An initial seed is obtained by starting a trajectory at the top of the barrier and propagating dynamics forward and backward in time. The equations of motion for the discrete forward-time dynamics are given in the main text. Reverse-time dynamics is generated according to

$$\begin{aligned} p_{i+\frac{1}{2}} &= \left[p_i e^{-\gamma \Delta t/2} - \xi_{i+\frac{3}{4}}^- \right] - f_{i+1} \frac{b \Delta t}{2} \\ r_i &= r_{i+1} - p_{i+\frac{1}{2}} \frac{b \Delta t}{m} \\ p_i &= \left[p_{i+\frac{1}{2}} - f_i \frac{b \Delta t}{2} \right] e^{-\gamma \Delta t/2} - \xi_{i+\frac{1}{4}}^-. \end{aligned} \quad (\text{C.1})$$

Because trajectories can be generated by either forward or reversed trajectories, it is useful to always keep track of the two forward noises required for each full timestep, $\xi_{i+\frac{1}{4}}^+$ and $\xi_{i+\frac{3}{4}}^+$, as well as the two backward noises, $\xi_{i+\frac{1}{4}}^-$ and $\xi_{i+\frac{3}{4}}^-$. After every simulated forward timestep from (r_i, p_i) to (r_{i+1}, p_{i+1}) , we compute and store the two reverse noises that result in reversed dynamics mapping (r_{i+1}, p_{i+1}) to (r_i, p_i) . Similarly, the forward noises are computed and recorded following every reversed timestep. It is straightforward to show that the ratio of probabilities of forward and reverse trajectories is given in terms of these noises as

$$\frac{P[x(t)|\Omega]}{P[\hat{x}(t)|\hat{\Omega}]} = \exp \left(-\frac{\beta \sum_{i=0}^{\frac{t_{\text{obs}}}{\Delta t}-1} \left(|\xi_{i+\frac{1}{4}}^+|^2 + |\xi_{i+\frac{3}{4}}^+|^2 - |\xi_{i+\frac{1}{4}}^-|^2 - |\xi_{i+\frac{3}{4}}^-|^2 \right)}{2m(1 - e^{-\gamma \Delta t})} + \beta \Delta E \right), \quad (\text{C.2})$$

where we use $x(t)$ to denote a trajectory in phase space, $(r(t), p(t))$. The difference in energies at the initial and final times of the trajectory, $\Delta E = E_{t_{\text{obs}}} - E_0$, appears because we assume that the system starts in thermal equilibrium at the beginning of the protocol. We identify the entropy production as

$$\omega = \ln \frac{P[x(t)|\Omega]}{P[\hat{x}(t)|\hat{\Omega}]} = -\frac{\beta}{2m(1-e^{-\gamma\Delta t})} \sum_{i=0}^{\frac{t_{\text{obs}}}{\Delta t}-1} \left(\left| \xi_{i+\frac{1}{4}}^+ \right|^2 + \left| \xi_{i+\frac{3}{4}}^+ \right|^2 - \left| \xi_{i+\frac{1}{4}}^- \right|^2 - \left| \xi_{i+\frac{3}{4}}^- \right|^2 \right) + \beta\Delta E. \quad (\text{C.3})$$

The extended ensemble sampling proceeds by a series of Monte Carlo moves in trajectory and protocol space. With equal probability, each TPS step performs one of three possible MC moves: a forward shot, a reverse shot, or a protocol move (which requires us to simultaneously update the trajectory). These moves and their acceptance probabilities are described in detail in the following sections.

Forward Shot

A timestep between 0 and $t_{\text{obs}}/\Delta t$ is selected uniformly and designated the shooting time. Starting at the shooting time, each value of $\xi_{i+\frac{1}{4}}^+$ and $\xi_{i+\frac{3}{4}}^+$ is modified to give new values $\tilde{\xi}_{i+\frac{1}{4}}^+$ and $\tilde{\xi}_{i+\frac{3}{4}}^+$,

$$\tilde{\xi}^+ = \alpha\xi^+ + \sqrt{1-\alpha^2}\eta. \quad (\text{C.4})$$

The parameter α controls the noise correlations, and η is drawn from the Gaussian distribution with mean 0 and variance $mk_B T(1 - e^{-\gamma\Delta t})$. Using these new noises, forward dynamics is propagated as prescribed by Eqs. (3.3) (and the corresponding reverse noises are stored). Provided the final timestep ends in region B, the new trajectory is accepted.

Reverse Shot

A random shooting time is selected as in the forward shot, and correlated reverse noises are generated for all times leading up to the shooting time,

$$\tilde{\xi}^- = \alpha\xi^- + \sqrt{1-\alpha^2}\eta. \quad (\text{C.5})$$

We draw η from the same distribution as in the forward shot. Using the new reverse noises, we propagate from the shooting time backward in time using Eqs. C.1. For this trial trajectory to be accepted it must, of course, start in region A, but we also must include a reweighting factor in the acceptance probability. This reweighting is needed because the trial trajectory, $\tilde{x}(t)$, was generated from a time-reversed protocol while its contribution to the equilibrium path probability refers to the forward-time protocol. The acceptance for the move can be written as

$$P_{\text{accept}}[x(t) \rightarrow \tilde{x}(t)] = \min \left[1, \frac{P_{\text{extended}}[x(t)|\Omega] P_{\text{gen.}}[x(t) \rightarrow \tilde{x}(t)]}{P_{\text{extended}}[\tilde{x}(t)|\Omega] P_{\text{gen.}}[\tilde{x}(t) \rightarrow x(t)]} \right]. \quad (\text{C.6})$$

The generation of $\tilde{x}(t)$ from $x(t)$ can be viewed as a three-stage procedure. First we take the time reversal of $r(t)$ to get $\hat{r}(t)$. Then we draw values of η to alter the reverse noises and convert $\hat{x}(t)$ to $\tilde{x}(t)$, a new reverse-time trajectory. Finally, we apply the time-reversal operator again to get $\tilde{x}(t)$. Thus we can rewrite the ratio in Eq. (C.6) as

$$\begin{aligned} \frac{P_{\text{gen.}}[x(t) \rightarrow \tilde{x}(t)]}{P_{\text{gen.}}[\tilde{x}(t) \rightarrow x(t)]} &= \frac{P_{\text{gen.}}[x(t) \rightarrow \hat{x}(t)] P_{\text{gen.}}[\hat{x}(t) \rightarrow \tilde{x}(t)] P_{\text{gen.}}[\tilde{x}(t) \rightarrow \tilde{x}(t)]}{P_{\text{gen.}}[\tilde{x}(t) \rightarrow \hat{x}(t)] P_{\text{gen.}}[\hat{x}(t) \rightarrow \hat{x}(t)] P_{\text{gen.}}[\hat{x}(t) \rightarrow x(t)]} \\ &= \frac{P_{\text{gen.}}[\hat{x}(t) \rightarrow \tilde{x}(t)]}{P_{\text{gen.}}[\tilde{x}(t) \rightarrow \hat{x}(t)]} \\ &= \frac{P_{\text{extended}}[\tilde{x}(t) | \hat{\Omega}]}{P_{\text{extended}}[\hat{x}(t) | \hat{\Omega}]} . \end{aligned} \quad (\text{C.7})$$

The first step uses the fact that the time-reversal operator is reversible. The second step is a consequence of noise-guided reverse dynamics generating unbiased samples from the reversed protocol ensemble. In other words,

$$\frac{P_{\text{extended}}[\hat{x}(t) | \hat{\Omega}] P_{\text{gen.}}[\hat{x}(t) \rightarrow \tilde{x}(t)]}{P_{\text{extended}}[\tilde{x}(t) | \hat{\Omega}] P_{\text{gen.}}[\tilde{x}(t) \rightarrow \hat{x}(t)]} = 1, \quad (\text{C.8})$$

which follows by the same logic that led to Eq. (2.21). Substituting Eq. (C.7) into Eq. (C.6) and rewriting the ratio of forward and reversed trajectories in terms of the entropy production ω of trajectory $x(t)$ and the entropy production $\tilde{\omega}$ of the trial trajectory $\tilde{x}(t)$, we are left with

$$P_{\text{accept}}[x(t) \rightarrow \tilde{x}(t)] = \min[1, h_A(\tilde{x}_0) e^{\tilde{\omega} - \omega}]. \quad (\text{C.9})$$

Protocol Move

The driving frequency Ω is perturbed by a symmetric Monte Carlo move. A trial frequency, $\tilde{\Omega}$ is chosen by adding to the old Ω a small perturbation, drawn uniformly from the interval $[-\delta, \delta]$ for some parameter δ . With this new driving frequency, the initial condition of the old trajectory, x_0 , is re-propagated forward with $x(t)$'s identical noise history. The proposed change to Ω is accepted if the new trajectory ends in region B,

$$P_{\text{accept}}[\Omega, x(t) \rightarrow \tilde{\Omega} \tilde{x}(t)] = \min \left[1, h_B(\tilde{x}_{t_{\text{obs}/\Delta t}}) \right]. \quad (\text{C.10})$$

In practice, it is typically necessary to allow Ω to only explore a bounded interval, in which case the move would also be rejected if $\tilde{\Omega}$ lies outside the allowed range. It can also be useful to restrain Ω to sample near some particular value of frequency, Ω_c , by accepting moves with probability

$$P_{\text{accept}}[\Omega, x(t) \rightarrow \tilde{\Omega} \tilde{x}(t)] = \min \left[1, h_B(\tilde{x}_{t_{\text{obs}/\Delta t}}) e^{-k(\Omega - \Omega_c)^2/2} \right]. \quad (\text{C.11})$$

We call Ω_c the center and k the curvature of the “umbrella sampling” bias, which enables importance sampling, as used to generate Figs. 3.6 and 3.7.

Appendix D

Path and Protocol Sampling for the Ising Model

Efficient path sampling of the Ising model was presented in Section 2.5. There, we introduced a scheme for symmetrically perturbing the random numbers (the “noises”) which are used to propagate Monte Carlo dynamics. We work with the same push up/push down Glauber dynamics in this appendix, but we present an alternative way to perturb the noises for TPS moves. For certain applications, like the Ising spin flips studied in Chapter 3, the TPS moves detailed here have proven more effective for path sampling.

D.1 Ising Dynamics and Dissipation

Let us first review the push up/push down dynamics. Each step of the dynamics depends on the state of three noise variables, ξ_{site}^+ , ξ_{dir}^+ , and ξ_{acc}^+ . The superscript + indicates that the noises are associated with a “forward-time” MC dynamics, as implicit in Chapter 2. An explicit distinction is necessary here since we will shortly introduce a corresponding “reversed-time” MC dynamics. A dynamical step consists of four substeps:

1. Choose spin $i = \text{ceiling}(\xi_{\text{site}}^+ N)$ to modify.
2. Construct a trial state by setting spin i equal to 1 if $\xi_{\text{dir}}^+ > 0.5$ and -1 otherwise.
3. Compute $\Delta(\beta E)$, the difference in reduced energy between the original configuration and the trial.
4. Accept the spin flip if $\xi_{\text{acc}}^+ < (1 + \exp(\Delta(\beta E)))^{-1}$.

As in Chapter 2, N is the number of lattice sites and β is the inverse temperature. When each of the noise variables is drawn from a uniform distribution on $[0, 1]$ at every timestep, the resulting spins evolve under natural dynamics. The temperature T and magnetic field h can be tuned as functions of time, and their effect naturally enters into the calculation of

$\Delta(\beta E)$. We write $P_0[\sigma(t), T(t), h(t)]$ for the probability distribution generated by natural dynamics which is subject to the protocol defined by $T(t)$ and $h(t)$, and we sometimes refer to this as the probability of trajectory $\sigma(t)$ in the forward direction.

Note that any forward trajectory can be obtained by many different noise histories. To see this most clearly, consider a single timestep of the forward dynamics. Without loss of generality, let us assume that ξ_{site}^+ lies on $[0, 1/N]$, so we choose to act on spin 1. This noise could be any value on that interval without affecting the behavior of the trajectory. Similar logic can be applied to both ξ_{dir}^+ and ξ_{acc}^+ . For any possible MC step, say a step that pushes spin 1 up and accepts the spin flip, the probability of carrying out the step is the product of the sizes of the intervals from which the three ξ^+ variables could have been drawn to induce the outcome. This probability, when multiplied over all steps, yields the total probability that a trajectory will propagate from its initial to final state.

To compute the dissipation, it is necessary to also define a reverse dynamics, which propagates a trajectory $\sigma(t)$ backwards in time. This reverse dynamics applies the time-reversed protocol, but otherwise proceeds via the same four substeps as the forward dynamics: pick a spin, push the spin up or down, compute the energy change, conditionally accept. At every timestep, we must compute the probability that a forward move will be exactly undone. If the forward move chose spin i , that means the reverse move must also choose spin i . A forward move that pushes spin i up, however, must be paired with a reverse move which attempts to push it down. In both of these cases, the probability of the selection in the forward direction exactly equals the necessary time-reversed selection; the probability of picking every site is equal and the probability of picking either direction is $1/2$. The forward and reversed probabilities differ, however, since the spin flip in substep 4 will be more likely to proceed one direction than the other. If $\Delta(\beta E)$ is the entropy produced by a forward step, then the relative probability of the forward to reverse step will be $e^{-\Delta(\beta E)}$. Thus the dissipation can be computed as

$$\omega = \ln \frac{\rho_{\text{ss}}(\sigma_0, T_0, h_0)}{\rho_{\text{ss}}(\sigma_{t_{\text{obs}}}, T_{t_{\text{obs}}}, h_{t_{\text{obs}}})} - \sum_{i=1}^{Nt_{\text{obs}}} \left(\frac{E\left(\frac{i}{N}\right)}{T\left(\frac{i}{N}\right)} - \frac{E\left(\frac{i-1}{N}\right)}{T\left(\frac{i-1}{N}\right)} \right). \quad (\text{D.1})$$

$E(t)$ is the energy of the Ising lattice at time t , where the unit of time is taken to be a MC sweep consisting of N MC moves. Note that when $T(t)$ and $h(t)$ are constant in time and ρ_{ss} is taken to be the Boltzmann distribution, $\omega = 0$.

We have shown how to relate the probability of forward and reverse trajectories in Ising dynamics, but it is convenient to also introduce a noise history that realizes the reverse-time trajectories. This noise history, consisting of ξ_{site}^- , ξ_{dir}^- , and ξ_{acc}^- at every MC step, enables reverse-shooting TPS moves. We give an algorithm for generating these reversed-time noises that appears slightly complicated, but can be understood simply. Every time a forward step is taken, a reverse noise is drawn which will undo that step. That way we can carry out MC dynamics in the reversed-time direction using those reversed-time noises. We can incorporate the generation of the ξ^- 's into every forward MC step as follows:

1. Choose spin $i = \text{ceiling}(\xi_{\text{site}}^+ N)$ to modify.

2. Draw ξ_{site}^- uniformly from $[(i-1)/N, i/N]$.
3. Construct a trial state by setting spin i equal to 1 if $\xi_{\text{dir}}^+ > 0.5$ and -1 otherwise.
4. If the trial move does not alter the state of spin i , i.e., pushing up a spin that's already up or pushing down a spin that's already down:
 - (a) Choose $\xi_{\text{dir}}^- = \xi_{\text{dir}}^+$.
 - (b) Choose ξ_{acc}^- uniformly from $[0, 1]$.
 - (c) Advance to the next timestep because the move does not alter spin i .
4. Compute $\Delta(\beta E)$, the difference in reduced energy between the original configuration and the trial.
5. Accept the spin flip if $\xi_{\text{acc}}^+ < (1 + \exp(\Delta(\beta E)))^{-1}$.
6. Select ξ_{dir}^- uniformly from $[0, 0.5]$ if spin i ended in the up state. Otherwise select uniformly from $[0.5, 1]$.
7. If the forward move was an accepted spin flip, uniformly select ξ_{acc}^- from $[0, (1 + e^{-\Delta(\beta E)})^{-1}]$. Otherwise select from $[(1 + e^{\Delta(\beta E)})^{-1}, 1]$.

The reversed time dynamics follows the same 7 substeps except that each ξ^+ is replaced by the corresponding ξ^- and the time reversed protocol is applied.

D.2 Path Sampling

Path sampling is performed by a series of shooting-like moves, which first symmetrically perturb the noise history then re-propagate MC dynamics in the forward or reversed direction. Here we detail the moves and derive the acceptance probabilities necessary to sample the trajectory space with a dissipation bias,

$$P_\lambda[\sigma(t), \Lambda(t)] \propto P_0[\sigma(t)|\Lambda(t)] e^{-\lambda\omega[\sigma(t), T(t), h(t)]} \quad (\text{D.2})$$

Noise Perturbations

In Chapter 2 we discussed one particular way to perturb the noise history in a symmetric manner. At every time step, we reused the old value of noise with probability $1 - \epsilon$ and otherwise uniformly drew new noise from $[0, 1]$. The parameter ϵ could be tuned to adjust the strength of correlations. We call this noise perturbation symmetric because $P(\xi \rightarrow \tilde{\xi}) = P(\tilde{\xi} \rightarrow \xi)$, where $\tilde{\xi}$ is the noise variable for a trial MC move as in the main text. Because the noises sample a uniform distribution, this symmetric generation probability is equivalent to obeying the principle of detailed balance in noise space,

$$P(\xi)P(\xi \rightarrow \tilde{\xi}) = P(\tilde{\xi})P(\tilde{\xi} \rightarrow \xi). \quad (\text{D.3})$$

In Chapter 3 we employ a different, but also symmetric, noise perturbation scheme. Before evolving some forward (backwards) MC dynamics, one of three noise perturbations is applied with equal probability to alter the forward (backwards) noises starting from a shooting time and passing to the end (beginning) of the trajectory.

1. All values of ξ_{site} , ξ_{dir} , and ξ_{acc} are uniformly resampled from the unit interval.
2. At each MC timestep the value of ξ_{site} is uniformly resampled from $[0, 1]$ with probability ϵ_{site} .
3. At each MC timestep, the value of ξ_{acc} performs a random walk on the unit interval with periodic boundary conditions. Each attempted step in ξ_{acc} is uniformly chosen from $[-\epsilon_{\text{acc}}, \epsilon_{\text{acc}}]$.

These schemes are sufficient to ensure ergodicity in noise space, but by selecting small values of ϵ_{site} and ϵ_{acc} , strong noise correlations can be maintained.

Shooting Moves

Shooting moves update all or part of a trajectory by re-evolving dynamics with a noise history which is highly correlated with the previous trajectory. We retain forward and reverse noise histories for all trajectories, regardless of whether the trajectory was initially generated via forward or reversed dynamics. Thus we can slightly perturb the reversed noises when attempting to re-propagate dynamics in the time-reversed direction, and we can perturb the forward noises when attempting to re-propagate dynamics in the forward direction.

Forward Shots

A time between 0 and t_{obs} is selected uniformly and designated the shooting time. From this shooting time, the forward noises are symmetrically perturbed as described above, and the push up/push down dynamics is propagated until the end of the trajectory to give a trial trajectory, $\tilde{\sigma}(t)$. It is straightforward to show that to sample the distribution in Eq. (D.2), the acceptance rate for forward shooting moves must be

$$P_{\text{acc}}[\sigma(t) \rightarrow \tilde{\sigma}(t)] = \min [1, e^{-\lambda(\tilde{\omega} - \omega)}], \quad (\text{D.4})$$

where ω is the dissipation of the old trajectory and $\tilde{\omega}$ is the dissipation of the new.

Reverse Shots

A time between 0 and t_{obs} is selected uniformly and designated the shooting time. From this shooting time, the reverse noises are symmetrically perturbed as described above, and the push up/push down dynamics is propagated backwards in time until time 0 to give $\hat{\sigma}(t)$. The

time reversal of this trajectory, $\tilde{\sigma}(t)$, is the trial trajectory for the reverse shooting move, which is accepted with probability

$$P_{\text{acc}}[\sigma(t) \rightarrow \tilde{\sigma}(t)] = \min [1, e^{(1-\lambda)(\tilde{\omega}-\omega)}]. \quad (\text{D.5})$$

Because we generated $\tilde{\sigma}(t)$ from the reverse-time dynamics but we want the probability of the forward-time trajectory $\tilde{\sigma}(t)$, the acceptance probability acquires an additional factor of $e^{\tilde{\omega}-\omega}$, which was absent in the forward shooting move acceptance probability, Eq. (D.4). This extra factor can be derived following the same steps that led to Eq. (C.9).

Crooks Shot

The Crooks shooting move [31] is a forward shooting move which re-propagates dynamics starting from time 0 but using a different initial condition. A distinct initial condition is generated with ordinary equilibrium Ising dynamics using the temperature T_0 and field h_0 of the initial time. This new initial condition is propagated forward in time using a correlated noise history, precisely as in a forward shooting move. Resampling the initial condition does not affect the acceptance probability, so like the forward shooting move, the Crooks shooting move is accepted with probability

$$P_{\text{acc}}[\sigma(t) \rightarrow \tilde{\sigma}(t)] = \min [1, e^{-\lambda(\tilde{\omega}-\omega)}]. \quad (\text{D.6})$$

D.3 Protocol Sampling

The values at the protocol at the initial and final times are held fixed, but Monte Carlo moves modify the protocol at all other times to sample the protocol space. To prevent protocols which ramp the temperature or magnetic field too rapidly, we further constrain the protocols to those which are piecewise linear with nine linear segments. In other words, we parametrize the protocol space by its value at ten evenly spaced times from 0 to t_{obs} . We call these times the control points. The full protocol $\Lambda(t)$ is obtained by linearly extrapolating between control points.

A Monte Carlo move uniformly selects one of the eight interior control point (the first and last control point are fixed) and tries to symmetrically modify either the temperature or the magnetic field by adding a uniform random number drawn from the interval $[-\delta, \delta]$, with δ a parameter affecting the size of jumps in protocol space. If the modification exits the allowed range of protocols (for example the temperature is made negative), then the move is rejected. Otherwise the full trial protocol $\tilde{\Lambda}(t)$ is constructed by generating piecewise linear T and h which pass through the modified control point. We can propose and conditionally accept the protocol move $\Lambda(t) \rightarrow \tilde{\Lambda}(t)$ so as to sample the distribution in Eq. (D.2), but the acceptance probability will involve computing $P_0[\sigma(t)|\tilde{\Lambda}(t)]$. In words, this is the probability of generating the old trajectory, given the new protocol. Typically, this conditional probability will be very small, so it is more efficient to update the protocol in concert with

the trajectory, proposing $\{\sigma(t), \Lambda(t)\} \rightarrow \{\tilde{\sigma}(t), \tilde{\Lambda}(t)\}$. The trial protocol is generated as previously described, and the trial trajectory is obtained with a forward shooting move from the initial timestep, using the new protocol to propagate dynamics. More explicitly, $\tilde{\sigma}_0$ is set to σ_0 then $\tilde{\sigma}(t)$ is generated using $\sigma(t)$'s noise history (or a noise history symmetrically perturbed about it). With this construction,

$$P_{\text{acc}}[\{\sigma(t), \Lambda(t)\} \rightarrow \{\tilde{\sigma}(t), \tilde{\Lambda}(t)\}] = \min \left[1, e^{-\lambda(\tilde{\omega} - \omega)} \right]. \quad (\text{D.7})$$

Appendix E

Ring Network with Heterogeneity Scaled Cumulant Generating Function

Were it not for the heterogeneous link connecting sites 1 and N , the tilted operator would have a translational symmetry, making its explicit diagonalization trivial in a Fourier basis. We construct a $1/N$ expansion of $\psi_{\omega,K}(\lambda, s)$ by expanding around the maximum eigenvalue of the translationally symmetric network,

$$\psi_{\omega,K}(\lambda, s) = x^{1-\lambda}e^{-s} + x^{\lambda}e^{-s} - 1 - x + \frac{\gamma e^{-s}(x^{\lambda} - x^{1-\lambda})}{N} + \dots, \quad (\text{E.1})$$

Recall from the main text that we write the elements of the maximal eigenvector as (f_1, f_2, \dots, f_N) and

$$\begin{pmatrix} f_i \\ f_{i+1} \end{pmatrix} = \begin{pmatrix} \frac{\psi+1+x}{e^{-s}x^{1-\lambda}} & -x^{2\lambda-1} \\ 1 & 0 \end{pmatrix} \begin{pmatrix} f_{i+1} \\ f_{i+2} \end{pmatrix} = B \begin{pmatrix} f_{i+1} \\ f_{i+2} \end{pmatrix}. \quad (\text{E.2})$$

Because of the translational symmetry of the network, the same transition matrix B relates almost all pairs of neighboring f_i 's. The heterogeneous link requires that we also introduce transfer matrices A_1 and A_2 given by

$$\begin{aligned} A_1 &= \begin{pmatrix} \frac{\psi+x+h_2}{e^{-s}h_1^{1-\lambda}h_2^{\lambda}} & -\frac{x^{\lambda}}{h_1^{1-\lambda}h_2^{\lambda}} \\ 1 & 0 \end{pmatrix} \\ A_2 &= \begin{pmatrix} \frac{\psi+h_1+1}{e^{-s}x^{1-\lambda}} & -\frac{h_1^{\lambda}h_2^{1-\lambda}}{x^{1-\lambda}} \\ 1 & 0 \end{pmatrix}. \end{aligned} \quad (\text{E.3})$$

Because the network is arranged in a ring, propagations around the full loop must map (f_1, f_2) onto itself, such that the transfer matrices must satisfy the boundary condition

$$B^{N-2}A_2A_1 \begin{pmatrix} f_1 \\ f_2 \end{pmatrix} = \begin{pmatrix} f_1 \\ f_2 \end{pmatrix}, \quad (\text{E.4})$$

which requires that $B^{N-2}A_2A_1$ posses a unit eigenvalue in the $N \rightarrow \infty$ limit. We use this condition to determine the $1/N$ expansion coefficient γ as a function of λ and s . Since $\psi_{\omega,K}(\lambda, s) = \psi_{\omega,K}(1 - \lambda, s)$ we focus on the case $x > 1$ and $\lambda < 1/2$ without loss of generality. It is convenient to write B in its eigenbasis after inserting the $1/N$ expansion of Eq. (E.1) where only the larger of the two eigenvalues will survive the large N limit,

$$\lim_{N \rightarrow \infty} B^{N-2} = \frac{e^{-\gamma}}{1 - x^{2\lambda-1}} \begin{pmatrix} 1 & -x^{2\lambda-1} \\ 1 & -x^{2\lambda-1} \end{pmatrix} \quad (\text{E.5})$$

Since we are interested in the large N behavior and there is only a single term of A_1 and A_2 in the product, we can comfortably neglect the $1/N$ term in the A matrices. The condition that $B^{N-2}A_2A_1$ has a unit eigenvalue requires

$$\gamma = \ln \left[\frac{x^{2(1-\lambda)} + (-h_1 h_2 + e^{2s}(h_2 - 1)(h_1 - x)) + e^s(h_1 + h_2 - 1 - x)x^{1-\lambda}}{h_1^{1-\lambda} h_2^\lambda (x^{1-\lambda} - x^\lambda)} \right] \quad (\text{E.6})$$

Note that γ diverges when the numerator of the argument of the logarithm has a root, in which case $\psi_{\omega,K}(\lambda, s)$ departs significantly from the corresponding value in the translationally symmetric network. The values of λ and s for which γ first diverges provides the line of cusps given in Eq. (5.7) of the main text. As shown in the main text, the value of $\psi_{\omega,K}(\lambda, s)$ everywhere follows. When γ does not diverge, the large N behavior coincides with the translationally symmetric result. Otherwise the behavior can be determined from the behavior of that translationally symmetric result along the curve $s^*(\lambda)$.

Appendix F

Analytical Treatment of the Triangle Network

Based on the numerical results for the triangle network, we anticipate that the same structure of delocalized and localized states will exist in the triangle network. To see this we construct the delocalized state from the solution to the translationally symmetric network and we construct the localized state using an ansatz that the eigenvector have bound state character as in the ring network. With this ansatz the form for $\psi_\omega(\lambda)$ can be reduced to the solution to a nonlinear system of two equations and two unknowns that can be rapidly solved numerically.

Translationally Symmetric Network

In the case of the triangle network with translationally symmetry, $\mathbb{W}_\omega(\lambda)$ can be exactly diagonalized by a discrete Fourier transform. If we number the sites in a zigzag fashion around the chain such that odd sites fall on the base of the triangles and even sites are at the points, then the right eigenvector takes the form

$$|q\rangle = (1, v, e^{2q\pi i/N}, ve^{2q\pi i/N}, e^{4q\pi i/N}, \dots, ve^{2q\pi(N-1)i/N}).$$

The constant factor v , which must be solved for, accounts for the fact that the odd and even sites are not identical by symmetry. The $q = 0$ eigenvalue is simple to compute, yielding the scaled cumulant generating function for the translationally symmetric triangle network,

$$\psi_\omega^{\Delta\text{ts}}(\lambda) = \frac{1}{2} \left(-2 - x - y + \sqrt{(x-y)^2 + 4(1+x^\lambda y^{1-\lambda})(1+x^{1-\lambda} y^\lambda)} \right). \quad (\text{F.1})$$

The Δ symbol indicates that this function is for the triangle network, and the ts indicates the translationally symmetric network. Interestingly, the rate b does not appear and therefore cannot influence the distribution of entropy production rates in this network. This is true even in the limit that b so large that the most likely pathways tend to flow along the b links while avoiding the triangular excursions.

Localized State Ansatz

In the thorough study of the ring network we saw that the introduction of a symmetry-breaking h link induces a transition between a delocalized and localized state. The delocalized state has a right eigenvector whose components have roughly equal magnitudes all the way around the ring. Indeed, in the large N limit we saw that this delocalized state converges to the solution for the translationally symmetric network. In addition to the delocalized state there is a localized one, whose right eigenvector has components that exponentially decay as a function of distance from the h link. This was shown formally with transfer matrices for the ring network, but for the more complicated triangle network we can just introduce this structure as an ansatz. We therefore anticipate a cusp at some value λ^* where $\psi^{\Delta_{\text{ts}}}$ must crossover the eigenvalue of a bound state, $\psi^{\Delta_{\text{b}}}$.

Because the rates are chosen to drive net flows clockwise, the exponential decays are generally not equal in opposite directions from the h link. We can introduce these decays by the constants c_1 and c_2 with the ansatz that the right eigenvector of $\mathbb{W}_\omega(\lambda)$ take the form

$$v = \left[\begin{pmatrix} c_1 \\ v_1 c_1 \\ c_1^2 \\ v_1 c_1^2 \\ \vdots \\ c_1^N \\ v_1 c_1^N \\ c_1^{N+1} \end{pmatrix} + a \begin{pmatrix} c_2^{N+1} \\ v_2 c_2^N \\ c_2^N \\ v_2 c_2^{N-1} \\ \vdots \\ c_2^2 \\ v_2 c_2 \\ c_2 \end{pmatrix} \right] \quad (\text{F.2})$$

The additional constants, v_1 and v_2 , are necessary because even and odd sites are not related by symmetry. The eigenvalue relation, $\mathbb{W}_\omega(\lambda)v = \psi_\omega^{\Delta_{\text{b}}}(\lambda)v$, gives a system of $N+1$ equations with 6 unknown parameters, a, v_1, v_2, c_1, c_2 , and $\psi_\omega^{\Delta_{\text{b}}}$. In the $N \rightarrow \infty$ limit we can neglect c_1^N and c_2^N since the c 's are less than one. We choose six of the equations in the eigenvalue relation to yield a messy, but fully determined, system,

$$\begin{cases} c_1 \psi^{\Delta_{\text{b}}} &= bc_1^2 - c_1(1+b+h) + ac_2h + c_1v_1 \\ c_1 v_1 \psi^{\Delta_{\text{b}}} &= c_1 - c_1 v_1(1+x) + c_1^2 x^\lambda y^{1-\lambda} \\ c_1^2 \psi^{\Delta_{\text{b}}} &= bc_1^3 + bc_1 + c_1^2 v_1 - c_1^2(1+2b+y) + c_1 v_1 x^{1-\lambda} y^\lambda \\ ac_2^2 \psi^{\Delta_{\text{b}}} &= bac_2 + bac_2^3 + ac_2 v_2 - ac_2^2(1+2b+y) + ac_2^2 v_2 x^{1-\lambda} y^\lambda \\ av_2 c_2 \psi^{\Delta_{\text{b}}} &= ac_2^2 - ac_2 v_2(1+x) + ac_2 x^\lambda y^{1-\lambda} \\ ac_2 \psi^{\Delta_{\text{b}}} &= bac_2^2 + c_1 h - ac_2(b+h+y) + ac_2 v_2 x^{1-\lambda} y^\lambda \end{cases} \quad (\text{F.3})$$

It is possible to algebraically solve for $\psi_\omega^{\Delta b}$, v_1 and v_2 in terms of c_1 and c_2 alone.

$$\begin{aligned}\psi_\omega^{\Delta b} &= \frac{1}{2} (v_2 x^{1-\lambda} y^\lambda + v_1 - y - 1 + b(c_1 + c_2 - 2) - 2h) \\ &\quad + \frac{1}{2} \sqrt{(v_2 x^{1-\lambda} y^\lambda - v_1 - y + 1 - b(c_1 - c_2))^2 + 4h^2}\end{aligned}\quad (\text{F.4})$$

$$\begin{aligned}v_1 &= \frac{1}{2} c_1 (y - x + 2b - c_1) - b \\ &\quad + \frac{1}{2} \sqrt{4c_1 (1 + c_1 x^\lambda y^{1-\lambda}) (1 + c_1 x^{1-\lambda} y^\lambda) + (c_1 (y - x + 2b - c_1) - b)^2}\end{aligned}\quad (\text{F.5})$$

$$\begin{aligned}v_2 &= \frac{1}{2} c_2 (y - x + 2b - c_2) - b \\ &\quad + \frac{1}{2} \sqrt{4c_2 (1 + c_2 x^\lambda y^{1-\lambda}) (1 + c_2 x^{1-\lambda} y^\lambda) + (c_2 (y - x + 2b - c_2) - b)^2}\end{aligned}\quad (\text{F.6})$$

By also eliminating a , this leaves a system of two coupled nonlinear equations for c_1 and c_2 ,

$$\begin{cases} \psi_\omega^{\Delta b} v_1 c_1 = c_1 - c_1 v_1 (x + 1) + v_1^2 x^\lambda y^{1-\lambda} \\ \psi_\omega^{\Delta b} v_2 c_2 = c_2^2 - c_2 v_2 (x + 1) + c_2 x^\lambda y^{1-\lambda}, \end{cases}\quad (\text{F.7})$$

This system can be solved numerically. The resulting values of c_1 and c_2 give the bound state scaled cumulant generating function, $\psi_\omega^{\Delta b}$, via Eq. (F.4). As plotted in Fig. 5.8, this localized branch crosses the translationally symmetric branch at λ^* , demonstrating that the cusp in ψ for the broken symmetry triangle network emerges for the same mathematical reasons as in the ring network. Namely, the singularity occurs at a transition between localized and delocalized eigenvectors.

In this presentation we have just accepted that the delocalized state will converge to the translationally symmetric solution in the large N limit. This can be confirmed with a delocalized state ansatz of the same form as Eq. (F.2) but with $c_1 = \exp(\gamma/N)$ such that c_1^N cannot be neglected. The result of that ansatz is another system of six equations with six unknowns, whose solution gives the translationally symmetric cumulant generating function.

Bibliography

- [1] Rosalind J. Allen, Chantal Valeriani, and Pieter Rein ten Wolde. “Forward flux sampling for rare event simulations”. *Journal of Physics: Condensed Matter* 21, 463102, 2009.
- [2] Rosalind J. Allen, Patrick B. Warren, and Pieter Rein Ten Wolde. “Sampling rare switching events in biochemical networks”. *Physical Review Letters* 94, 018104, 2005.
- [3] Rosalind J. Allen et al. “Homogeneous nucleation under shear in a two-dimensional Ising model: Cluster growth, coalescence, and breakup”. *The Journal of Chemical Physics* 129, 134704, 2008.
- [4] Bernhard Altaner, Artur Wachtel, and Jürgen Vollmer. “Fluctuating Currents in Stochastic Thermodynamics II. Energy Conversion and Nonequilibrium Response in Kinesin Models”. *arXiv preprint arXiv:1504.03648*, 2015.
- [5] Hans C. Andersen, David Chandler, and John D. Weeks. “Roles of repulsive and attractive forces in liquids: the equilibrium theory of classical fluids”. *Advances in Chemical Physics* 34, 105, 1976.
- [6] Hans C. Andersen, John D. Weeks, and David Chandler. “Relationship between the hard-sphere fluid and fluids with realistic repulsive forces”. *Physical Review A* 4, 1597, 1971.
- [7] Christophe Andrieu and Gareth O. Roberts. “The pseudo-marginal approach for efficient Monte Carlo computations”. *The Annals of Statistics*, 697–725, 2009.
- [8] Thomas E. Angelini et al. “Glass-like dynamics of collective cell migration”. *Proceedings of the National Academy of Sciences* 108, 4714–4719, 2011.
- [9] Manuel Athènes and Gilles Adjanor. “Measurement of nonequilibrium entropy from space-time thermodynamic integration”. *The Journal of Chemical Physics* 129, 024116, 2008.
- [10] Nathalie Q. Balaban et al. “Bacterial persistence as a phenotypic switch”. *Science* 305, 1622–1625, 2004.
- [11] Robin C. Ball, Thomas M.A. Fink, and Neill E. Bowler. “Stochastic annealing”. *Physical Review Letters* 91, 030201, 2003.

- [12] Mark A. Beaumont. “Estimation of population growth or decline in genetically monitored populations”. *Genetics* 164, 1139–1160, 2003.
- [13] L. Bertini et al. “Current fluctuations in stochastic lattice gases”. *Physical Review Letters* 94, 030601, 2005.
- [14] L. Bertini et al. “Non equilibrium current fluctuations in stochastic lattice gases”. *Journal of Statistical Physics* 123, 237–276, 2006.
- [15] Paul L. Biancaniello, Anthony J. Kim, and John C. Crocker. “Colloidal interactions and self-assembly using DNA hybridization”. *Physical Review Letters* 94, 058302, 2005.
- [16] Joseph W. Bigger. “Treatment of staphylococcal infections with penicillin by intermittent sterilisation”. *The Lancet* 244, 497–500, 1944.
- [17] T. Bodineau and B. Derrida. “Current fluctuations in nonequilibrium diffusive systems: an additivity principle”. *Physical Review Letters* 92, 180601, 2004.
- [18] T. Bodineau and B. Derrida. “Distribution of current in nonequilibrium diffusive systems and phase transitions”. *Physical Review E* 72, 066110, 2005.
- [19] Thierry Bodineau and Cristina Toninelli. “Activity phase transition for constrained dynamics”. *Communications in Mathematical Physics* 311, 357–396, 2012.
- [20] Peter G. Bolhuis, Christoph Dellago, and David Chandler. “Reaction coordinates of biomolecular isomerization”. *Proceedings of the National Academy of Sciences* 97, 5877–5882, 2000.
- [21] Peter G. Bolhuis et al. “Transition path sampling: Throwing ropes over rough mountain passes, in the dark”. *Annual Review of Physical Chemistry* 53, 291–318, 2002.
- [22] Ludovic Brun et al. “A theory of microtubule catastrophes and their regulation”. *Proceedings of the National Academy of Sciences* 106, 21173–21178, 2009.
- [23] Adrián A. Budini, Robert M. Turner, and Juan P. Garrahan. “Fluctuating observation time ensembles in the thermodynamics of trajectories”. *Journal of Statistical Mechanics: Theory and Experiment* 2014, P03012, 2014.
- [24] D.M. Ceperley and M. Dewing. “The penalty method for random walks with uncertain energies”. *The Journal of Chemical Physics* 110, 9812–9820, 1999.
- [25] David Chandler. “Barrier crossings: classical theory of rare but important events”. *Classical and Quantum Dynamics in Condensed Phase Simulations*, 5–23, 1998.
- [26] David Chandler. *Introduction to Modern Statistical Mechanics*. Vol. 1. Oxford University Press, 1987.
- [27] Raphaël Chetrite and Hugo Touchette. “Nonequilibrium Markov processes conditioned on large deviations”. In: *Annales Henri Poincaré*. Springer. 2014. 1–53.
- [28] Raphaël Chetrite and Hugo Touchette. “Nonequilibrium microcanonical and canonical ensembles and their equivalence”. *Physical Review Letters* 111, 120601, 2013.

- [29] D. Collin et al. “Verification of the Crooks fluctuation theorem and recovery of RNA folding free energies”. *Nature* 437, 231–234, 2005.
- [30] Gavin E. Crooks and David Chandler. “Efficient transition path sampling for nonequilibrium stochastic dynamics”. *Physical Review E* 64, 026109, 2001.
- [31] Gavin Earl Crooks. “Excursions in Statistical Dynamics”. PhD thesis. University of California, 1999.
- [32] Christoph Dellago, Peter G. Bolhuis, and David Chandler. “Efficient transition path sampling: Application to Lennard-Jones cluster rearrangements”. *The Journal of Chemical Physics* 108, 9236–9245, 1998.
- [33] Christoph Dellago et al. “Transition path sampling and the calculation of rate constants”. *The Journal of Chemical Physics* 108, 1964–1977, 1998.
- [34] Martin Depken, Juan M.R. Parrondo, and Stephan W. Grill. “Intermittent Transcription Dynamics for the Rapid Production of Long Transcripts of High Fidelity”. *Cell Reports* 5, 521–530, 2013.
- [35] Bernard Derrida. “Non-equilibrium steady states: fluctuations and large deviations of the density and of the current”. *Journal of Statistical Mechanics: Theory and Experiment* 2007, P07023, 2007.
- [36] Bernard Derrida and Joel L. Lebowitz. “Exact large deviation function in the asymmetric exclusion process”. *Physical Review Letters* 80, 209, 1998.
- [37] Lorenzo Di Michele et al. “Multistep kinetic self-assembly of DNA-coated colloids”. *Nature Communications* 4, 2013.
- [38] Ariane Dimitrov et al. “Detection of GTP-tubulin conformation in vivo reveals a role for GTP remnants in microtubule rescues”. *Science* 322, 1353–1356, 2008.
- [39] Marileen Dogterom and Stanislas Leibler. “Physical aspects of the growth and regulation of microtubule structures”. *Physical Review Letters* 70, 1347, 1993.
- [40] J.L. Doob. “Markoff chains—denumerable case”. *Transactions of the American Mathematical Society*, 455–473, 1945.
- [41] Rémi Dreyfus et al. “Aggregation-disaggregation transition of DNA-coated colloids: Experiments and theory”. *Physical Review E* 81, 041404, 2010.
- [42] Titus S. van Erp and Peter G. Bolhuis. “Elaborating transition interface sampling methods”. *Journal of Computational Physics* 205, 157–181, 2005.
- [43] Carlos P. Espigares, Pedro L. Garrido, and Pablo I. Hurtado. “Dynamical phase transition for current statistics in a simple driven diffusive system”. *Physical Review E* 87, 032115, 2013.
- [44] Alessandra Faggionato and Davide Gabrielli. “A representation formula for large deviations rate functionals of invariant measures on the one dimensional torus”. *Annales de l’Institut Henri Poincaré, Probabilités et Statistiques* 48, 212–234, 2012.

- [45] Richard P. Feynman. *Statistical Mechanics*. Vol. 1. Westview Press, 1972.
- [46] Daan Frenkel and Berend Smit. *Understanding Molecular Simulation: From Algorithms to Applications*. Vol. 1. Academic press, 2001.
- [47] Ikuko Fujiwara et al. “Microscopic analysis of polymerization dynamics with individual actin filaments”. *Nature Cell Biology* 4, 666–673, 2002.
- [48] Ethan C. Garner, Christopher S. Campbell, and R. Dyche Mullins. “Dynamic instability in a DNA-segregating prokaryotic actin homolog”. *Science* 306, 1021–1025, 2004.
- [49] Juan P. Garrahan et al. “Dynamical first-order phase transition in kinetically constrained models of glasses”. *Physical Review Letters* 98, 195702, 2007.
- [50] Juan P. Garrahan et al. “First-order dynamical phase transition in models of glasses: an approach based on ensembles of histories”. *Journal of Physics A: Mathematical and Theoretical* 42, 075007, 2009.
- [51] Nienke Geerts and Erika Eiser. “DNA-functionalized colloids: Physical properties and applications”. *Soft Matter* 6, 4647–4660, 2010.
- [52] Phillip L. Geissler, Christoph Dellago, and David Chandler. “Chemical dynamics of the protonated water trimer analyzed by transition path sampling”. *Physical Chemistry Chemical Physics* 1, 1317–1322, 1999.
- [53] Phillip L. Geissler et al. “Autoionization in liquid water”. *Science* 291, 2121–2124, 2001.
- [54] Daniel T. Gillespie. “A general method for numerically simulating the stochastic time evolution of coupled chemical reactions”. *Journal of Computational Physics* 22, 403–434, 1976.
- [55] Daniel T. Gillespie. “Exact stochastic simulation of coupled chemical reactions”. *The Journal of Physical Chemistry* 81, 2340–2361, 1977.
- [56] Todd R. Gingrich, Suriyanarayanan Vaikuntanathan, and Phillip L. Geissler. “Heterogeneity-induced large deviations in activity and (in some cases) entropy production”. *Physical Review E* 90, 042123, 2014.
- [57] Alex Gomez-Marin, Tim Schmiedl, and Udo Seifert. “Optimal protocols for minimal work processes in underdamped stochastic thermodynamics”. *The Journal of Chemical Physics* 129, 024114, 2008.
- [58] J.R. Gomez-Solano et al. “Experimental verification of a modified fluctuation-dissipation relation for a micron-sized particle in a nonequilibrium steady state”. *Physical Review Letters* 103, 040601, 2009.
- [59] Michael Grünwald, Christoph Dellago, and Phillip L. Geissler. “Precision shooting: Sampling long transition pathways”. *The Journal of Chemical Physics* 129, 194101, 2008.

- [60] Nicholas Guttenberg, Aaron R. Dinner, and Jonathan Weare. “Steered transition path sampling”. *The Journal of Chemical Physics* 136, 234103, 2012.
- [61] R.J. Harris, A. Rákos, and G.M. Schütz. “Current fluctuations in the zero-range process with open boundaries”. *Journal of Statistical Mechanics: Theory and Experiment* 2005, P08003, 2005.
- [62] Alexander K. Hartmann. “High-precision work distributions for extreme nonequilibrium processes in large systems”. *Physical Review E* 89, 052103, 2014.
- [63] W.K. Hastings. “Monte Carlo sampling methods using Markov chains and their applications”. *Biometrika* 57, 97–109, 1970.
- [64] Lester O. Hedges et al. “Dynamic order-disorder in atomistic models of structural glass formers”. *Science* 323, 1309–1313, 2009.
- [65] Haye Hinrichsen and Eytan Domany. “Damage spreading in the Ising model”. *Physical Review E* 56, 94, 1997.
- [66] Jie Hu, Ao Ma, and Aaron R. Dinner. “A two-step nucleotide-flipping mechanism enables kinetic discrimination of DNA lesions by AGT”. *Proceedings of the National Academy of Sciences* 105, 4615–4620, 2008.
- [67] Barry Isralewitz, Mu Gao, and Klaus Schulten. “Steered molecular dynamics and mechanical functions of proteins”. *Current Opinion in Structural Biology* 11, 224–230, 2001.
- [68] Robert L. Jack and Peter Sollich. “Large Deviations and Ensembles of Trajectories in Stochastic Models”. *Progress of Theoretical Physics*, 304–317, 2010.
- [69] C. Jarzynski. “Nonequilibrium equality for free energy differences”. *Physical Review Letters* 78, 2690, 1997.
- [70] N.G. van Kampen. *Stochastic Processes in Physics and Chemistry*. Vol. 1. Elsevier, 1992.
- [71] Iris Keren et al. “Specialized persister cells and the mechanism of multidrug tolerance in Escherichia coli”. *Journal of Bacteriology* 186, 8172–8180, 2004.
- [72] Aaron S. Keys et al. “Excitations are localized and relaxation is hierarchical in glass-forming liquids”. *Physical Review X* 1, 021013, 2011.
- [73] D. Lacoste, A.W.C. Lau, and K. Mallick. “Fluctuation theorem and large deviation function for a solvable model of a molecular motor”. *Physical Review E* 78, 011915, 2008.
- [74] Joel L. Lebowitz and Herbert Spohn. “A Gallavotti–Cohen-type symmetry in the large deviation functional for stochastic dynamics”. *Journal of Statistical Physics* 95, 333–365, 1999.
- [75] V. Lecomte, C. Appert-Rolland, and F. van Wijland. “Thermodynamic formalism for systems with Markov dynamics”. *Journal of Statistical Physics* 127, 51–106, 2007. ISSN: 0022-4715.

- [76] Mirjam E. Leunissen et al. “Towards self-replicating materials of DNA-functionalized colloids”. *Soft Matter* 5, 2422–2430, 2009.
- [77] Kim Lewis. “Persister cells”. *Annual Review of Microbiology* 64, 357–372, 2010.
- [78] Kim Lewis. “Programmed death in bacteria”. *Microbiology and Molecular Biology Reviews* 64, 503–514, 2000.
- [79] John Liebler et al. *The Inner Life of the Cell*. 2007. URL: http://multimedia.mcb.harvard.edu/anim_innerlife_hi.html (visited on 04/20/2015).
- [80] L. Lin, K.F. Liu, and J. Sloan. “A noisy Monte Carlo algorithm”. *Physical Review D* 61, 074505, 2000.
- [81] Jan Liphardt et al. “Equilibrium information from nonequilibrium measurements in an experimental test of Jarzynski’s equality”. *Science* 296, 1832–1835, 2002.
- [82] Hanbin Mao et al. “Temperature control methods in a laser tweezers system”. *Bioophysical Journal* 89, 1308–1316, 2005.
- [83] A.M. Mariz, H.J. Herrmann, and L. de Arcangelis. “Comparative study of damage spreading in the Ising model using heat-bath, Glauber, and Metropolis dynamics”. *Journal of Statistical Physics* 59, 1043–1050, 1990.
- [84] Francisco J. Martinez-Veracoechea et al. “Designing stimulus-sensitive colloidal walkers”. *Soft Matter* 10, 3463–3470, 2014.
- [85] Mathew M. Maye et al. “Stepwise surface encoding for high-throughput assembly of nanoclusters”. *Nature Materials* 8, 388–391, 2009.
- [86] Jakob Mehl, Thomas Speck, and Udo Seifert. “Large deviation function for entropy production in driven one-dimensional systems”. *Physical Review E* 78, 011123, 2008.
- [87] Nicholas Metropolis et al. “Equation of state calculations by fast computing machines”. *The Journal of Chemical Physics* 21, 1087–1092, 1953.
- [88] Tim Mitchison and Marc Kirschner. “Dynamic instability of microtubule growth”. *Nature* 312, 237–242, 1984.
- [89] Bortolo M. Mognetti et al. “Predicting DNA-mediated colloidal pair interactions”. *Proceedings of the National Academy of Sciences* 109, E378, 2012.
- [90] Daniele Moroni, Titus S. van Erp, and Peter G. Bolhuis. “Investigating rare events by transition interface sampling”. *Physica A: Statistical Mechanics and its Applications* 340, 395–401, 2004.
- [91] Jerome P. Nilmeier et al. “Nonequilibrium candidate Monte Carlo is an efficient tool for equilibrium simulation”. *Proceedings of the National Academy of Sciences* 108, E1009–E1018, 2011.
- [92] David J. Norris and Yurii A. Vlasov. “Chemical approaches to three-dimensional semiconductor photonic crystals”. *Advanced Materials* 13, 371–376, 2001.

- [93] Dmytro Nykypanchuk et al. “DNA-guided crystallization of colloidal nanoparticles”. *Nature* 451, 549–552, 2008.
- [94] Harald Oberhofer, Christoph Dellago, and Phillip L. Geissler. “Biased sampling of nonequilibrium trajectories: Can fast switching simulations outperform conventional free energy calculation methods?” *The Journal of Physical Chemistry B* 109, 6902–6915, 2005.
- [95] Sanghyun Park. “Comparison of the serial and parallel algorithms of generalized ensemble simulations: An analytical approach”. *Physical Review E* 77, 016709, 2008.
- [96] Sanghyun Park et al. “Free energy calculation from steered molecular dynamics simulations using Jarzynski’s equality”. *The Journal of Chemical Physics* 119, 3559–3566, 2003.
- [97] David Popp et al. “Suprastructures and dynamic properties of Mycobacterium tuberculosis FtsZ”. *Journal of Biological Chemistry* 285, 11281–11289, 2010.
- [98] Lawrence R. Pratt and David Chandler. “Theory of the hydrophobic effect”. *The Journal of Chemical Physics* 67, 3683–3704, 1977.
- [99] Peter Reimann. “Brownian motors: noisy transport far from equilibrium”. *Physics Reports* 361, 57–265, 2002.
- [100] Tim Schmiedl and Udo Seifert. “Optimal finite-time processes in stochastic thermodynamics”. *Physical Review Letters* 98, 108301, 2007.
- [101] J. Schnakenberg. “Network theory of microscopic and macroscopic behavior of master equation systems”. *Reviews of Modern Physics* 48, 571, 1976.
- [102] Udo Seifert. “Entropy production along a stochastic trajectory and an integral fluctuation theorem”. *Physical Review Letters* 95, 040602, 2005.
- [103] Udo Seifert. “Stochastic thermodynamics, fluctuation theorems and molecular machines”. *Reports on Progress in Physics* 75, 126001, 2012.
- [104] Jong-Shik Shin and Niles A. Pierce. “A synthetic DNA walker for molecular transport”. *Journal of the American Chemical Society* 126, 10834–10835, 2004.
- [105] Michael R. Shirts and John D. Chodera. “Statistically optimal analysis of samples from multiple equilibrium states”. *The Journal of Chemical Physics* 129, 124105, 2008.
- [106] Matthew J. Siegfried and Kyoung-Shin Choi. “Directing the architecture of cuprous oxide crystals during electrochemical growth”. *Angewandte Chemie* 117, 3282–3287, 2005.
- [107] David A. Sivak, John D. Chodera, and Gavin E. Crooks. “Time step rescaling recovers continuous-time dynamical properties for discrete-time Langevin integration of nonequilibrium systems”. *The Journal of Physical Chemistry B* 118, 6466–6474, 2014.

- [108] David A. Sivak, John D. Chodera, and Gavin E. Crooks. “Using nonequilibrium fluctuation theorems to understand and correct errors in equilibrium and nonequilibrium simulations of discrete Langevin dynamics”. *Physical Review X* 3, 011007, 2013.
- [109] Frank H. Stillinger and Aneesur Rahman. “Improved simulation of liquid water by molecular dynamics”. *The Journal of Chemical Physics* 60, 1545–1557, 1974.
- [110] Gabriel Stoltz. “Path sampling with stochastic dynamics: Some new algorithms”. *Journal of Computational Physics* 225, 491–508, 2007.
- [111] Holger Then and Andreas Engel. “Computing the optimal protocol for finite-time processes in stochastic thermodynamics”. *Physical Review E* 77, 041105, 2008.
- [112] Hugo Touchette. “The large deviation approach to statistical mechanics”. *Physics Reports* 478, 1–69, 2009.
- [113] Hugo Touchette and Rosemary J. Harris. “Large Deviation Approach to Nonequilibrium Systems”. *Nonequilibrium Statistical Physics of Small Systems: Fluctuation Relations and Beyond*, 335–360, 2013.
- [114] F. Turci and E. Pitard. “Large deviations and heterogeneities in a driven kinetically constrained model”. *Europhysics Letters* 94, 10003, 2011.
- [115] Suriyanarayanan Vaikuntanathan, Todd R. Gingrich, and Phillip L. Geissler. “Dynamic phase transitions in simple driven kinetic networks”. *Physical Review E* 89, 062108, 2014.
- [116] Patrick Varilly et al. “A general theory of DNA-mediated and other valence-limited colloidal interactions”. *The Journal of Chemical Physics* 137, 094108, 2012.
- [117] Nora Vázquez-Laslop, Hyunwoo Lee, and Alexander A. Neyfakh. “Increased persistence in *Escherichia coli* caused by controlled expression of toxins or other unrelated proteins”. *Journal of Bacteriology* 188, 3494–3497, 2006.
- [118] Teun Vissers et al. “Lane formation in driven mixtures of oppositely charged colloids”. *Soft Matter* 7, 2352–2356, 2011.
- [119] Artur Wachtel, Jürgen Vollmer, and Bernhard Altaner. “Determining the Statistics of Fluctuating Currents: General Markovian Dynamics and its Application to Motor Proteins”. *arXiv preprint arXiv:1407.2065*, 2014.
- [120] Artur Wachtel, Jürgen Volmer, and Bernhard Altaner. “Fluctuating Currents in Stochastic Thermodynamics I. Gauge Invariance of Asymptotic Statistics”. *arXiv preprint arXiv:1407.2065*, 2015.
- [121] Jeffrey K. Weber et al. “Dynamical Phase Transitions Reveal Amyloid-like States on Protein Folding Landscapes”. *Biophysical Journal* 107, 974–982, 2014.
- [122] John D. Weeks, David Chandler, and Hans C. Andersen. “Role of repulsive forces in determining the equilibrium structure of simple liquids”. *The Journal of Chemical Physics* 54, 5237–5247, 1971.

- [123] Peng Yin et al. “Programming biomolecular self-assembly pathways”. *Nature* 451, 318–322, 2008.
- [124] Patrick R Zulkowski et al. “Geometry of thermodynamic control”. *Physical Review E* 86, 041148, 2012.